TECHNISCHE UNIVERSITÄT WIEN

Diploma Thesis

Conductivity relaxation of mixed ionic and electronic conducting oxides

carried out for the purpose of obtaining the degree of Master of Science (MSc or Dipl.-Ing. or DI), submitted at TU Wien, Faculty of Mechanical and Industrial Engineering, by

Christin Böhme
Mat.Nr.: 01141221

under the supervision of

Univ.Prof. Dipl.-Phys. Dr.rer.nat. Jürgen Fleig
and
Univ.Ass. Dipl.-Ing. Dr.rer.nat. Markus Kubicek
Institute of Chemical Technologies and Analytics, E164

Affidavit

I declare in lieu of oath, that I wrote this thesis and performed the associated research myself, using only literature cited in this volume.

Christin Böhme

Vienna, July 2020

Abstract

Oxygen exchange at the surface of a mixed ionic and electronic conducting (MIEC) perovskite type oxide and subsequent diffusion of oxygen within the bulk of the material are technologically relevant transport processes as they ensure the functionality of various devices such as solid oxide fuel cells (SOFCs) and high temperature oxygen sensors. Thus, understanding how these transport processes are affected by operating conditions, such as temperature and oxygen partial pressure, as well as by specific material properties of the MIEC oxide, e.g. structure, doping and strain, is of great interest.

In this work, the oxygen transport properties of various MIEC oxides were investigated by application of the van der Pauw method to conductivity relaxation experiments. Selected materials included e.g. nominally undoped $SrTiO_3$ (STO) and Fe-doped STO single crystals as well as $La_{0.6}Sr_{0.4}CoO_{3-\delta}$ (LSC) thin films. The LSC thin films were deposited by pulsed laser deposition (PLD) on various substrates such as single-cyrstalline MgO, $LaAlO_3$ (LAO) and STO. Measurements were carried out in the pO_2 range between 0.015 bar and 0.2 bar. A fitting procedure was developed, which allowed for determination of the surface exchange coefficient, k_{chem}, and the chemical diffusion coefficient, D_{chem}, from the measured relaxation data. Evaluated kinetic parameters were either discussed in connection with dopant concentration (Fe:STO, STO) or with regard to the difference in the utilized substrates (LSC thin films). The acceptor doping in the deliberately doped Fe:STO single crystal, for instance, likely increased the influence of the trapping effect, resulting in undoped STO exhibiting faster surface kinetics and thus higher k_{chem} values.

In addition to the kinetic parameters, the equilibrium conductivity could also be evaluated as a function of the surrounding pO_2 from the measured relaxation data. In accordance with literature data, higher conductivity values were measured for the Fe:STO single crystal resulting from the higher iron concentration. In contrast to the epitaxial films grown on LAO and STO, which exhibited comparable conductivity values to bulk LSC, lower conductivity values were measured in case of the LSC|MgO thin film, which can be attributed to the grain boundaries in the columnar structure of the film.

Furthermore, in the course of the conducted conductivity relaxation experiments on the LSC thin films, a secondary, slower relaxation process was discovered, which partly superposed entire measurements. Experimental conditions, under which this drift-phenomenon was observed, were characterized.

Kurzfassung

Sauerstoffaustausch an der Oberfläche eines gemischtleitenden Oxids sowie die nachfolgende Diffusion von Sauerstoff innerhalb der Volumensphase des Materials sind technologisch wichtige Prozesse, da sie die Funktionsweise von verschiedenen Anwendungen, wie z.B. jene von Festoxid-Brennstoffzellen sowie jene von Hochtemperatur-Sauerstoffsensoren, sicherstellen. Daher ist es von großem Interesse zu verstehen, wie diese Transportprozesse von Betriebsbedingungen, wie Temperatur und Sauerstoffpartialdruck, und von spezifischen Materialeigenschaften des gemischtleitenden Oxids, z.B. Struktur, Dotierung und Verzerrungen im Kristallgitter, beeinflusst werden.

In dieser Arbeit wurden die Sauerstofftransporteigenschaften von verschiedenen gemischtleitenden Oxiden unter Anwendung der van der Pauw Methode auf Leitfähigkeitsrelaxationsexperimente untersucht. Zu den ausgewählten Materialien zählten unter anderem nominell undotierte $SrTiO_3$ (STO) und Fe-dotierte Einkristalle sowie $La_{0.6}Sr_{0.4}CoO_{3-\delta}$ (LSC) Dünnfilme. Die LSC Dünnfilme wurden mittels Laserdeposition (pulsed laser deposition, PLD) auf verschieden Substraten, wie einkristallinem MgO, $LaAlO_3$ (LAO) und STO, abgeschieden. Ein Anpassungsverfahren wurde entwickelt, welches es ermöglichte den Oberflächenaustauschkoeffizienten, k_{chem}, und den chemischen Diffusionskoeffizienten, D_{chem}, aus den gemessenen Relaxationsdaten zu bestimmen. Die ausgewerteten kinetischen Parameter wurden entweder im Zusammenhang mit der Dotierungskonzentration (Fe:STO, STO) oder im Hinblick auf den Unterschied in den verwendeten Substraten (LSC Dünnfilme) diskutiert. Beispielsweise erhöhte die Akzeptordotierung im gezielt dotierten Fe:STO Einkristall wahrscheinlich den Einfluss des Trappings, was dazu führte, dass undotiertes STO eine schnellere Kinetik im Hinblick auf den Oberflächeneinbau und somit höhere k_{chem} Werte aufwies.

Neben den kinetischen Parametern konnte zudem die Gleichgewichtsleitfähigkeit in Abhängigkeit des umgebenden pO_2 aus den Relaxationsdaten ausgewertet werden. In Übereinstimmung mit Literaturdaten wurden im Fall des Fe:STO Einkristalls höhere Leitfähigkeiten gemessen, was auf den höheren Eisengehalt zurückzuführen ist. Im Gegensatz zu den epi-

taktischen Filmen auf LAO und STO, welche vergleichbare Leitfähigkeitswerte zu bulk LSC aufwiesen, wurden für den LSC|MgO Dünnfilm niedrigere Leitfähigkeitswerte gemessen, was auf Korngrenzen in der kolumnaren Struktur des Films zurückgeführt werden kann.

Darüber hinaus wurde im Zuge der Relaxationsexperimente an den LSC Dünnfilmen ein zusätzlicher, langsamerer Relaxationsprozess entdeckt, welcher Messungen zum Teil vollständig überlagerte. Experimentelle Bedingungen, unter denen dieses Drift-Phänomen beobachtet wurde, wurden charakterisiert.

Contents

Symbols

Symbol	Description	Unit
a	half of the sample thickness	cm
A	area	cm^2
c	molar concentration	mol/cm^3
d	sample thickness	cm
D_{chem}	chemical diffusion coefficent	cm^2/s
F	Faraday's constant	C/mol
f	correction factor	-
I	current	A
j	molar flux density	mol/cm^2s
k_{chem}	surface exchange coefficient	cm/s
k_r	effective rate constant	1/s
L	dimensionless parameter	-
L_c	characteristic length	cm
N_A	Avogadro constant	1/mol
t	time	s
T_r	reactor temperature	K
T_{STP}	room temperature	K
U	voltage	V
V	volume	cm^3
V_r	reactor volume	cm^3
z	charge number	-
$\Phi_{r,tot}$	gas flow rate	cm^3/s
α_n	eigenvalues	-
δ	oxygen nonstoichiometry	-
δc	concentration deviation from equilibrium state	mol/cm^3
$\delta\mu$	chemical potential deviation from equilibrium state	J/mol
μ	chemical potential	J/mol

Symbol	Description	Unit
$\tilde{\mu}$	electrochemical potential	J/mol
ρ	resistivity	Ω cm
σ	electrical conductivity	S/cm
σ_g	grain conductivity	S/cm
σ_{gb}	grain boundary conductivity	S/cm
σ_{norm}	normalized conductivity	-
τ_f	reactor flush time	s
ϕ	electric potential	V

1. Introduction

Oxygen transport in mixed ionic and electronic conducting (MIEC) perovskite type oxides is a key process that ensures the functionality of various technologically relevant devices. Perovskite type oxides are, for example, applicable as cathode materials in intermediate temperature solid oxide fuel cells (IT-SOFCs) and thus, responsible for oxygen reduction and further transport of oxygen ions to the cathode|electrolyte interface [1]. Furthermore, used as oxygen separation membranes perovskite materials selectively transport oxygen from the feed to the permeate side [2]. In addition, perovskite type oxides are also applied in resistive high temperature oxygen sensors [3–5]. In this instance, the material's ability to incorporate and release oxygen into and from its crystal structure, thereby simultaneously altering its charge carrier concentration, is utilized in the sensing process. The desired operating performance of each mentioned device, that is, high output currents in case of IT-SOFCs, high oxygen fluxes for oxygen separation membranes and fast signal responses in case of oxygen sensors, relies on fast oxygen transport. Therefore, understanding how the oxygen transport properties of a respective MIEC perovskite type oxide are affected by the nature of the material as well as by experimental and operating conditions, respectively, is crucial.

With regard to experimental conditions, quantifying the influence of oxygen partial pressure (pO_2) and temperature on the oxygen transport properties is of primary interest. The oxygen transport in the above mentioned devices essentially consists of oxygen exchange at the gas|solid interface and subsequent diffusion of oxygen within the bulk of the material. Hence, assessing the influence of said process variables by evaluating the corresponding kinetic parameters as specific material properties constitutes an appropriate possibility. Specifically, the two transport processes are represented by the surface exchange coefficient, k, and the diffusion coefficient, D. Over the past years many studies thus aimed at characterizing the pO_2 and temperature dependence of k and D for various perovskite materials including $La_{1-x}Sr_xCoO_{3-\delta}$ [6, 7], $La_{1-x}Sr_xFeO_{3-\delta}$ [8], $Ba_{1-x}Sr_xCo_{1-y}Fe_yO_{3-\delta}$ [9, 10], $La_{1-x}Sr_xCo_{1-y}Fe_yO_{3-\delta}$ [11] and $SrTi_{1-x}Fe_xO_{3-\delta}$ [12, 13], which are either potential or already established materials for the applications mentioned at the beginning. In all quoted studies defined gas atmospheres were used

to investigate the short-term behavior of the respective oxygen exchange kinetics. With respect to real operating conditions, however, testing the oxygen transport properties on longer time scales at elevated temperatures and in presence of gas phase contaminates is necessary. For instance, prolonged exposure to elevated temperatures might cause changes in the material's surface composition. For $La_{0.6}Sr_{0.4}CoO_{3-\delta}$ (LSC) Sr enrichment in the surface near zone has been repeatedly reported after thermal annealing, which in addition has been linked to degradation of the material's surface exchange kinetics [14–17]. Studies, which further investigated the long-term behavior of the oxygen transport properties of LSC in presence of gas phase contaminates, such as SO_2, Si and Cr, showed that the kinetic parameters decrease and thus, the oxygen exchange kinetics deteriorate due to the presence of said contaminates [18–20]. In addition to impurities in the gas phase, however, humid atmospheres might also cause a degradation of the material's oxygen exchange kinetics [16].

The oxygen transport properties are, as already mentioned above, also affected by the material itself. In principle, the oxygen diffusion mechanism, for example, depends on the crystal structure of the material and thus on the existing point defects. While the perovskite type oxides with general formula $ABO_{3-\delta}$ discussed in this work transport oxygen via oxygen vacancies, oxygen migration through layered hyperstoichiometric $A_2BO_{4+\delta}$ oxides with a $KNiF_4$-type structure is enabled by an interstitialcy mechanism [1]. Additionally, for compositions of $La_{1-x}Sr_xCoO_{3-\delta}$, $Ba_{1-x}Sr_xCo_{1-y}Fe_yO_{3-\delta}$ and $La_{1-x}Sr_xCo_{1-y}Fe_yO_{3-\delta}$ the oxygen vacancy concentration and their mobility ($\widehat{=}$ ionic conductivity) are key factors that determine the rate of the surface exchange, whereas the electronic conductivity is of secondary importance [21]. (A reasonably high electronic conductivity is still required to ensure the supply of electronic charge carriers consumed in the oxygen transport.) Besides affecting the surface exchange, the ionic conductivity is also coupled indirectly with the diffusion kinetics of the material [6, 22]. Since the perovskite structure is extremely flexible with regard to doping and substitution of different elements or cations on its A- or B-site, the magnitude of the ionic and electronic conductivity can be adjusted by the respective composition of the perovskite oxide. That is, substituting A and/or B site cations by aliovalent cations leads to changes in the electronic structure as well as in the oxygen non-stoichiometry of the perovskite material, thereby altering the material's electronic and ionic conductivity. Thus, in that sense the composition constitutes an additional factor controlling the oxygen transport properties of perovskite type oxides. In context of oxygen vacancy concentrations and mobility and their relevance in the oxygen transport process for a number of perovskite oxides, the effect of lattice strain on the oxygen exchange kinetics is also worth mentioning. Lattice strain induced by lattice mismatch at the interface between a thin film and a substrate changes e.g. the oxygen defect formation

enthalpy and their migration barrier in the film [23]. Tensile strain in $La_{0.8}Sr_{0.2}CoO_{3-\delta}$ thin films, for example, was found to induce higher oxygen vacancy concentrations at the film's surface compared to its compressive counterpart [15]. Furthermore, in a subsequent study, which quantified the effect of lattice strain on the oxygen transport properties, Kubicek et al. showed that tensile strained $La_{1-x}Sr_xCoO_{3-\delta}$ thin films on single-crystalline $SrTiO_3$ (STO) exhibited faster surface exchange and diffusion kinetics [24] compared to compressively strained films on single-crystalline $LaAlO_3$ (LAO). The authors deduced that tensile strain lowers the formation enthalpy of oxygen vacancies and/or their migration barrier, thereby enhancing the oxygen exchange kinetics of the respective thin films [24]. Additionally, metallic surface decorations in form of coatings or nanoparticles may affect the surface exchange reaction. For example, platinum and silver coatings were found to accelerate the surface exchange of iron doped STO single crystals [12]. The same effect was also observed for $La_{0.6}Sr_{0.4}FeO_{3-\delta}$ thin films decorated with platinum nanoparticles [25, 26]. In both instances the metallic decorations enhance oxygen dissociation and thus, accelerate one step in the multi-step reaction chain of the surface exchange. Oxygen transport may be further affected by material or process specific factors, which are not discussed in more detail at this point, e.g. the microstructure of the material (porosity, grain size, grain boundaries etc.) [1, 22], orientation [27], UV irradiation [28] and deposition conditions in case of thin films [29].

Generally, the kinetics of the oxygen transport are accessible by three experimental approaches: the tracer experiment, the electrical experiment and the chemical experiment [30]. Techniques, which rely on these experimental methods, include isotope exchange depth profiling [24, 31, 32], impedance spectroscopy [32], thermogravimetry [33] and electrical conductivity relaxation [6–8, 34–36]. Essentially, the corresponding kinetic parameters, that is, the surface exchange coefficient and the diffusion coefficient, are obtained by fitting the measured data to an appropriate theoretical model. The obtained k and D values of said experimental approaches, however, conceptually differ from each other, since each method utilizes a different driving force to quantify the oxygen exchange kinetics [30]. Thus, a direct comparison of kinetic parameters obtained by different methods is generally not possible [30].

In this work, electrical conductivity relaxation was used to investigate the oxygen exchange kinetics of $La_{0.6}Sr_{0.4}CoO_{3-\delta}$ polycrystals and LSC thin films as well as of undoped and iron doped STO single crystals. In conductivity relaxation experiments an outer gradient in the oxygen chemical potential ($\widehat{=}$ step change in the pO_2 in the surrounding atmosphere) is imposed on the sample, which causes the sample either to incorporate oxygen into or release oxygen from its crystal structure. As a result, the oxygen content and thus the charge carrier concentration of the material relaxes to a new equilibrium value, which allows for measuring the change

in electrical conductivity over time to evaluate the oxygen transport kinetics. Measurements were carried out in the pO_2 range between 0.015 bar and 0.2 bar at various temperatures. The re-equilibration kinetics of each sample were followed by measuring the dc-conductivity via the van der Pauw method. The main objective was to determine the kinetic parameters, k_{chem} and D_{chem}, from the recorded data and to quantify the influence of pO_2, temperature, dopant concentration and different strain states induced by different substrates on said oxygen transport properties. In addition to the kinetic parameters, the materials' equilibrium conductivity, which was attained after a respective pO_2 step had been applied, was obtainable from the measured data. Thus, studying the electrical properties of LSC and (Fe:)STO in connection to the aforementioned factors was also possible.

2. Theoretical background

2.1. Crystal structure and defect chemistry of (Fe:)STO and LSC

In this work, nominally undoped $SrTiO_3$ (STO), iron doped $SrTiO_3$ (Fe:STO) as well as $La_{0.6}Sr_{0.4}CoO_{3-\delta}$ (LSC) were investigated by means of conductivity relaxation. Each of said materials conducts ions as well as electronic charge carriers ($\widehat{=}$ electrons, electron holes). They are mixed ionic and electronic conductors. Furthermore, the materials adopt the perovskite type structure $ABO_{3-\delta}$ [22, 37].

Figure 2.1 depicts the A-centered view of an ideal cubic perovskite structure $ABO_{3-\delta}$. The structure can be conceived to consist of a large cation, which occupies the A site and is coordinated by 12 oxygen atoms, and corner-sharing BO_6 octahedra, where B is a smaller cation [38].

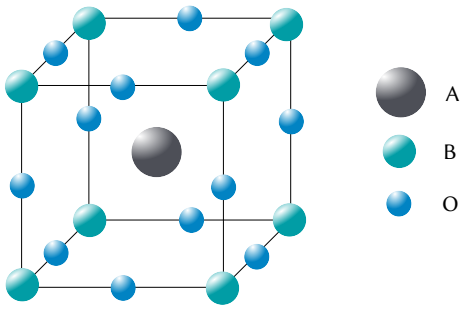

Figure 2.1.: A-centered view of a unit cell of an ideal cubic perovskite structure.

In the two following subsections the respective site occupation in the pervoskite type structure for (Fe:)STO and LSC will be briefly presented. Furthermore, the effects of introducing acceptor dopants (Fe^{3+}, Sr^{2+}) into the crystal lattice will be discussed in terms of defect chemistry for each compound.

2.1.1. Fe:STO

$SrTi_{1-x}Fe_xO_{3-\delta}$ is a solid solution series between $SrTiO_3$ and $SrFeO_{3-\delta}$, in which the iron content is variable between $0 \leq x \leq 1$ [22]. The solid solution series adapts a cubic pervoskite type structure for all compositions between $0 \leq x \leq 1$ [39]. Below a doping level of $x < 0.01$, $SrTi_{1-x}Fe_xO_{3-\delta}$ is considered to be a dilute solution of Fe in $SrTiO_3$ [40, 41]. The corresponding defect model for these compositions has been investigated thoroughly by many authors [42–47] and provides the basis for the following description as the doping level of the sample used in this work was 0.16 mol% Fe.

The A site in Fe:STO is occupied by Sr^{2+}, whereas Ti^{4+} and Fe^{3+} occupy the B-site. Using the Körger-Vink notation, the partial substitution of Ti^{4+} for Fe^{3+} is written as Fe'_{Ti} indicating that an effective negative charge with respect to the surrounding structure is introduced. The relative negative charge is only partly balanced by formation of electron holes ($h^\bullet$) [22]. Charge compensation occurs mostly by formation of oxygen vacancies ($V_O^{\bullet\bullet}$) [22]. Both point defect species are highly important as they are necessary for oxygen incorporation or release as well as for oxygen diffusion within the material. Furthermore, in Fe:STO iron does not only exist as Fe^{3+}, but also as Fe^{4+} ($\widehat{=} Fe^{\times}_{Ti}$) and can therefore undergo valence changes according to the following reaction [42, 46, 47]

$$Fe^{\times}_{Ti} \rightleftharpoons Fe'_{Ti} + h^\bullet. \tag{2.1}$$

Equation (2.1) represents an internal source and sink term for electronic charge carriers [42] and thus, the law of mass conservation must be satisfied [42],

$$[Fe] = [Fe^{\times}_{Ti}] + [Fe'_{Ti}]. \tag{2.2}$$

The concentration of $Fe^{\times}_{Ti}$ increases with decreasing temperature and increasing pO_2 in the surrounding atmosphere [22]. Obviously, $[Fe'_{Ti}]$ has to decrease simultaneously according to Equation (2.2).

Further, the generation and recombination of electrons and electron holes has to be taken into account [42, 46, 47]

$$nil \rightleftharpoons e' + h^\bullet. \tag{2.3}$$

At sufficiently high temperatures (T ≈ 750 K [42, 48]) Fe:STO establishes a equilibrium state with the surrounding atmosphere depending on the respective pO_2. If the oxygen partial pressure is changed in oxidizing direction, oxygen is incorporated into the lattice by annihilation and formation of a oxygen vacancy and two electron holes, respectively (see Equation (2.4)). Conversely, if the pO_2 is switched in reducing direction, oxygen is released from the crystal lattice creating a oxygen vacancy and two conduction electrons (see Equation (2.5)).

$$\frac{1}{2}O_2 + V_O^{\bullet\bullet} \rightleftharpoons O_O^{\times} + 2h^{\bullet} \tag{2.4}$$

$$O_O^{\times} \rightleftharpoons \frac{1}{2}O_2 + V_O^{\bullet\bullet} + 2e' \tag{2.5}$$

Since the electroneutrality of the material has to be maintained, the charge neutrality condition reads [42]

$$2[V_O^{\bullet\bullet}] + [h^{\bullet}] = [Fe'_{Ti}] + [e']. \tag{2.6}$$

It is noted that Equation (2.6) is a simplified form of the charge neutrality condition, that, in its fullest form, includes nine charged point defects (e.g. singly & doubly charged strontium vacancies, dopant-vacancy associates, hydroxide ions) [48]. Equation (2.6) holds in the temperature range between ≈ 750 K and ≈ 1300 K under dry experimental conditions [48].

This condensed description of the defect chemistry of Fe:STO is also applicable to nominally undoped STO. In undoped STO, titanium may be substituted by extrinsic acceptor impurities (e.g. Fe, Mn) [46, 48]. Furthermore, strontium vacancies, which are introduced during fabrication, are immobile below ≈ 1000 °C and effectively act as intrinsic acceptors in STO [46, 48]. Equation (2.7) - Equation (2.10) are the adapted equations, where A denotes an unspecified extrinsic acceptor impurity. Again, the charge neutrality condition (Equation (2.10)) has to be considered in reference to the aforementioned temperature range. Equation (2.3) - Equation (2.5) hold independently.

$$A_{Ti}^{\times} \rightleftharpoons A'_{Ti} + h^{\bullet} \tag{2.7}$$

$$[A] = [A_{Ti}^{\times}] + [A'_{Ti}] \tag{2.8}$$

$$2[V''_{Sr}] + [A_{Ti}^{\times}] = [A'_{total}] \tag{2.9}$$

$$2[V_O^{\bullet\bullet}] + [h^{\bullet}] = [A'_{total}] + [e'] \tag{2.10}$$

2.1.2. LSC

Depending on the Sr content as well as on the temperature, $La_{1-x}Sr_xCoO_{3-\delta}$ can either adapt a rhombohedral or a cubic perovskite type structure [49, 50]. The rhombohedral structure is favored at lower temperatures and a transformation to the cubic structure is possible if the temperature is increased [49]. Furthermore, the transition temperature ($\widehat{=}$ temperature at which the structural transformation occurs) decreases with increasing Sr content [49, 51]. Søgaard et al. estimated that $La_{0.6}Sr_{0.4}CoO_{3-\delta}$ adapts the cubic structure above 475 °C±25 °C [52]. For a Sr content of x=0.5 Petrov et al. found that the transition between the rhombohedral and the cubic structure occurs at 365 K [49]. A cubic structure at room temperature can be anticipated for $x > 0.55$ [49, 50].

In $La_{1-x}Sr_xCoO_{3-\delta}$ La^{3+} occupies the A-site and is partly substituted by Sr^{2+} ($\widehat{=} Sr'_{La}$), creating an effective negative charge with respect to the surrounding crystal lattice. The valences of lanthanum, strontium and oxygen are fixed, whereas Co, which occupies the B-site, can adapt different valence states between Co^{2+} and Co^{4+} [53]. Charge neutrality is maintained by an increase of the mean Co valence and an increase of the oxygen non-stoichiometry [53, 54]. According to Mizusaki et al., for a strontium content $x \leq 0.2$ the introduced relative negative charge is mainly compensated by an increase of the mean Co valence, whereas between $0.2 \leq x \leq 0.5$ charge neutrality is mainly restored by an increasing oxygen deficit of the material [53]. A further increase of the strontium content ($x > 0.5$) again results in an increase of the mean Co valence [53]. These results were obtained at 800 °C, however, Mizusaki et al. noted that similar trends were also observed at different temperatures [53].

Furthermore, the defect concentrations of $La_{1-x}Sr_xCoO_{3-\delta}$ depend on the oxygen partial pressure in the surrounding atmosphere. That is, LSC also establishes equilibrium states with the surrounding atmosphere at sufficiently high temperatures. The respective equilibria for the oxygen incorporation into as well as for the oxygen release from the crystal lattice were already given in subsection 2.1.1 for (Fe:)STO (see Equation (2.4), Equation (2.5)). As said equilibria are the same for LSC they are not stated again at this point. Consequently, the overall charge neutrality condition for $La_{1-x}Sr_xCoO_{3-\delta}$ can be expressed by

$$2[V_O^{\bullet\bullet}] + [h^{\bullet}] = [Sr'_{La}] + [e'] \tag{2.11}$$

Remarks about the electronic structure of $La_{1-x}Sr_xCoO_{3-\delta}$ have been left out of the description as the interpretation of the obtained equilibrium conductivity values from the conductivity relaxation experiments could be carried out on the basis of Equation (2.4), Equation (2.5) and Equation (2.11), respectively. It is noted, however, that two different models are discussed in literature. Firstly, a model that assumes that the defects are randomly distributed within the material (dilute solution) and that the electronic defects are localized on Co sites [49, 54]. Secondly, the itinerant electron model, which treats oxygen vacancies according to the dilute solution model, whereas the conduction electrons are assumed to be delocalized in a partially filled, rigid electron band [55–58]. The reader is referred to the quoted works for a detailed description of the two concepts.

2.2. Conductivity Relaxation

2.2.1. Principles

The conductivity relaxation method can be used to investigate the oxygen exchange kinetics of mixed ionic and electronic conducting materials. Generally, the change in conductivity of a respective material, that occurs after the oxygen chemical potential in the atmosphere has been changed, is recorded as a function of time [35].

At the beginning of an experiment the sample is in equilibrium with the surrounding atmosphere. Changing the oxygen partial pressure abruptly causes the sample, depending on the direction, in which the pO_2 is switched, to either release or incorporate oxygen until it attains a new equilibrium state with the surrounding atmosphere. The temperature is held at a constant value throughout the experiment. The release or incorporation of oxygen is coupled with a change in the oxygen non-stoichiometry of the material and thus, according to the respective charge neutrality condition, also with a change of the electronic charge carrier concentration, both of which consequently affect the electrical conductivity of the sample [59].

Recording the conductivity as a measure for the change in oxygen non-stoichiometry is only valid if a correlation between these two quantities exists [35, 59, 60]. In most instances, depending on the experimental conditions, the assumption of a linear relationship is appropriate [59]. That is, if the change in oxygen content and the change in the electrical charge carrier concentration are linearly connected, the conductivity also changes proportionally as a result of the changing defect concentrations [59].

It is possible to extract the surface exchange coefficient, k_{chem}, as well as the chemical diffusion coefficient, D_{chem}, from the measured relaxation data since the oxygen exchange is based on two consecutive processes: 1) oxygen exchange at the gas-solid interface and 2) diffusion of atomic oxygen within the bulk of the material [35, 61]. Practically this is carried out by fitting the transient responses to an appropriate mathematical model, while k_{chem} and D_{chem} serve as fitting parameters. The mathematical modeling of the oxygen exchange will be discussed in subsection 2.2.2.

In addition, it should be mentioned that the experimental execution of the conductivity relaxation method requires the consideration of several factors. Firstly, the magnitude of the respective pO_2 steps should be small to ensure that the application of a linear exchange model, as discussed above, is valid [62]. Hence, the investigation of oxygen exchange kinetics by means of conductivity relaxation is restricted to conditions close to the equilibrium state. Secondly, depending on the reactor geometry (as well as experimental conditions and chosen material), a flush time correction of the theoretical equations might be necessary [63]. Thirdly, a simplification of the mathematical model, e.g. assuming a one-dimensional transport process, is only valid if the sample geometry is chosen accordingly. That is, the thickness of the sample needs to be sufficiently small compared to the remaining two sample dimensions in order to ensure that oxygen exchange is suppressed at the edges of the sample [64]. Lastly, material properties such as porosity and grain size might also influence the relaxation process and should therefore be considered [34].

2.2.2. Mathematical model

The following subsection will discuss the mathematical modeling of the oxygen exchange. The description will lead to a solution of the diffusion equation, which was derived by Crank [65].

Consider a plane sheet with thickness $2a$. Oxygen is incorporated and released through the plane faces of the sample. The sample thickness is small compared to the plane faces and thus, oxygen exchange through the edges can be neglected, which allows for modeling of a one-dimensional transport process. Initially, the oxygen concentration c_0 is uniformly distributed within the sample. When the pO_2 is switched, the sample will relax to a new constant concentration c_∞, which corresponds to the new pO_2 in the surrounding atmosphere. Figure 2.2 illustrates the situation under consideration. Note that, even though the initial and final concentrations are plotted, the progression of the concentration profile is not depicted.

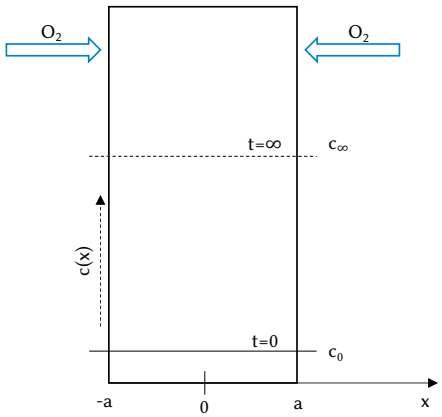

Figure 2.2.: Simple illustration of oxygen incorporation. Plane sheet geometry, sample thickness = $2a$. The initial oxygen concentration at the beginning of the experiment is denoted by c_0. The final oxygen concentration, which is attained when the sample has reached a new equilibrium state with the surrounding atmosphere, is denoted by c_∞.

The chemical diffusion of neutral oxygen atoms within the material can be described by Fick's 2nd law

$$\frac{\partial c}{\partial t} = D_{chem} \frac{\partial^2 c}{\partial x^2}, \tag{2.12}$$

which is a non-steady state, linear partial differential equation. The chemical diffusion coefficient is considered to be constant. The solution requires one initial condition as well as two boundary conditions. The boundary conditions for the surface exchange through the plane faces of the sample can be modeled as

$$j_O(\pm a, t) = -D_{chem} \left.\frac{\partial c}{\partial x}\right|_{x=\pm a} = \pm k_{chem} \left[c(\pm a, t) - c_\infty\right], \tag{2.13}$$

where j_O and $c(\pm a, t)$ denote the oxygen mass flux density and the momentary oxygen concentration. The surface exchange coefficient is considered to be a first-order rate constant. Furthermore, due to the symmetry of the sample at $x = 0$, the concentration gradient reads

$$\left.\frac{\partial c}{\partial x}\right|_{x=0} = 0, \tag{2.14}$$

at all times $t \geq 0$. The initial condition is

$$c(x, t = 0) = c_0, \quad -a < x < a. \tag{2.15}$$

In order to simplify the subsequent calculations, the following substitution is used [61]

$$\tilde{c}(x, t) = c(x, t) - c_\infty, \tag{2.16}$$

which yields

$$\frac{\partial \tilde{c}}{\partial t} = D_{chem} \frac{\partial^2 \tilde{c}}{\partial x^2} \tag{2.17}$$

for the diffusion equation. The transformed boundary and initial conditions are presented in Equation (2.18) - Equation (2.20).

$$-D_{chem} \left.\frac{\partial \tilde{c}}{\partial x}\right|_{x=a} = k_{chem} \cdot \tilde{c}(a, t) \tag{2.18}$$

$$\left.\frac{\partial \tilde{c}}{\partial x}\right|_{x=0} = 0 \tag{2.19}$$

$$\tilde{c}(x, t = 0) = c_0 - c_\infty, \quad -a < x < a \tag{2.20}$$

A solution of Equation (2.17) may be obtained by assuming that the variables are separable [65]. Therefore it is assumed that $\tilde{c}(x, t)$ is equal to the product of a function T, that only depends on t, and a function X, which only depends on x.

$$\tilde{c}(x, t) = T(t) \cdot X(x) \tag{2.21}$$

Applying Equation (2.21) to Equation (2.17) and rearranging the obtained expression yields

$$\frac{dT}{T} = \frac{D_{chem}}{X} \cdot \frac{d^2X}{dx^2} = -D_{chem}\lambda^2, \tag{2.22}$$

where the left side of the equation depends only on t and the right side only depends on x. Consequently, both sides must be equal to the same constant, which is denoted by $-D_{chem}\lambda^2$. λ is the eigenvalue. The negative sign is chosen to ensure that restricted solutions are obtained for $t \to \infty$. Solving the two ordinary differential equations yields the general solution of Equation (2.17)

$$\tilde{c}\,(x,t) = (A \cdot sin\,(\lambda x) + B \cdot cos\,(\lambda x)) \cdot exp\left(-\lambda^2 D_{chem} t\right). \tag{2.23}$$

The parameters A, B and λ are subsequently determined by the boundary and the initial conditions. The application of Equation (2.19) to Equation (2.23) yields

$$\left.\frac{\partial \tilde{c}}{\partial x}\right|_{x=0} = 0 \quad \rightarrow \quad A = 0. \tag{2.24}$$

Furthermore, applying the boundary condition (Equation (2.18)) to Equation (2.23) yields

$$-D_{chem}\left.\frac{\partial \tilde{c}}{\partial x}\right|_{x=a} = k_{chem} \cdot \tilde{c}\,(a,t) \quad \rightarrow \quad \lambda \cdot tan\,(\lambda) = \lambda_n \cdot tan\,(a\lambda_n) = \frac{k_{chem}}{D_{chem}}, \tag{2.25}$$

which represents a separate condition for the eigenvalues. The subscript m is used to show that an infinite number of eigenvalues exist. Subsequently, the x-coordinate a is removed from said condition by substitution with [61]

$$\alpha_n = a\lambda_n \quad \rightarrow \quad \alpha_n \cdot tan(\alpha_n) = \frac{ak_{chem}}{D_{chem}} = L, \tag{2.26}$$

where L is a dimensionless parameter. Equation (2.26) is a transcendental equation. Note that the eigenvalues α_n ($\widehat{=}$ roots of Equation (2.26)) have to be approximated by a numerical method [66].

The linearity of Equation (2.17) allows the application of the superposition principle and the complete solution of Equation (2.17) is therefore expressed by the following sum (Fourier series)

$$\tilde{c}\,(x,t) = \sum_{n=1}^{\infty} B_n \cdot cos\left(\frac{\alpha_n}{a}x\right) \cdot exp\left(-\frac{\alpha_n^2 D_{chem} t}{a^2}\right). \tag{2.27}$$

The coefficients B_n are determined by the initial condition.

$$\tilde{c}\,(x, t=0) = c_0 - c_\infty = \sum_{n=1}^{\infty} B_n \cdot cos\left(\frac{\alpha_n}{a}x\right) \quad \Big| \cdot \int_0^a cos\left(\frac{\alpha_m}{a}x\right) dx \tag{2.28}$$

Using the orthogonality relation

$$\int_0^a cos\left(\frac{\alpha_m}{a}x\right) cos\left(\frac{\alpha_n}{a}x\right) dx = \begin{cases} 0, & m \neq n \\ \frac{a}{2} \cdot \frac{\alpha_n^2 + L^2 + L}{\alpha_n \cdot L}, & m = n \end{cases}, \tag{2.29}$$

yields [61]

$$B_n = (c_0 - c_\infty) \cdot \frac{2 \cdot L}{(\alpha_n^2 + L^2 + L) \cdot cos\,(\alpha_n)} \quad . \tag{2.30}$$

Substituting Equation (2.30) in Equation (2.27) as well as taking Equation (2.16) into account yields the complete solution, that satisfies the boundary conditions as well as the initial condition,

$$c\,(x,t) = c_\infty + (c_0 - c_\infty) \cdot \sum_{n=1}^{\infty} \frac{2 \cdot L \cdot cos\,(\alpha_n x/a)}{(\alpha_n^2 + L^2 + L) \cdot cos\,(\alpha_n)} \cdot exp\left(-\frac{\alpha_n^2 D_{chem} t}{a^2}\right). \tag{2.31}$$

Finally, the normalized concentration profile [65] is obtained by rearranging Equation (2.31)

$$\frac{c\,(x,t) - c_0}{c_\infty - c_0} = 1 - \sum_{n=1}^{\infty} \frac{2 \cdot L \cdot cos\,(\alpha_n x/a)}{(\alpha_n^2 + L^2 + L) \cdot cos\,(\alpha_n)} \cdot exp\left(-\frac{\alpha_n^2 D_{chem} t}{a^2}\right). \tag{2.32}$$

If the change in electrical conductivity and the change in oxygen content are correlated as described in subsection 2.2.1, it is valid to integrate Equation (2.32) along x, which yields the normalized conductivity profile

$$\frac{\sigma(t)-\sigma_0}{\sigma_\infty-\sigma_0} = 1 - \sum_{n=1}^{\infty} \frac{2L^2}{\alpha_n^2\left(\alpha_n^2+L^2+L\right)} \cdot exp\left(-\frac{\alpha_n^2 D_{chem} t}{a^2}\right). \tag{2.33}$$

Note that, based on the aforementioned correlation, Equation (2.33) represents the total amount of exchanged oxygen [35, 64].

2.2.3. Differences between mixed control, surface limited and diffusion limited relaxation kinetics

In subsection 2.2.1 it was argued that the transport parameters, k_{chem} and D_{chem}, could be evaluated from the measured relaxation data as the oxygen exchange is based on two consecutive processes. This statement needs to be specified since the evaluation of both parameters is only valid, if both transport processes contribute to the relaxation behavior of the sample. In this case the relaxation process is under mixed control [63] and Equation (2.33) can be used to extract k_{chem} and D_{chem}.

If, however, the relaxation behavior is entirely dominated by one of two consecutive processes, only the respective transport parameter can be obtained from the data.

In case of surface limitation, the diffusion within the material is much faster than the surface exchange process. That is, the change in oxygen content following a pO_2 step is rapidly balanced within the bulk of the material. In this instance, Equation (2.33) reduces to the following equation

$$\frac{\sigma(t)-\sigma_0}{\sigma_\infty-\sigma_0} = 1 - exp\left(-\frac{k_{chem} t}{a}\right). \tag{2.34}$$

Consequently, only the surface exchange coefficient can be evaluated from the relaxation data.

If the relaxation process is limited by diffusion within the material, the oxygen exchange at the surface is much faster than the diffusion process. The surface of the material attains the equilibrium concentration, c_∞, instantly, which results in a concentration gradient inside the

sample. The reduced version of Equation (2.33) in this case is

$$\frac{\sigma(t)-\sigma_0}{\sigma_\infty-\sigma_0} = 1 - \frac{8}{\pi^2}\sum_{n=1}^{\infty}\frac{1}{(2n+1)^2}\cdot exp\left(-\frac{(2n+1)^2\pi^2 D_{chem}t}{4a^2}\right). \tag{2.35}$$

Only D_{chem} can be derived from a respective transient response.

The distinction between the three regimes depends on the value of L (see Equation (2.26)), which is unknown at the beginning of an experiment [34]. A range for L, within which an evaluation for both transport parameters is valid, was derived by Otter et al. [63]. The practical application of said interval will be discussed in connection with the fitting approach in subsection 3.4.2.

The characteristic length

$$L_c = \frac{D_{chem}}{k_{chem}} \tag{2.36}$$

allows for a distinction between surface and diffusion limited relaxation processes for a given sample thickness [63]. The relaxation process is mostly limited by the surface exchange, if $a \ll L_c$ [63]. Conversely, if $a \gg L_c$, diffusion limitation will largely prevail [63]. Note that L_c depends on oxygen partial pressure as well as on temperature since the underlying transport processes are pO_2 and temperature dependent [34].

2.3. Oxygen transport

2.3.1. Chemical diffusion

In context of a conductivity relaxation experiment, the transport of neutral oxygen atoms within the bulk of the material is a chemical diffusion process. Chemical diffusion of oxygen is facilitated by ambipolar transport of charge carriers driven by a gradient in the oxygen chemical potential [67, 68]. Since charged carriers are involved in the transport of the mobile neutral species 'O', charge neutrality needs to be maintained throughout the transport process [22].

Assuming that only two mobile charge carriers are present and furthermore, neglecting trapping effects due to redox active impurities or dopants [69] (e.g. Fe in Fe:STO), the components O^{2-} and e^- are transported (in opposite directions) via ionic and electronic charge carriers [30], which are, in case of STO and LSC, oxygen vacancies and electron holes. Expressing the transport process as a position change from x to x' yields [22]

$$O^{2-}(x) \rightleftharpoons^{V_O^{\bullet\bullet}} O^{2-}(x'), \tag{2.37}$$

$$2\,e^-(x) \rightleftharpoons^{2h^{\bullet}} 2\,e^-(x'). \tag{2.38}$$

As already mentioned in section 2.2, the application of the conductivity relaxation method is restricted to conditions close to the equilibrium state and thus, only small driving forces ($\Delta\mu_O$) can be applied. Following this, it is valid to start the derivation of the chemical diffusion coefficient by using the linear flux equation [30]

$$j_k = -\frac{\sigma_k}{z_k^2 F^2}\nabla\tilde{\mu}_k, \tag{2.39}$$

where j, σ and z denote the molar flux density, the conductivity and the charge number. Furthermore, F denotes the Faraday constant and $\tilde{\mu}$ denotes electrochemical potential. The subscript k points to the respective charge carrier. In Equation (2.39) cross coefficients, which would include contributions stemming from interference between the two transport processes shown above, are neglected [30]. The electrochemical potential is defined as

$$\tilde{\mu}_k = \mu_k + z_k F\phi, \tag{2.40}$$

where μ and ϕ denote the chemical potential and the local electric potential, respectively. Therefore, the following expressions are obtained for the component flux densities

$$j_{O^{2-}} = -\frac{\sigma_{ion}}{4F^2}\nabla\tilde{\mu}_{O^{2-}} = -\frac{\sigma_{ion}}{4F^2}\left(\nabla\mu_{O^{2-}} - 2F\nabla\phi\right), \tag{2.41}$$

$$j_{e^-} = -\frac{\sigma_{eon}}{F^2}\nabla\tilde{\mu}_{e^-} = -\frac{\sigma_{eon}}{F^2}\left(\nabla\mu_{e^-} - F\nabla\phi\right). \tag{2.42}$$

The two flux densities are coupled by the electroneutrality condition

$$\sum_k z_k j_k = 2j_{O^{2-}} + j_{e^-} = 0. \tag{2.43}$$

Isolating ϕ in Equation (2.41) as well as taking Equation (2.43) into account yields the following expression for $j_{O^{2-}}$,

$$j_{O^{2-}} = -\frac{1}{4F^2} \cdot \frac{\sigma_{ion} \cdot \sigma_{eon}}{\sigma_{ion} + \sigma_{eon}} \cdot \left(\nabla \mu_{O^{2-}} - 2\nabla \mu_{e^-}\right). \tag{2.44}$$

It is possible to rewrite Equation (2.44) in terms of the mobile neutral species 'O' [70]. Therefore the equilibrium between neutral atomic oxygen, oxide ions and electrons has to be considered (Equation (2.45)).

$$O + 2e^- \rightleftharpoons O^{2-} \tag{2.45}$$

Expressing the equilibrium condition ($\sum_k \mu_k = 0$) for this reaction

$$\mu_O = \tilde{\mu}_{O^{2-}} - 2\tilde{\mu}_{e^-}, \tag{2.46}$$

$$\mu_O = \mu_{O^{2-}} - 2F\phi - 2\mu_{e^-} + 2F\phi, \tag{2.47}$$

as well as expressing the respective gradient of the equilibrium condition, reveals that the chemical potential gradient of oxygen equals the bracketed difference in Equation (2.44)

$$\nabla \mu_O = \nabla \mu_{O^{2-}} - 2\nabla \mu_{e^-}. \tag{2.48}$$

Thus, the original molar flux density (Equation (2.44)) is rewritten in terms of the mobile neutral species 'O'

$$j_O = j_{O^{2-}} = -\frac{1}{4F^2} \cdot \frac{\sigma_{ion} \cdot \sigma_{eon}}{\sigma_{ion} + \sigma_{eon}} \cdot \nabla \mu_O. \tag{2.49}$$

Assuming furthermore that the transport proceeds only in one dimension as well as taking the chain rule into account (μ is a function of the concentration), yields

$$j_O = -\frac{1}{4F^2} \cdot \frac{\sigma_{ion} \cdot \sigma_{eon}}{\sigma_{ion} + \sigma_{eon}} \cdot \frac{\partial \mu_O}{\partial c_O} \cdot \frac{\partial c_O}{\partial x}. \tag{2.50}$$

Comparing Equation (2.50) to Fick's first law, again, under the assumption of one-dimensional diffusion,

$$j = -D\frac{\partial c}{\partial x}, \tag{2.51}$$

shows that chemical diffusion coefficient corresponds to

$$D_{chem} = \frac{1}{4F^2} \cdot \frac{\sigma_{ion} \cdot \sigma_{eon}}{\sigma_{ion} + \sigma_{eon}} \cdot \frac{\partial \mu_O}{\partial c_O}. \tag{2.52}$$

Equation (2.52) shows that 1) both ionic and electronic charge carriers contribute to D_{chem} and 2) that the chemical diffusion coefficient is also dependent on the chemical capacitance $(\partial \mu_O / \partial c_O)^{-1}$, which is a measure for the stoichiometric change, that a sample undergoes following a pO_2 step in the surrounding atmosphere [22]. It is important to note that the chemical diffusion coefficient measures the mobility of the mobile defects in a respective material [68] since a change in the oxygen content, as already mentioned in subsection 2.2.1, is coupled with a change of the charge carrier concentration according to the respective electroneutrality condition.

It should be mentioned that even though D_{chem} in Equation (2.52) is expressed in terms of the component O, it is also possible to rewrite the expression in terms of O^{2-}/e^- (Equation (2.48)), which then allows for a separation of ionic and electronic terms. Moreover, this expression can be transformed to obtain a correlation between D_{chem} and the corresponding mobile charge carriers. Resulting simplifications due to dilute charge carrier concentrations are not given in this work, but can be found in the literature [68–70].

2.3.2. Surface exchange

The oxygen exchange at the gas-solid interface is a multistep reaction [22], which involves, inter alia, the following steps: oxygen transport in the gas phase to the sample, oxygen adsorption at the sample surface, oxygen dissociation and ionization and finally, incorporation of oxygen into the first layer of the material into oxygen vacancies [22, 70]. The mathematical model for the oxygen flux across the gas-solid interface for conditions close to equilibrium state was already given in subsection 2.2.2 (see Equation (2.13)). This expression contained the surface exchange coefficient k_{chem} as a proportionality factor.

The surface exchange coefficient can be linked to the reaction mechanism under the assumptions that 1) one step of the aforementioned reaction series determines the overall rate of the surface exchange ($\widehat{=}$ rate determining step, *rds*) as well as that 2) the other reaction steps are in quasi-equilibrium. This shall be briefly illustrated by means of a first order reaction

$$\mathrm{A} \rightleftharpoons \mathrm{B}, \tag{2.53}$$

which for the further explanation constitutes the *rds*. It is noted that theoretically each of the mentioned reaction steps can limit the surface exchange. Which step of the series constitutes the *rds* depends on the respective material as well as on the experimental conditions under consideration. Based on the aforementioned assumptions, the flux across the interface, j, can be related to reaction rate of the rate determining step by [22, 28]

$$\mathscr{R} = \mathscr{R}_{rds} = \frac{j}{2a} = \frac{d[\mathrm{B}]}{dt} = \overrightarrow{k}[\mathrm{A}] - \overleftarrow{k}[\mathrm{B}] = -\overleftarrow{k}[\mathrm{B}]\left(1 - \exp\left(\frac{-\Delta_r G}{RT}\right)\right), \tag{2.54}$$

where $2a$ equals, again, the sample thickness. $\mathscr{R}$, $\overrightarrow{k}$ and $\overleftarrow{k}$ denote the reaction rate of the *rds* and the rate constants of the forward and the backward reaction, respectively. Furthermore, $\Delta_r G$ denotes the Gibbs free energy of the reaction ($\Delta_r G = \mu_A - \mu_B$) and represents the driving force of the reaction. The reaction rate approaches zero close to the equilibrium state and Equation (2.54) becomes [28]

$$\frac{j}{2a} \approx \overrightarrow{k}[\mathrm{A}]_{eq}\left(\frac{\delta\mu}{RT}\right) = \overleftarrow{k}[\mathrm{B}]_{eq}\left(\frac{\delta\mu}{RT}\right) = \frac{\mathscr{R}_0}{RT}\left(\frac{\partial\mu}{\partial c}\delta c\right), \tag{2.55}$$

with

$$\mathscr{R}_0 = \sqrt{\overrightarrow{k}[\mathrm{A}]_{eq}\,\overleftarrow{k}[\mathrm{B}]_{eq}}. \tag{2.56}$$

Assuming proximity to the equilibrium state allowed for linearization of the exponential term in Equation (2.54). The subscript '*eq*' refers to the respective concentrations of species A and B in equilibrium. $\delta\mu$ denotes the deviation from equilibrium, that is, $\delta\mu$ measures the difference of the momentary value and the equilibrium value of μ. Furthermore, it contains contributions from both species, that is, $\delta\mu = (\delta\mu_A - \delta\mu_B)$. The driving force was further expressed in terms of the concentration deviation from the equilibrium state, δc. Both quantities, $\delta\mu$ and δc, refer to the first layer of the material [30].

Clearly, Equation (2.55) resembles Equation (2.13). However, the proportionality factor in this instance is not the surface exchange coefficient but the effective rate constant, k_r, which equals

$$k_r = \frac{\mathscr{R}_0}{RT} \cdot \frac{\partial \mu}{\partial c}, \tag{2.57}$$

and which is furthermore linked to the surface exchange coefficient, k_{chem}, by the sample thickness ($d = 2a$)

$$k_r = \frac{k_{chem}}{d}. \tag{2.58}$$

Finally, expressing the surface exchange coefficient for the oxygen exchange at the sample surface according to Equation (2.57) as well as taking Equation (2.58) into account yields [28, 30, 71]

$$k_{chem} \propto d \cdot \frac{\mathscr{R}_0}{RT} \cdot \frac{\partial \mu_O}{\partial c_O}, \tag{2.59}$$

Equation (2.59) shows that, on the one hand, the reaction mechanism contributes to the surface exchange coefficient in form of $\mathscr{R}_0$ and, on the other hand, that k_{chem} also depends on the defect chemistry within the first layer of the material as the chemical capacitance, $(\partial \mu_O / \partial c_O)^{-1}$, is also present in Equation (2.59) [22]. In this context it should be mentioned that the steps preceding and succeeding the rate determining step contribute to $\mathscr{R}_0$ through mass action laws [28, 30].

2.4. Van der Pauw method

The van der Pauw method is a four point direct current measurement technique, which can be used to determine the specific resistivity of a flat sample of arbitrary shape [72, 73]. Application of the method requires that the sample 1) is singly connected and 2) has a uniform thickness [72, 73]. The four electrical contacts need to be sufficiently small and should be, ideally, positioned alongside the circumference of the sample [72, 73]. In this work, mainly square sample geometries were used. Figure 2.3 illustrates the arrangement of the four electrical contacts in case of a square sample.

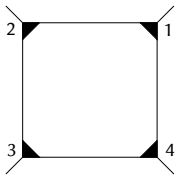

Figure 2.3.: Top view of the square sample geometry. The electrical contacts are placed at the four corners of the sample.

The resistance R_{1234} is defined by

$$R_{1234} = \frac{U_4 - U_3}{I_{12}}, \tag{2.60}$$

where I_{12} denotes the current, that enters and leaves the sample at contact 1 and 2, respectively. The numerator of Equation (2.60) is the measured potential difference, U_{34}, between contact 4 and 3. Figure 2.4 depicts the configuration, in which the resistance R_{1234} is measured.

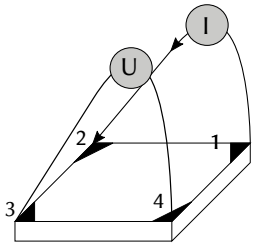

Figure 2.4.: Measurement of the resistance R_{1234}. I denotes the direct current source. U denotes the measurement of the potential difference between contact 4 and 3.

Switching the entry point of the current by 90 °C yields the resistance

$$R_{2341} = \frac{U_1 - U_4}{I_{23}}. \tag{2.61}$$

Van der Pauw demonstrated that the following relation holds for any sample shape [72].

$$exp\left(-\frac{\pi d}{\rho} R_{1234}\right) + exp\left(-\frac{\pi d}{\rho} R_{2341}\right) = 1 \tag{2.62}$$

In Equation (2.62) d and ρ denote the sample thickness and the specific resistivity, respectively. Since R_{1234}, R_{2341} and d are measurable and therefore known quantities, the solution for ρ can be expressed from Equation (2.62) in the following form

$$\rho = \frac{\pi d}{ln\,(2)} \cdot \frac{R_{1234} + R_{2341}}{2} \cdot f\left(\frac{R_{1234}}{R_{2341}}\right), \tag{2.63}$$

where f is a function of the resistances R_{1234}/R_{2341}. An approximation of f by

$$f \approx 1 - \left(\frac{R_{1234} - R_{2341}}{R_{1234} + R_{2341}}\right)^2 \cdot \frac{ln\,(2)}{2} - \left(\frac{R_{1234} - R_{2341}}{R_{1234} + R_{2341}}\right)^4 \cdot \left(\frac{(ln\,(2))^2}{4} - \frac{(ln\,(2))^3}{12}\right), \tag{2.64}$$

is valid, if the values of R_{1234} and R_{2341} are similar [72].

Preis, Holzinger, and Sitte demonstrated that the van der Pauw method can be used for conductivity relaxation measurements on mixed ionic and electronic materials [59]. A prerequisite for the application of the van der Pauw technique is that the diffusion of the mobile species within the material is restricted to the direction perpendicular to the current flow [59]. Thus, the considered oxygen exchange process needs to be one-dimensional. An assessment of whether or not a one-dimensional transport process can be expected for a particular sample was given by Preis based on a comparison between relaxation curves for mass transport (expressing the total amount of exchanged oxygen) and normalized conductivity profiles [64]. If the aforementioned curves coincide, the assumption of one-dimensional oxygen exchange processes is valid. Close agreement between the curves is anticipated, if the diameter to thickness ratio is 10 (or higher) [64].

3. Experimental

3.1. Sample preparation

3.1.1. STO and Fe:STO single crystals

Strontium titanate (CrysTec GmbH, Germany) and iron doped strontium titanate single crystals (Alineason, 0.16 mol%) were used. Both specimens were polished on both sides, had an (100) orientation and the dimensions were 10 mm x 10 mm x 0.5 mm. Platinum paste was used to brush the electrical contacts onto the surface of the single crystals in the four corners of the square samples. The samples were then dried on a heating plate for 15 min at 300 °C. To ensure good adhesion of the Pt paste (Tanaka Europe GmbH) to the single crystal and to achieve a defined concentration of the oxygen vacancies in the material the samples were sintered for 2 h at 900 °C and afterwards annealed for 5 h at 600 °C. This thermal treatment was done in air.

3.1.2. Polycrystalline LSC

$La_{0.6}Sr_{0.4}CoO_{3-\delta}$ powder was synthesized by the Pechini method [74]. Figure 3.1 shows the overall preparation process from the synthesis of the LSC powder to the final specimen used in the experiments. The single steps of the process will be explained in detail in the following section.

a) $La_{0.6}Sr_{0.4}CoO_{3-\delta}$ powder synthesis

Table 3.1 shows the raw materials that were used to synthesize approximately 14.36 g of LSC powder. La_2O_3 (99.999 % trace metals, Sigma Aldrich) was dissolved in HNO_3 (70 %, purified by redistillation, ≥ 99.999 % trace metals basis, Sigma Aldrich). $SrCO_3$ (≥ 99.9 % trace metals, Sigma Aldrich) and Co (99.995 % trace metals basis, granular, Sigma Aldrich) were added

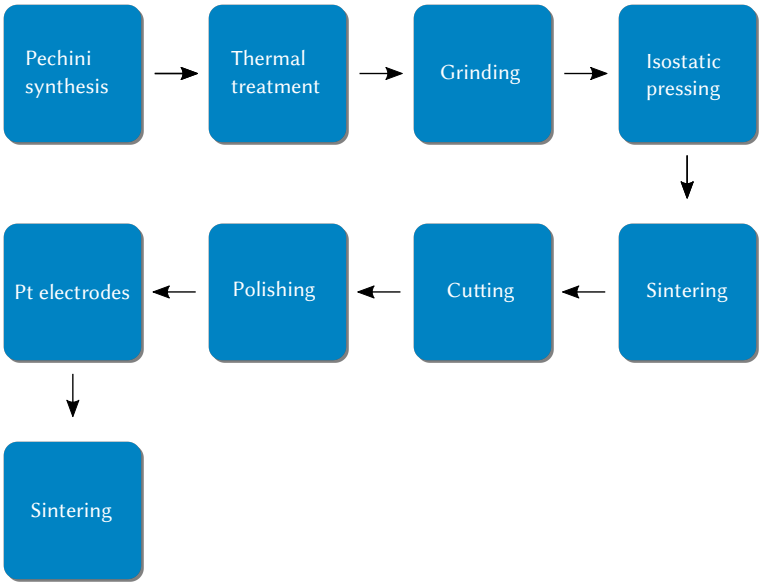

Figure 3.1.: Flowchart showing the single steps of the preparation process of polycrystalline $La_{0.6}Sr_{0.4}CoO_{3-\delta}$.

together. Afterwards the dissolved La_2O_3 was added step-by-step to the mixture of $SrCO_3$ and Co. To ensure that all La_2O_3 was transferred to the mixture, the beaker which contained the La_2O_3 solution was rinsed repeatedly with distilled water that was added to the mixture. Finally, citric acid monohydrate ($\geq$ 99.0 %, Sigma Aldrich), which acted as an chelating agent, was added and the solution was then heated under reflux conditions while stirring continuously with a magnetic stirrer. Upon evaporation, the viscosity of the mixture increased and bubbles ascending to the top were scarcely visible, the stirring was stopped and the magnetic stirring bar removed. Afterwards the heating of the gel was continued. Since the gel didn't completely combust as desired, the beaker had to be heated with a Bunsen burner in order to eliminate the remaining organic components from the mixture. The resulting amorphous powder was then crystallized by thermal treatment in air in a chamber furnace. The temperature setpoints were 300 °C, 500 °C, 1000 °C and the dwell times for each setpoint were 15 min, 1 h and 2 h, respectively. The furnace was heated with different heating rates of 5 °C/min, 2 °C/min and 5 °C/min. After the thermal treatment the powder was ground.

Table 3.1.: Components used in Pechini synthesis

La_2CO_3	6.5067 g
Co	3.9232 g
$SrCO_3$	3.9307 g
$C_6H_8O_7 \cdot H_2O$	30.8 g

b) Preparing samples for experiments

The obtained LSC powder was isostatically pressed into pellets at 3.1 kbar for 1 min. Then the pressed pellets were placed into a platinum crucible on an LSC powder bed and sintered for 12 h at 1200 °C. The heating and the cooling rate were both 5 °C/min. Afterwards the LSC pellets were cut into circular discs with thicknesses varying between 0.62 mm and 1.3 mm. The diameter of all cut samples was approximately 11 mm. To obtain homogeneously thick samples with plane surfaces the samples were finely ground using a MD Piano 1200 resin bonded diamond disc (Struers) and a MD Largo composite disc (Struers). Two polishing steps followed with two different polishing cloths: MD Dac and MD Nap (Struers). These steps were carried out using a grinding and polishing machine (TegraPol-31, Struers). After these preparation steps the specimens were mirror-polished with thicknesses between 0.46 mm and 0.56 mm.

c) Electrical contacts

Four electrical contacts were brushed onto the samples with platinum paste. They were arranged at the edge, 90 ° from each other. The samples were then sintered for 2 h at 850 °C in air with a heating and cooling rate of 5 °C/min.

3.1.3. LSC thin films

a) Pulsed laser deposition

$La_{0.6}Sr_{0.4}CoO_{3-\delta}$ thin films were produced by pulsed laser deposition (PLD). As substrates (100) oriented MgO, $LaAlO_3$ (LAO) and $SrTiO_3$ (STO) single crystals, that were polished on one side, were used. All single crystals had a size of 10 mm x 10 mm x 0.5 mm. The used LSC target was prepared in-house via the Pechini method as described above. For ablation of the target a KrF excimer laser (COMPex Pro 201F) was used. A list of important deposition parameters is given in Table 3.2.

Table 3.2.: PLD parameters

Target distance	6 cm
Laser energy	400 mJ/pulse
Laser wavelength	248 nm
Pulse frequency	1 Hz
Oxygen partial pressure	0.04 mbar

LSC films with thicknesses of 10 nm, 20 nm and 40 nm were prepared. Table 3.3 shows the time needed to deposit the desired film thickness under the conditions mentioned in Table 3.2. The PLD chamber was heated at a fixed heating rate and the surface temperature of the sample was measured with a pyrometer, which was calibrated with the emissivity ϵ of yttria-stabilized zirconia (YSZ). At 600 °C the deposition was started. Since LSC has a different ϵ, the temperature increased to approximately 650 °C during the deposition. After the deposition was completed the temperature was lowered with a rate of 10-12 °C/min.

Table 3.3.: Deposition time for different LSC film thicknesses

Desired film thickness	10 nm	20 nm	40 nm
Deposition time	500 s	1000 s	2000 s

b) Electrical contacts

The electrical contacts were brushed onto the corners of the square surface of the film with platinum paste. Afterwards the samples were put onto a Al_2O_3 plate which was then placed onto a heating plate to dry the paste for 15 min to 20 min. The temperature of the heating plate was approximately 120 °C. This preparation step had to be carried out a number of times because the adhesion between the LSC film and the Pt paste wasn't sufficient enough. After some time of being exposed to elevated temperatures during the experiments the Pt contacts would delaminate and fall off. A higher temperature sintering step as done for the (Fe:)STO single crystals and the LSC pellets (see subsection 3.1.1 and subsection 3.1.2) was avoided because Sr segregation to the surface of the LSC film had to be prevented [14].

3.2. Material characterization

3.2.1. X-ray diffraction

The LSC thin films were analyzed via X-ray diffraction using an Empyrean multipurpose diffractometer (Malvern Panalytical, Netherlands/United Kingdom). θ-2θ-scans as well as reciprocal space maps were recorded. A Cu anode was used and the operating voltage and tube current were 45 kV and 40 mA, respectively. During the measurements the Cu-$K_{\alpha 2}$ emission was cut from the incident beam with a hybrid monochromator 2XGe(220). Detection of the diffracted beam was done with a GaliPIX3D area detector (Malvern Panalytical, Netherlands/United Kingdom).

3.2.2. Surface analysis via profilometry

Using the van der Pauw technique to measure the resistivity of a specimen requires the knowledge of the exact thickness of said specimen (see section 2.4). Therefore the film thicknesses of the LSC films were measured with a DektakXT stylus profilometer (Bruker, USA) to check if the deposited film thicknesses were in agreement with the desired film thicknesses mentioned in Table 3.3. Line scans with a stylus force of 3 mg were performed. Figure 3.2 shows two samples that were used to measure the film thickness.

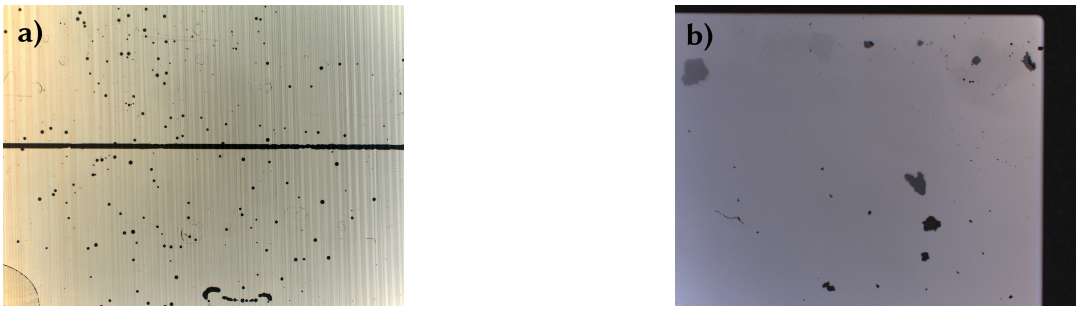

Figure 3.2.: Top view of samples used for surface analysis: **a)** A line across the whole width of the thin film was prepared by photolithography and chemically etched afterwards. The microscope image shows the sample after the etching process. **b)** The surface of the sample isn't completely covered with LSC. Pinholes in the surface after pulsed laser deposition are visible.

3.3. Electrical characterization

3.3.1. Van der Pauw measurements

All prepared samples were electrically characterized using the van der Pauw technique. [72, 73]

a) Measurement setup

Figure 3.3 shows an overview of the experimental setup. The experimental setup included a sample holder made out fused silica, which was mounted into a threaded flange. A type K thermocouple, which was connected to a 2000 DMM multimeter (Keithley, USA), was placed approximately 1 cm below the sample holder to measure the temperature during the experiments. To achieve a defined gas atmosphere a fused silica tube was put over the sample holder which was then screwed to the flange.

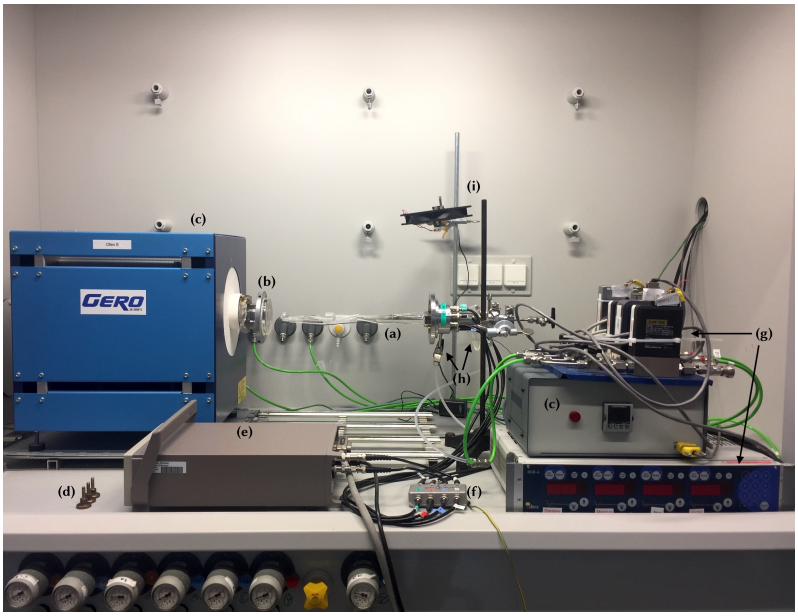

Figure 3.3.: Van der Pauw measurement setup: **(a)** fused silica sample holder, **(b)** outer fused silica tube, **(c)** tube furnace and PID controller, **(d)** screws, **(e)** multimeter for voltage measurement, **(f)** switch box, **(g)** mass flow controllers with control unit, **(h)** gas inlet and outlet, **(i)** ventilator for cooling the flange

All experiments were done in desired O_2-N_2 mixtures (both Alphagaz^{TM} 1, Air liquide, Austria). The gas flow was controlled by two mass flow controllers (MFC) which were connected to a 4-channel Area Rod-4 power and readout unit. This control unit was used because it allowed automated application of pO_2 steps to the system. Heating of the samples was done with a tube furnace and the furnace temperature was controlled by an Eurotherm PID controller, which was connected to the furnace. For polarization of the sample the van der Pauw technique requires a direct current (DC) source. Therefore a 2410 source-meter-unit (SMU) (Keithley, USA) was connected to two adjacent electrodes and operated in a source voltage, measure current mode. The voltage on the remaining two contacts was measured with a second 2000 DMM multimeter. Additionally a switch box was installed into the circuit, which allowed to change the measurement configuration from 1234 to 2341 (i.e. a 90° rotation of electric contacting). All electrical wiring inside the reactor including the four tips, that contacted the sample, were made of platinum. In Figure 3.4 a detailed view of the sample holder is shown.

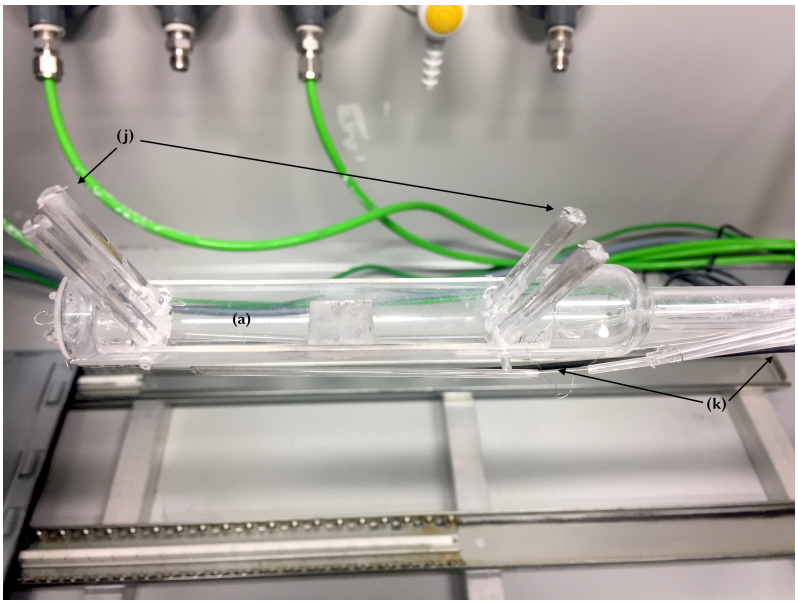

Figure 3.4.: Detailed view of the sample holder: **(a)** fused silica sample holder, **(j)** four Pt tips for contacting of the sample, **(k)** thermocouple

b) Workflow

The general workflow was the same for all analyzed materials. First the sample was placed into the sample holder. To avoid contact resistances the Pt tips were brushed with Pt paste before contacting the sample. The tube furnace, which was mounted to sliding rails and also

carried the outer fused silica tube, was carefully slid over the sample holder and the outer tube was then screwed to the flange. Afterwards a total gas flow of 9.9 l/h was employed and the tube furnace was heated to the desired temperature setpoint.

After the temperature inside the reactor remained at a constant value for at least an hour the correction factor f was measured. Therefore voltage was applied with the SMU and the current I_{12} between the contacts 1 and 2 and the voltage U_{43} between the contacts 4 and 3 were measured. This was done four times. The total time for each run was 40 s. After 20 s the polarization of the applied voltage was changed. The measured data was recorded with a rate of one point per 0.1 s. By flipping the switch of the switch box the entry point of the current was changed by 90 °. Hence, current I_{23} and voltage U_{14} were measured in this mode. This measurement was also done four times under the same conditions described above. f was averaged from these eight measurements and all following calculations were done with this average value.

Afterwards the actual conductivity relaxation measurement was started. Since f had already been quantified, the experiment could be executed without changing the mode of the switch box. pO_2 steps ($\leq$ factor 1.67) were applied both in reducing and oxidizing direction in a pO_2 range between 0.015 bar and 0.2 bar. This procedure was repeated at least once to obtain information about the relaxation behavior of the examined materials, e.g. if the steps from reduction and oxidation runs were equal. The duration between the single pO_2 steps had to be chosen carefully since the evaluation of data obtained from relaxation experiments is based on the premise that the sample reaches a new equilibrium state. Generally, the duration after an applied pO_2 step until the sample is again at equilibrium with the surrounding gas atmosphere is a function of temperature. At higher temperatures the process will be faster and the time needed to run an experiment will be shortened. Therefore tests, where time of the re-equilibration process at a certain temperature was guessed and if necessary, was adjusted, were run for each type of sample.

The data during the measurements were recorded with a time resolution of one point per second. Due to observed drifting in the recorded data the polarization of the applied voltage was changed more than once to suppress the drift within the transient response in case of some LSC thin films. Only for two experiments, that were carried out on the Fe:STO single crystal, the polarization was only changed once in the middle of the chosen time duration between the initial and new equilibrium pO_2 in all other experiments. The applied voltage varied between the different sample types but was always chosen based on: a) that 10% of the applied input voltage could be read from the multimeter and b) that the input power was less than 0.01 W

to avoid Joule heating of the sample. Table 3.4 presents the temperature ranges at which the different materials were measured as well as the voltage values which were applied during the experiments.

Table 3.4.: Summary of the experimental conditions

	(Fe:)STO	**polycrystalline LSC**	**LSC thin films**
Temperature range	542 °C -767 °C	513 °C - 715 °C	143 °C -466 °C
Applied voltage	0.05 V	0.05 V - 4 V	0.1 V

c) Calibration of mass flow controllers

As mentioned above, two mass flow controllers were used to mix O_2 and N_2 in appropriate ratios. The calibration was done by measuring the time needed for a certain volume of water to be displaced by a utilized gas flow. This was done at several setpoints of each mass flow controller. Figure 3.5 shows the measured data points and the calibration curve that was fitted to the data. The flow rate of O_2 was measured more thoroughly in the range between 0 % and 20 % so that oxygen partial pressure switches in this window could be accomplished with a higher accuracy. In addition, Figure 3.5a reveals that the achievable N_2 flow rate is smaller than the achievable O_2 flow rate. Hence, the total gas flow was limited by the N_2 flow rate. Both calibration curves were used later on to calculate the partial flow of each gas.

Since mixed ionic and electronic conductors release or incorporate oxygen following a pO_2 switch in the surrounding atmosphere, it is important to supply an adequate amount of oxygen in the carrier gas stream to ensure that the oxygen partial pressure step is well defined and not manipulated by the oyxgen flux of the measured sample [75, 76] . Therefore experiments employing different flow rates were carried out. Figure 3.6 presents extracts of three measurements that were done on a STO single crystal at the same furnace temperature setpoint of 660 °C. A flow rate of 0.516 ml/s was the lowest and a flow rate of 2.75 ml/s the highest achievable rate. The calculated electrical conductivity is plotted against the experimental duration. Figure 3.6a shows how the conductivity changes upon an applied pO_2 switch between 0.2 bar and 0.15 bar, Figure 3.6b presents the same experiments but between oxygen partial pressures of 0.15 bar and 0.10 bar.

It is clear that the change in conductivity depends on the applied gas flow. With higher flow rates the transient response becomes more pronounced and approaches the shape of an ideal step, which is preferably and also an indicator that the oxygen supply in the gas flow

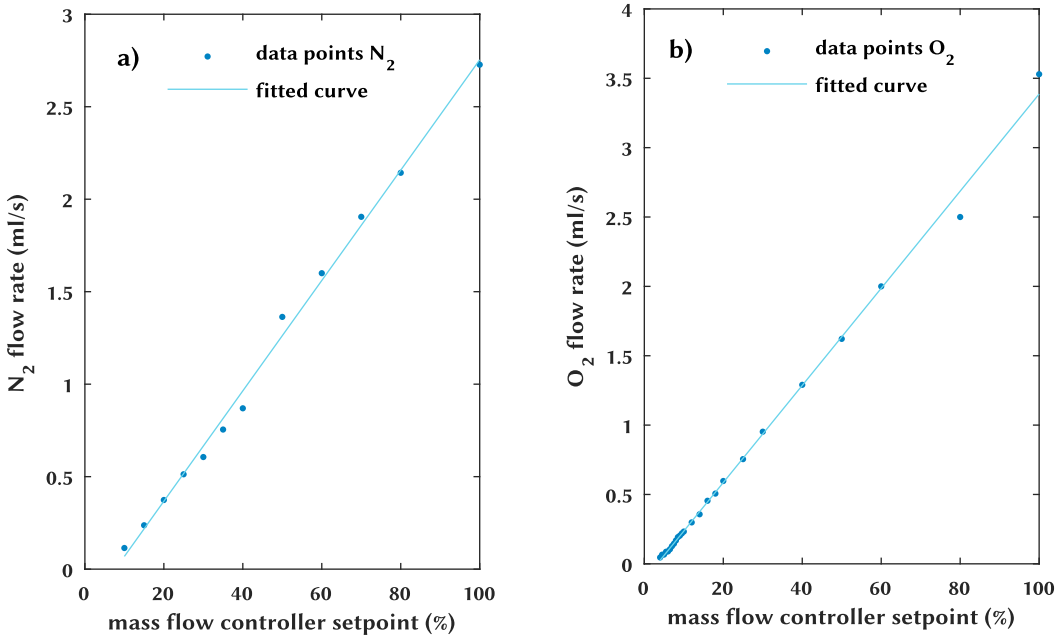

Figure 3.5.: N_2 and O_2 flow rate dependence of the mass flow controller setpoint. **a)** N_2 calibration curve: y = 0.0298 · x - 0.2294 **b)** O_2 calibration curve: y = 0.035 · x - 0.1142

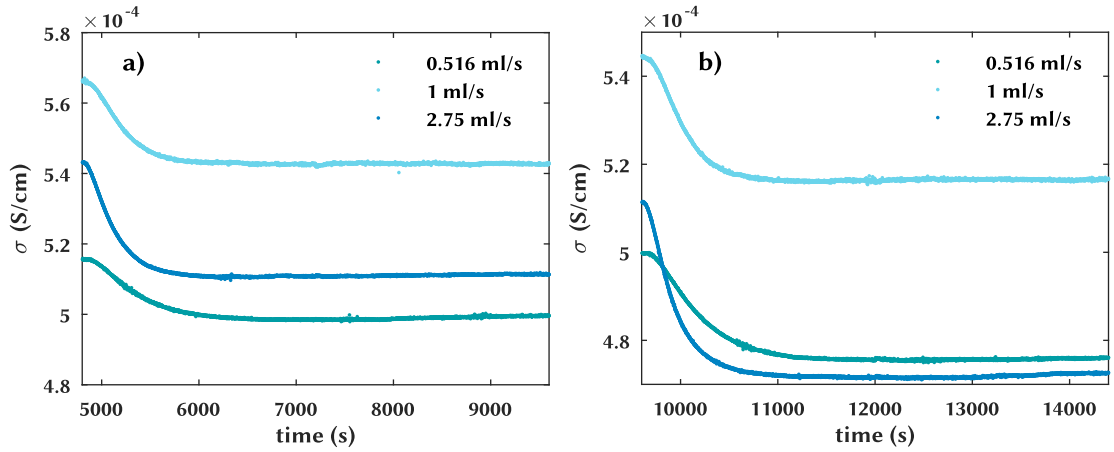

Figure 3.6.: Extracts of three measurements of STO employing different gas flows: 0.516 ml/s, 1 ml/s, 2.75 ml/s at 636 °C, 634 °C and 637 °C, respectively. **a)** A pO_2 switch between 0.2 bar and 0.15 bar was applied. **b)** A pO_2 switch between 0.15 bar and 0.10 bar was applied.

rate is sufficient. However, an ideal step response cannot be achieved as the volume of the reactor has to be flushed, which also has an impact on the shape of the transient response [63]. The measured average temperatures during the experiments differed slightly from each other and were 634 °C, 636 °C and 637 °C. Nonetheless, this fact should not contradict the conclusion drawn above. Hence, all experiments were carried out with a total gas flow rate of 2.75 ml/s.

3.4. Data analysis

3.4.1. Relaxation profiles

a) Equilibrium conductivity

Besides kinetic data, the value of the equilibrium conductivity at a certain oxygen partial pressure in the surrounding atmosphere can be derived from the measured data. The evaluation of the equilibrium conductivity was the same for all samples. Generally, the conductivity σ can easily be calculated from the measured data since it is the reciprocal value of the resistivity ρ (Equation (2.63), section 2.4):

$$\sigma = \frac{1}{\rho} \tag{3.1}$$

Figure 3.7 gives as an example for a typical course of a conductivity relaxation experiment. The calculated conductivity is plotted against the experimental duration t. Each step is linked to the stepwise change of the oxygen partial pressure.

The single pO_2 steps that were applied in all experiments are given below:

$$0.2\,\text{bar} \rightleftharpoons 0.15\,\text{bar} \rightleftharpoons 0.10\,\text{bar} \rightleftharpoons 0.075\,\text{bar} \rightleftharpoons 0.05\,\text{bar} \rightleftharpoons 0.035\,\text{bar} \rightleftharpoons 0.025\,\text{bar} \rightleftharpoons 0.015\,\text{bar}$$

The value of the equilibrium conductivity was obtained by taking the mean of the last 10 % of the measured data of each step. However, this was only done if the sample had reached a new equilibrium state with the surrounding atmosphere in the chosen experimental duration. In Figure 3.7 a step is shown where the O_2 was cut from the gas flow rate and the reactor was flushed with pure N_2. When the next pO_2 switch was applied the conductivity of the sample was still decreasing. In this case the chosen duration was too short and a constant value of σ couldn't be reached. Therefore this step wasn't evaluated.

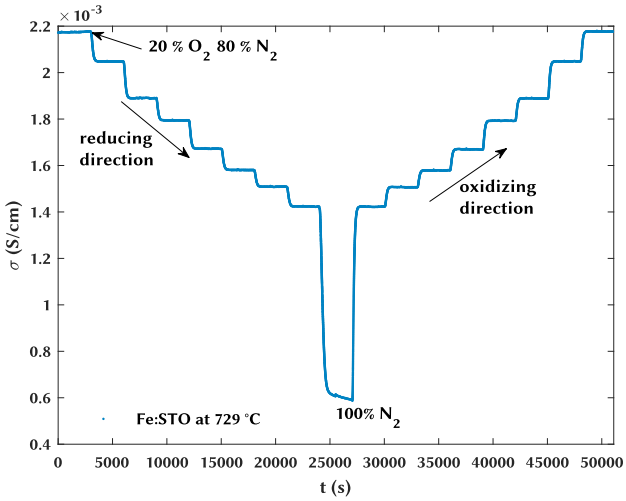

Figure 3.7.: Conductivity relaxation experiment carried out on a Fe:STO single crystal at 729 °C. The pO_2 switches are carried out stepwise both in reducing and oxidizing direction, starting in this instance at 0.2 bar.

b) Determination of kinetic parameters

Figure 3.8a presents a detail of the step profile shown above. A pO_2 switch between 0.10 bar and 0.15 bar in both reducing and oxidizing direction is shown. Figure 3.8b shows each calculated normalized conductivity σ_{norm} of these two oxygen partial pressure steps plotted against the experimental duration. Normalized relaxation profiles are used to obtain the kinetic parameters D_{chem} and k_{chem}.

The kinetic parameters are derived by fitting a solution of Fick's 2nd law to the normalized relaxation profile as already explained before (see subsection 2.2.2) However, Equation (2.33) only holds if the oxygen partial pressure change inside the reactor occurs instantly after the pO_2 switch has been applied to the system. Since the volume of the reactor used throughout the experiments didn't allow for instantaneous pO_2 steps a modified version of Equation (2.33) had to be employed. Equation (3.2) was derived by Otter et al. [63] and takes the reactor flush time τ_f into account. The reactor was modeled as a continuous ideally stirred tank reactor, assuming perfect mixing inside the reactor [63].

$$\frac{\sigma(t)-\sigma_0}{\sigma_\infty-\sigma_0} = 1 - exp\left(-\frac{t}{\tau_f}\right) - \sum_{n=1}^{\infty} \frac{2L^2}{\alpha_n^2(\alpha_n^2+L^2+L)} \cdot \frac{\tau_n}{\tau_n-\tau_f} \cdot \left[exp\left(-\frac{t}{\tau_n}\right) - exp\left(-\frac{t}{\tau_f}\right)\right] \quad (3.2)$$

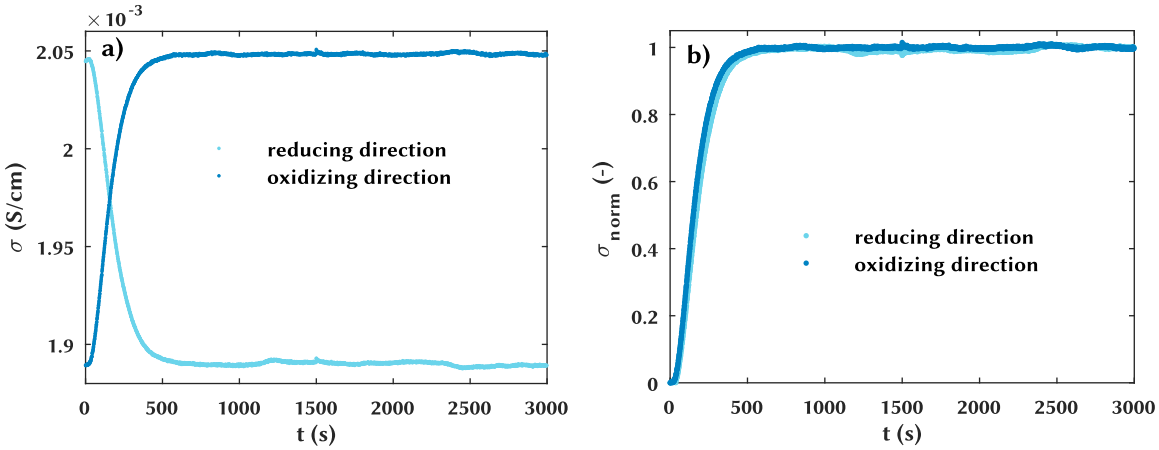

Figure 3.8.: Measurement of a Fe:STO single crystal at 729 °C. **a)** σ plotted against t. pO_2 switch in reducing and oxidizing direction: 0.15 bar → 0.10 bar, 0.10 bar → 0.15 bar. **b)** σ_{norm} plotted against the experimental duration.

with

$$\tau_n = \frac{a^2}{\alpha_n^2 D_{chem}} \tag{3.3}$$

Otter et al. showed that if τ_f has an impact on the relaxation process, the relaxation profile will shift to the right, thereby changing the shape of the profile [63]. If the flush time correction is then ignored in the fitting procedure large errors are introduced into the obtained kinetic parameters [63]. Hence, Equation (3.2) was used as a basis for the fitting procedure which will be explained in the following subsection 3.4.2. If not mentioned otherwise, σ_0 is the first value of σ after the oxygen partial pressure is switched. σ_∞ is again the average of the last 10 % of the now constant transient response.

3.4.2. Fitting procedure

a) Developing a fitting routine

The fitting process was carried out in MATLAB (9.5 (R2018b), The MathWorks, Inc., USA) using the curve fitting function *lsqcurvefit*, which uses a non linear least squares solver to solve a given problem. It requires a non linear model function, which includes the coefficients that are of interest. Additionally, a set of x,y-data is required and an initial point has to be defined at which the solver begins the minimization of the problem.

Equation (3.2) served as the model function and in a first attempt to fit the data D_{chem} was substituted using:

$$D_{chem} = \frac{ak_{chem}}{L} \tag{3.4}$$

This was done to constrain the fit and left τ_f and k_{chem} as coefficients in the fitting process. The value of L was guessed and the roots of the transcendental equation (Equation (2.26), subsection 2.2.2) were calculated based on that guess using a method proposed by Otter, Haar, and Bouwmeester [66]. Figure 3.9 shows a normalized relaxation profile of a Fe:STO single crystal at 729 °C, the oxygen partial pressure is switched between 0.15 bar and 0.10 bar. In a first approach to test the fitting routine, three different values of L were guessed in order to fit the relaxation profile and find τ_f and k_{chem}.

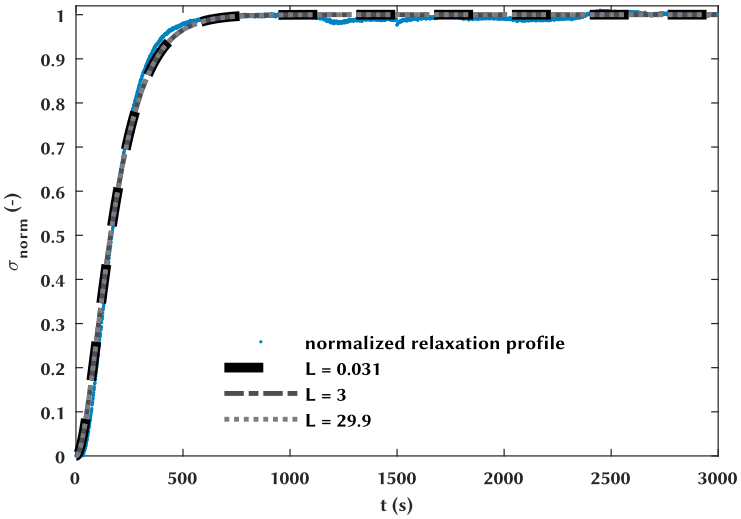

Figure 3.9.: Fe:STO single crystal at 729 °C, normalized relaxation profile at a pO_2 switch between 0.15 bar → 0.10 bar. Three different input values for L were guessed: 0.031, 3 and 29.9.

The plotted fits in Figure 3.9 seem to fit the relaxation profile equally well even though their input values of L differ considerably from each another. This suggests that the fit only relies on the guess of the starting values and seems to be independent of the input value of L. The evaluation of D_{chem} and k_{chem} from relaxation profiles, however, strongly depends on the value of L. According to Otter et al. both parameters can be obtained simultaneously if L is included in the interval $0.03 < L < 30$ [63]. For L values < 0.03 the relaxation process is controlled by the surface reaction and only k_{chem} can be derived from the relaxation profile. For L values > 30 the process is limited by the diffusion within the bulk of the material and thus, only

D_{chem} can be evaluated [63]. The example in Figure 3.9 shows that in employing this fitting method a determination, if a guessed value of L describes the relaxation process, as well as the evaluation of the kinetic parameters itself, become impossible. That is, even though all input values of L were included in the interval mentioned above, the "actual" value of L is not known at the beginning of an experiment and as a consequence an erroneous analysis of the kinetic parameters cannot be ruled out.

To overcome the shortcomings of this fitting approach, a literature search was conducted and an approach by Gopal and Haile was adapted [34]. They made use of the transcendental equation (Equation (2.26), subsection 2.2.2) and replaced L by it, thereby avoiding the need to guess the L value in the beginning of the fitting procedure. Instead α_1 and D_{chem} become independent fitting parameters [34]. Once α_1 is identified, the value of L and the remaining α_n can be calculated. The fitting process is simplified by this fitting approach as the value of α_1 can only take values between 0 and 1.5708 for $0 < L < \infty$. (see Table 3.5)

Table 3.5.: Calculated roots of the transcendental equation $L = \alpha_n \cdot tan(\alpha_n)$ for different values of L.

L	α_1	α_2	α_3	α_4	α_5	α_6	α_7	α_8
0	0	3.1416	6.2832	9.4248	12.5664	15.7080	18.8496	21.9911
0.03	0.1723	3.1511	6.2880	9.4280	12.5688	15.7099	18.8511	21.9925
30	1.5202	4.5615	7.6057	10.6543	13.7085	16.7691	19.8361	22.9098
∞	1.5708	4.7124	7.854	10.9956	14.1372	17.2788	20.4204	23.5619

Equation (3.5) shows the adapted version of Equation (3.2) where L was replaced by the transcendental equation as proposed by Gopal and Haile. The fitting parameters are: α_1, D_{chem} and τ_f. The reason for τ_f being a fitting parameter is the absence of an oxygen sensor in the measurement setup and therefore the lack of knowledge about the flush time behavior of the reactor.

$$\frac{\sigma(t)-\sigma_0}{\sigma_\infty-\sigma_0} = 1 - exp\left(-\frac{t}{\tau_f}\right) - \sum_{n=1}^{\infty} \frac{2\cdot tan^2(\alpha_n)}{\left(\alpha_n^2 + \alpha_n^2 tan^2(\alpha_n) + \alpha_n tan(\alpha_n)\right)} \cdot \frac{\tau_n}{\tau_n - \tau_f} \cdot \left[exp\left(-\frac{t}{\tau_n}\right) - exp\left(-\frac{t}{\tau_f}\right)\right] \quad (3.5)$$

One might notice that Gopal and Haile used a different interval within which D_{chem} and k_{chem} could be derived simultaneously. However, for the purpose of this work the fitting procedure was carried out using the boundaries of L mentioned earlier.

b) Two-parameter fit: D_{chem} , k_{chem}

This and the following paragraph contain information about the fitting process used to extract the kinetic parameters from experiments on Fe:STO and STO single crystals. The fitting procedure for the LSC thin films will be explained after that.

First every relaxation profile was fitted with a two-parameter fit using Equation (3.2). As already mentioned α_1, D_{chem} and τ_f were fitting parameters, which required an initial guess. α_1 and τ_f were varied between 0.001-1.5 and 30 s - 800 s, respectively. Estimated values of D_{chem} were obtained from Merkle and Maier [22]. For interpretation of the obtained solution, the solver gives, amongst other parameters, the value of a *first-order optimality* measure. Theoretically, the *first-order optimality* should be zero if the solver has reached a local minimum. The sum in Equation (3.2) was calculated using the first eight terms of the series.

The fitting procedure contained the following steps:

1. Fitting the relaxation profile with fixed initial values for α_1 and D_{chem} while switching the value for τ_f in a for-loop between 30 s and 800 s in steps of 5 s for each run.
2. Finding the smallest value of the *first-order optimality* among the 155 fitting runs.
3. Repeating 1.) and 2.) but changing the initial guess value of α_1 while switching τ_f again in the above mentioned for-loop. The value of D_{chem} stays unchanged throughout the fitting procedure. These steps are repeated until $\alpha_1 = 1.5$.
4. Calculating L from the fit which produced the smallest *first-order optimality* value.
5. Calculating k_{chem} using Equation (2.26) if $0.03 < L < 30$.

If the value of L was included in the interval between $0.03 < L < 30$, where it is assumed that both transport parameters can be derived from the relaxation profile, but L was close to the bounds of said interval, a single-parameter fit was performed in addition to the two-parameter fit in order to verify the obtained values from the two-parameter fit [34]. The single-parameter fit, which will be explained in the next paragraph, was also subsequently performed, if L wasn't included in the interval.

c) Single-parameter fit: k_{chem} or D_{chem}

The two-parameter fit will introduce errors in the obtained parameters, if the relaxation process is either dominated by surface reaction or diffusion of the mobile species within the material [34].

In case of $L < 0.03$ or L being near to this lower bound of the interval, a single-parameter fit was performed. The relaxation profile was fitted to Equation (3.6), which is a reduced version of Equation (3.2). In this instance the oxygen incorporation at the surface of the sample dominates the relaxation process and only the first term of the series is relevant as the higher terms converge to zero and can be neglected [34, 63, 77]. τ_f and k_{chem} are the fitting parameters.

$$\frac{\sigma(t)-\sigma_0}{\sigma_\infty-\sigma_0} = 1 - exp\left(-\frac{t}{\tau_f}\right) - \frac{\frac{a}{k_{chem}}}{\frac{a}{k_{chem}}-\tau_f} \cdot \left[exp\left(-\frac{k_{chem}t}{a}\right) - exp\left(-\frac{t}{\tau_f}\right)\right] \tag{3.6}$$

The single-parameter fit was approached in a similar manner as the two-parameter fit:

1. Fitting the relaxation to Equation (3.6). τ_f was, again, switched in a for-loop while k_{chem} had a fixed initial value.

2. Finding the smallest value of the *first-order optimality* among the 155 fitting runs.

3. Repeating 1.) and 2.) but changing the initial value of k_{chem} for the next fitting run. k_{chem} was varied over five orders of magnitude to ensure that the smallest value of the *first-order optimality* measure was picked out of a large enough data pool.

A diffusion limited relaxation profile wasn't encountered during all experiments but for the sake of completeness, the version of Equation (3.2) in case of the diffusion limited relaxation process is presented in Equation (3.7). The single parameter fit should be performed, if $L > 30$ or if the value of L is close to this upper bound. The fitting parameters for this procedure are τ_f and D_{chem}.

$$\frac{\sigma(t)-\sigma_0}{\sigma_\infty-\sigma_0} = 1 - exp\left(-\frac{t}{\tau_f}\right) - \frac{8}{\pi^2}\sum_{n=1}^{\infty}\frac{1}{(2n+1)^2}\cdot\frac{\tau_n}{\tau_n-\tau_f} \cdot \left[exp\left(-\frac{t}{\tau_n}\right) - exp\left(-\frac{t}{\tau_f}\right)\right] \tag{3.7}$$

with

$$\tau_n = \frac{4a^2}{D_{chem}\,(2n+1)^2\,\pi^2} \tag{3.8}$$

d) An adapted fitting procedure for the LSC thin films

The following two paragraphs contain information about the adapted fitting procedure for the relaxation profiles of the LSC thin films. It is described separately because the approach to the problem differs from the method described above. First of all, the determination of the value of L with the two-parameter fit, which was the first step in the fitting procedure for Fe:STO and STO, is abandoned. The relaxation process of the thin films is assumed to be controlled by the surface reaction as the film thickness d, which was in the range of nanometres for all deposited LSC thin films (Table 3.3), is considered much less than the characteristic length L_c (Equation (2.36), subsection 2.2.3). Hence, the relaxation profile is fitted directly with a single-parameter fit to obtain k_{chem}. Secondly, fitting relaxation profiles to Equation (3.6) resulted in questionable output values.

In a first attempt to fit a set of relaxation profiles from experiments conducted on LSC thin films, Equation (3.6) was used. Since the thin films are deposited on inert substrates [1], oxygen can only be incorporated and released from the top of the thin films. Accordingly, a had to be set equal to the film thickness d in Equation (3.6). Figure 3.10 shows a relaxation profile of a 40 nm LSC thin film at 386 °C, which was deposited on LAO. Even though the data is quite noisy, the fitted curve seems to qualitatively represent the relaxation profile. However, the output values are $\tau_f = 174$ s and $k_{chem} = 0.2752$ cm/s. The value for τ_f seems plausible when compared to the data whereas the obtained value for k_{chem} has to be doubted. Compared to data from Egger et al. [6], its assigned value is too high at this particular temperature. To ensure that the implausible output value for k_{chem} wasn't just a singularity for this specific relaxation profile, relaxation profiles from other pO_2 switches were fitted against Equation (3.6). The output values for k_{chem} were found to be too high in each instance. As a consequence Equation (3.6) wasn't used to fit the relaxation data of the LSC thin films.

The next attempt to fit the relaxation data of the LSC thin films involved Equation (3.9)

$$\frac{\sigma(t)-\sigma_0}{\sigma_\infty-\sigma_0} = 1 - exp\left(-\frac{t}{\tau_r}\right) - exp\left(-\frac{t}{\tau_f}\right) \tag{3.9}$$

[1] In this context inert is used to point out that the chosen substrates are insulators as well as inert to oxygen exchange in the considered temperature range and their contribution to the measured conductivity can be neglected.

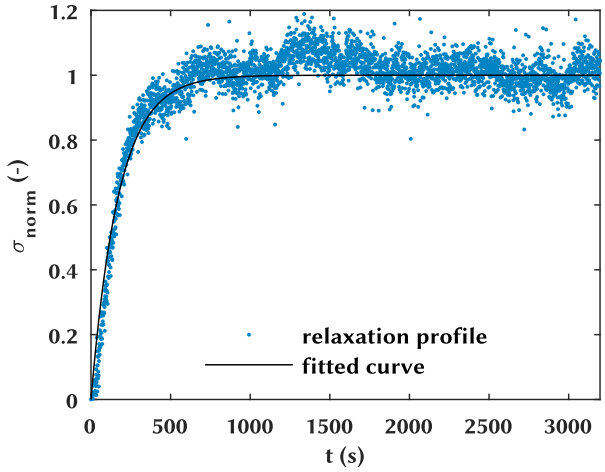

Figure 3.10.: 40 nm LSC|LAO at 386 °C, pO_2 switch in reducing direction form 0.2 bar → 0.15 bar. The relaxation profile was fitted to Equation (3.6). Output values for τ_f and k were 174 s and 0.2752 cm/s, respectively.

with

$$\tau_r = \frac{d}{k_{chem}}. \tag{3.10}$$

In Equation (3.9) the relaxation process is modeled with two exponential functions. τ_f denotes the reactor flush time, while τ_r denotes the specific relaxation time of the thin film. Since both τ_f and τ_r are fitting parameters, the value of k_{chem} can be calculated using Equation (3.10).

Figure 3.11 shows the same pO_2 step as in Figure 3.10, but the fitted curve was obtained by fitting the relaxation profile to Equation (3.9). The output values for τ_f and τ_r are 174 s and 0.002 s, respectively. τ_f matches the value from the fit shown above. The value of τ_r corresponds to $k_{chem} = 2 \cdot 10^{-3}$ cm/s, which is not convincing either since the k_{chem} value is still too high. Additionally, it was observed that the input value for τ_r equaled the output value. The input value of τ_r was therefore subsequently varied over several orders of magnitude and the same behavior was observed: τ_f was fitted independent of its input value and the input value of τ_r equaled its output value. This led to the conclusion that the fitting procedure was only sensitive to τ_f and Equation (3.9) couldn't be used to fit the relaxation profiles. Additionally, it raised the question if the flush time of the reactor was in fact the only parameter, apart from the equilibrium conductivity, that could be derived from the relaxation profiles at higher temperatures. To deduce if τ_r and τ_f could be derived from the relaxation profiles simultaneously,

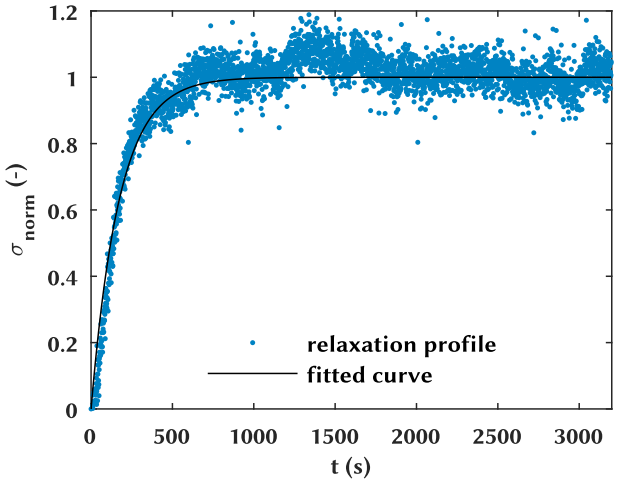

Figure 3.11.: 40 nm LSC|LAO at 386 °C, pO_2 switch in reducing direction from 0.2 bar → 0.15 bar. The relaxation profile was fitted to Equation (3.9). Output values for τ_f and τ_r were 174 s and 0.002 s, respectively.

τ_r had to be estimated and compared to the value of τ_f. Generally, τ_r offers information on how fast the surface reaction step will be at a certain temperature and the condition $\tau_f \ll \tau_r$ has to hold if kinetic parameters are to be derived from relaxation profiles [63].

In Figure 3.12, data points are shown that were extracted from the work of Egger et al. [6]. The decadic logarithm of the surface exchange coefficient is plotted against the inverse temperature. The data points were fitted with a linear function which was subsequently used to extrapolate values of k_{chem} at lower temperatures.

In order to calculate τ_r from the extrapolated k_{chem} values, the quantitative change in the oxygen vacancy concentration that follows a pO_2 switch has to be assessed. Throughout the experiment the charge neutrality of the material has to be fulfilled:

$$[Sr'_{La}] - 2[V^{\bullet\bullet}_{O}] - [h^{\bullet}] = 0 \tag{3.11}$$

The hole concentration of $La_{0.6}Sr_{0.4}CoO_{3-\delta}$ is assumed to be very close to 0.4 since the oxygen nonstoichiometry δ is small in the considered temperature range between 100 °C - 500 °C [53]. The change in conductivity following a pO_2 switch is therefore attributed to a change of the hole concentration, which again, as demanded by Equation (3.11), causes to change the concentration of oxygen vacancies.

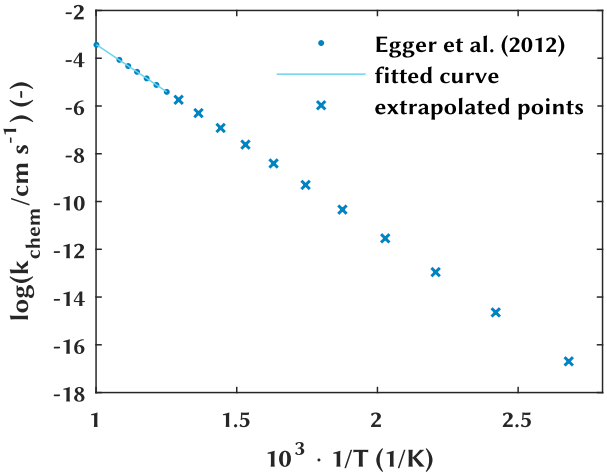

Figure 3.12.: Logarithm of the surface exchange coefficient dependent on the inverse temperature. Data points in the temperature range between 525 °C and 725 °C were taken from Egger et al. [6] and fitted with a linear function: $y = -7.9x + 4.478$. This function was then used to extrapolate points in the temperature range between 100 °C and 500 °C. Egger et al. derived the k_{chem} values at a pO_2 of 0.1 bar.

It was observed that the conductivity of the LSC thin films in the temperature range between 268 °C - 466 °C changed by approximately 0.1 % for each pO_2 switch independent of the thin film's substrate and direction in which the pO_2 was switched (see Appendix C). Thus, the change of the hole concentration after an oxygen partial pressure switch is applied, is estimated by

$$\Delta\sigma = \Delta[h^{\bullet}] \approx 0.001. \tag{3.12}$$

The relative change of the oxygen vacancy concentration is therefore

$$\Delta[V_O^{\bullet\bullet}] \approx \frac{0.4 \cdot 0.001}{2} \approx 2 \cdot 10^{-4}. \tag{3.13}$$

The change of the oxygen vacancy concentration has to be related to the LSC thin film. Since both examples referred to the same sample the following calculation will also be based on the 40 nm LSC|LAO thin film. Naturally, the estimation would be the same for any other LSC thin film with a different thickness. The volume V of a 40 nm thin film is

$$V = 1 \times 1 \times 0.000004 = 4 \cdot 10^{-6} cm^3. \tag{3.14}$$

The relative change in oxygen content for $La_{0.6}Sr_{0.4}CoO_{3-\delta}$ in the volume of a 40 nm thin film is therefore

$$\Delta V \approx 2 \cdot 10^{-4} \cdot 4 \cdot 10^{-6} \approx 8 \cdot 10^{-10} cm^3. \tag{3.15}$$

To calculate τ_r the relative change of the oxygen content in the volume of the thin film has to be related to the area A of the thin film. This gives the relative change of the oxygen content in the thickness of the thin film.

$$\Delta d \approx \frac{\Delta V}{A} \approx \frac{8 \cdot 10^{-10} cm^3}{1 cm^2} \approx 8 \cdot 10^{-10} cm \tag{3.16}$$

Finally, Δd can then be inserted into Equation (3.10) to calculate τ_r.

Table 3.6 presents the calculated values of τ_r for each extrapolated point in Figure 3.12. As k_{chem} increases with increasing temperature τ_r decreases, which means that the oxygen is incorporated or released faster with increasing temperature. In the examples shown above the output value of τ_f was 174 s at 386 °C. Comparing this value to the extrapolated value of τ_r at 380 °C it becomes clear that $\tau_f \gg \tau_r$.

Table 3.6.: Overview over the extrapolated values of k_{chem} that were calculated using $y = -7.9 \cdot x + 4.478$. Additionally, calculated values of τ_r for a 40 nm LSC thin film are shown. Above 220 °C the output value of $\tau_f \gg \tau_r$.

T (°C)	T (K)	$10^3 \cdot \frac{1}{T}$ (1/K)	$\log\left(\frac{k_{chem}}{cm \cdot s^{-1}}\right)$ (-)	k_{chem} (cm/s)	τ_r (s)
100	375.15	2.6656	-16.5800	$2.6300 \cdot 10^{-17}$	30418189
140	415.15	2.4088	-14.5511	$2.8115 \cdot 10^{-15}$	284549
180	455.15	2.1971	-12.8787	$1.3222 \cdot 10^{-13}$	6050.70
220	495.15	2.0196	-11.4766	$3.3376 \cdot 10^{-12}$	239.69
260	535.15	1.8686	-10.2840	$5.1998 \cdot 10^{-11}$	15.39
300	575.15	1.7387	-9.2573	$5.5291 \cdot 10^{-10}$	1.4469
340	615.15	1.6256	-8.3642	$4.3232 \cdot 10^{-9}$	0.1850
380	655.15	1.5264	-7.5801	$2.6296 \cdot 10^{-8}$	0.0304
420	695.15	1.4385	-6.8863	$1.2994 \cdot 10^{-7}$	0.0062
460	735.15	1.3603	-6.2679	$5.3963 \cdot 10^{-7}$	0.0015
500	775.15	1.2901	-5.7134	$1.9347 \cdot 10^{-6}$	0.0004

τ_f exceeding τ_r poses a problem for the evaluation of the data since kinetic parameters can only be derived from relaxation profiles if $\tau_f \ll \tau_r$ [63]. If the flush time of the reactor is greater than or in the range of the specific relaxation time the sample acts as an oxygen sensor and consequently, only τ_f can be evaluated [63].

Based on the results of this estimation two conclusions could be drawn:

1. τ_f is the only parameter that can be derived from relaxation profiles in the temperature range between 268 °C and 466 °C because τ_f superposes the specific relaxation time of the LSC thin films at temperatures above 200 °C.

2. Using the measurement setup described in subsection 3.3.1 to acquire information on the thin films' τ_r, requires that the experiments were to be done at temperatures around and below 200 °C.

The relaxation profiles, that were measured at temperatures between 268 °C and 466 °C, were therefore fitted to Equation (3.17). Instead of *lsqcurvefit* the MATLAB curve fitting tool was used in the fitting procedure. τ_f was the fitting parameter.

$$\frac{\sigma(t) - \sigma_0}{\sigma_\infty - \sigma_0} = 1 - exp\left(-\frac{t}{\tau_f}\right) \tag{3.17}$$

Additionally, conductivity relaxation experiments were conducted on three LSC thin films, 10 nm LSC|LAO, 10 nm LSC|STO, 20 nm LSC|MgO, at 144 °C, 143 °C - 204 °C and 144 °C, respectively. The relaxation data from these experiments showed a drift, which had to be removed from the data in order to fit it. Equation (3.18) was used to fit the drift corrected relaxation profiles. τ was the fitting parameter. The drift as well as the data analysis will be described in detail in the following section 3.5.

$$\frac{\sigma(t) - \sigma_0}{\sigma_\infty - \sigma_0} = 1 - exp\left(-\frac{t}{\tau}\right) \tag{3.18}$$

with

$$\tau = \tau_r + \tau_f \tag{3.19}$$

e) General remarks on the fitting procedure

In the following paragraph a few observations that were made during the process of evaluating the data will be addressed.

The *first-order optimality* measure is used as a parameter to objectively assess if a minimum is found. In theory, the solver should converge to one solution where the global minimum is reached and the *first-order optimality* measure is therefore zero. Practically, however, there are several local minima. That is, the *first-order optimality* has to be zero at a minimum but in return, if the *first-order optimality* is zero, it doesn't necessarily follow that the output parameters are found at the global minimum. This means that there is the possibility of introducing errors in the obtained parameters by deciding for or against a output value based on the *first-order optimality*. So far these errors have not been quantified or estimated but it should be considered for following experiments.

The solver needs initial values that are sufficiently close to the "real" values. This prevents that the solver converges to a false minimum. Moreover, the fitting parameters should be constrained to avoid that the nonlinear least squares solver presents output values, that mathematically solve the problem, but otherwise are physically implausible. Namely, in this work α_1 and τ_f should have been constrained.

In addition, τ_f being a fitting parameter produced challenges throughout the fitting procedure. Firstly, τ_f tends to be the dominating parameter in the exponential function as it exceeds the other parameters in several orders of magnitude [78]. The fitting process is therefore controlled by the flush time. Furthermore, small changes in τ_f will have a rather strong impact on the other fitting parameters. Secondly, fitting results exhibiting equally low *first-order optimality* measures in addition to visually good agreement of measured data and fitted curve, but different τ_f values could not be distinguished since the flush time could not be quantified precisely. Thus, measuring the flush time during an experiment would benefit the evaluation of the kinetic parameters tremendously as this would allow for treating τ_f as a fixed parameter in the fitting process.

3.5. Drift in measured data

A drift in the measured data was observed for the experiments that were conducted on the LSC thin films. The other materials didn't exhibit this behavior. This section will show how drifting relaxation data looks like, under which experimental conditions the drift occurs and if it is possible to circumvent it. Finally, the data analysis of the drifting data will be discussed.

If the oxygen partial pressure in the surrounding atmosphere is changed, the electrical conductivity of the sample will relax to a new equilibrium value. Switching the oxygen partial pressure again in the reversed direction should result in the starting value of σ. In case of the LSC thin films the equilibrium conductivity for each oxygen partial pressure shifts over the span of the experiment, meaning that the values of σ from pO_2 switches in reducing and oxidizing direction do not match. In this work this behavior will be referred to as drifting data.

a) Experimental conditions

Figure 3.13 presents two examples of drifting relaxation data. Both experiments were conducted on the same sample, a 10 nm LSC thin film. Figure 3.13a) shows a measurement that was done at 146 °C. The electrical conductivity is shifting towards lower values over the span of the experiment and the slope of the drift is less steep for pO_2 steps in oxidizing direction. The measurement, that is presented in Figure 3.13b), was done at 430 °C. The slope of the drift is positive in this case, causing the conductivity to shift to higher values. However, it is evident that in this case the drift in the data is much less pronounced compared to the measurement that was done at 146 °C. This behavior was observed for all LSC thin films: the drift was more pronounced if the experiment was conducted below or around 200 °C and became less pronounced at elevated temperatures above 300 °C.

In addition to the drift that superposes the entire measurement, Figure 3.13b) shows that the value of the conductivity is also drifting when the oxygen partial pressure is kept at a constant value before the next pO_2 step is applied. This behavior could be avoided in some cases by switching the polarization of the applied voltage more than once.

It was already pointed out that the slope of the drift in Figure 3.13a) is negative and becomes less steep when the oxygen partial pressure is switched in oxidizing direction. This led to the assumption that the drift might occur because oxygen was being released and incorporated from and into the material with two different surface reaction rates. It was suspected that

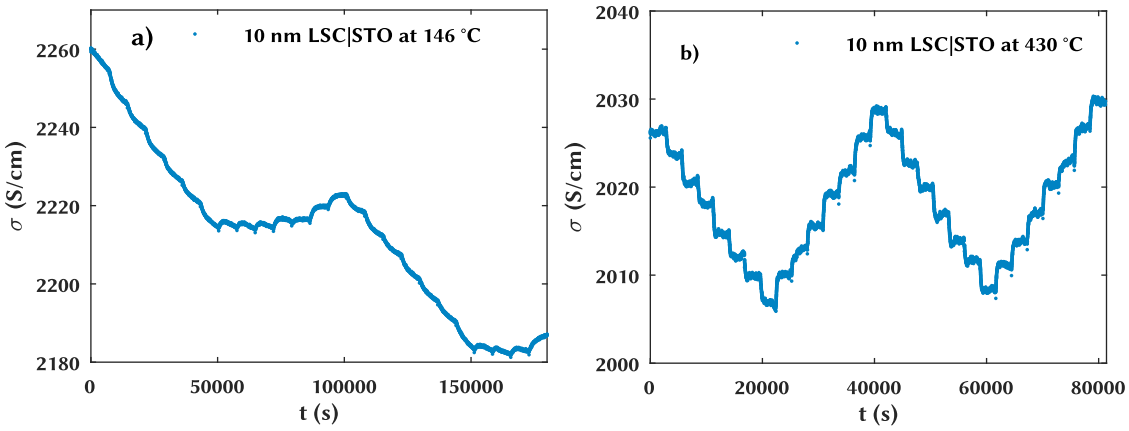

Figure 3.13.: 10 nm LSC|STO thin film measured at different temperatures. **a)** 146 °C, pronounced drift in the data visible. **b)** 430 °C, drift less pronounced compared to measurement at 146 °C, but an overall trend is still visible.

the porosity of the Pt contacts wasn't sufficient enough, which would lead to a slower oxygen incorporation and release at and under the Pt contacts compared to the unpainted surface of the thin film. Furthermore, the gradual direction change of the slope was assumed to stem from accelerated oxygen incorporation at and under the Pt contacts when the oxygen partial pressure was changed in oxidizing direction.

To test if the Pt contacts were linked to the drift, the experiment was repeated at 143 °C and the Pt contacts were removed using an ultrasonic bath. If the Pt contacts were the origin of the drift, the drift should vanish. The Pt tips were brushed with Pt paste before contacting the sample to ensure a sufficient electrical contact.

Figure 3.14 shows the result of this measurement. The drift is still visible and the relaxation data are therefore not consistent with the aforementioned hypothesis. But in contrast to the measurement, that was done at 146 °C, the drift now had an overall positive slope. If this behavior is linked to the absence of the Pt contacts couldn't be determined as this was the only measurement which was conducted without Pt contacts. The range of the conductivity values is a little lower compared to the previous measurement, which could be associated with the absence of the Pt contacts.

Thus, the origin of the drift in the relaxation data is still unknown and it was not possible to circumvent it in this work. The examples in Figure 3.13 and Figure 3.14 also showed that the drift may have either a positive or a negative slope.

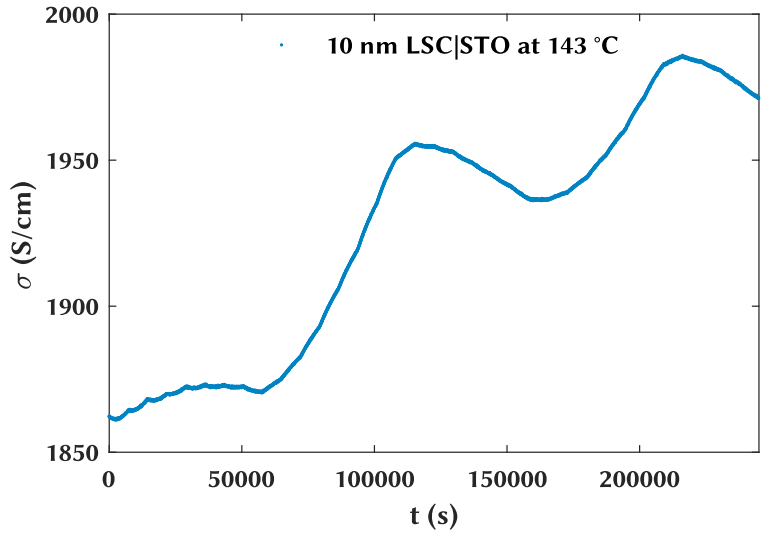

Figure 3.14.: The same 10 nm LSC|STO thin film as in Figure 3.13a), measured at 143 °C without Pt contacts. Now, a positive drift was observed.

This drift-phenomenon is particularly interesting, as the defect chemical cause is unknown. Cationic defects can be ruled out to play a role at these low temperatures, whereas the chemical exchange and diffusion is already responsible for the observed signal and has a much faster time constant than the drift. One possibility might be - yet unknown - phase instabilities of LSC at these low temperatures.

b) Data analysis

Even though the origin of the drift has not been determined so far, the data from the measurements of the LSC thin films at 144 °C-146 °C, 194 °C and 204 °C were used to estimate the chemical surface exchange coefficient k_{chem}. As mentioned in subsection 3.4.2 Equation (3.18) was used to fit the relaxation data that were obtained from these experiments. However, the data had to be corrected by subtracting the drift before the relaxation profiles could be fitted to Equation (3.18).

The last third of each transient response was taken and fitted to a linear function. The slope of this function was used to correct the drifting data. Instead of using the continuous experimental time, each corrected profile was calculated using the given experimental duration between two

oxygen partial pressure switches. By employing this approach it is assumed that the sample reaches an equilibrium state with the surrounding atmosphere in the given duration before the next pO_2 switch is applied. Figure 3.15 shows the resulting data.

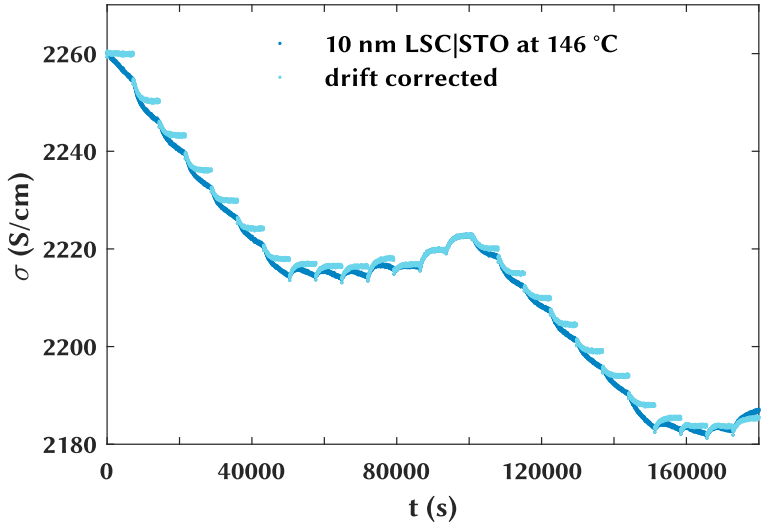

Figure 3.15.: 10 nm LSC|STO thin film measured at 146 °C. The relaxation data were corrected by subtracting the drift in order to estimate k_{chem} from this experiment. Original data are shown in dark blue, corrected data in light blue.

It is clear that absolute values of the electrical conductivity and therefore the equilibrium conductivity for each pO_2 step cannot be evaluated since the drift is superimposed on the whole measurement. The relative change in conductivity, however, can be used to estimate the change in oxygen content in the film thickness.

In Figure 3.16b) the normalized conductivity of a pO_2 step in reducing direction between 0.10 bar and 0.075 bar is presented. This profile was calculated using the drift corrected transient response shown in Figure 3.16a). The drift corrected normalized conductivity can be fitted to Equation (3.18) in order to obtain τ.

Calculating τ_r from Equation (3.19) requires τ_f. The flush time was averaged from the fitting results of all relaxation experiments that were done on the LSC thin films at a furnace set temperature of 500 °C and amounted to 189 s. τ_f was taken from these experiments as the temperature was high enough to ensure that the specific relaxation time was short compared to the flush time and the output value of the fitting procedure therefore was the flush time. The detailed derivation can be found in subsection 4.4.1.

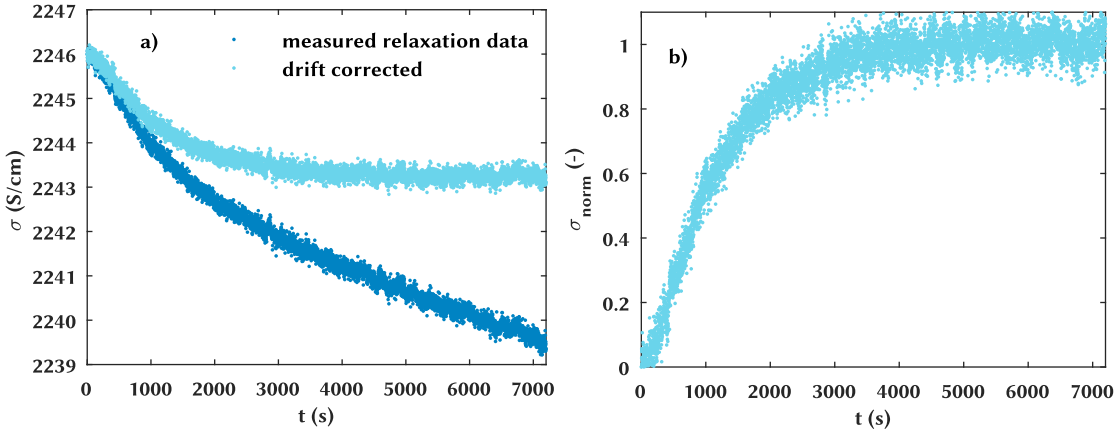

Figure 3.16.: 10 nm LSC|STO thin film measured at 146 °C. **a)** Measured and drift corrected transient response of a pO_2 switch between 0.10 bar and 0.075 bar. **b)** Normalized relaxation profile, which was calculated using the drift corrected transient response shown in Figure 3.16a).

To estimate k_{chem}, the relative change in oxygen content in the thin film, that follows an oxygen partial pressure switch, has to be assessed as well. The estimation of the relative change in oxygen content is basically the same estimation, which was already shown to calculate τ_r from extrapolated k_{chem} values (see subsection 3.4.2). The only difference is that the relative change in conductivity has to be calculated for each pO_2 step as its value changes for each pO_2 switch:

$$\Delta\sigma \approx \Delta[h^{\bullet}] \approx \left|1 - \frac{\sigma_{\infty}}{\sigma_0}\right|. \tag{3.20}$$

σ_0 denotes the initial conductivity, which is calculated by averaging the first ten points of the drift corrected transient response. σ_{∞} denotes the final value of the conductivity to which the sample relaxes in the given duration. It is calculated by averaging the last ten percent of the drift corrected data. The subsequent steps to calculate the relative change in oxygen content in the thin film thickness Δd are the same as in subsection 3.4.2.

Finally, k_{chem} is calculated using Equation (3.10).

4. Results and discussion

4.1. Material characterization

4.1.1. X-ray diffraction

$\theta-2\theta$ scans were carried out for a LSC|LAO and a LSC|STO thin film to investigate the structural composition of the deposited thin films. In addition, reciprocal space maps of these thin films were measured to check if the thin films were strained by the used substrates.

The obtained diffractograms from $\theta-2\theta$ scans are presented in Figure 4.1. The intensity plotted on the y-axis represents the square root of the registered counts. Identification of the single peaks was achieved by comparing the measured pattern to a XRD database. The majority of the peaks could be assigned to (100) diffraction peaks of LSC and the used substrates. In addition, the (111) diffraction peak of the silicium sample holder is visible in both diffractograms. At $2\theta \approx 95\,^{\circ}$ an additional diffraction peak is observed in each diffractogram. This peak and the small peak next to the (003) diffraction peak of the STO substrate in Figure 4.1a could not be assigned.

Figure 4.2a shows the measured reciprocal space map for a LSC|STO thin film. The (103) reflex of the LSC thin film is vertically aligned to the (103) reflex of the substrate, indicating that the LSC thin film is strained by the STO substrate. In case of the reciprocal space map shown in Figure 4.2b, which was measured for a LSC|LAO thin film, the vertical alignment between the (103) reflexes of the thin film and the substrate is also visible. The measured (103) reflex of this LSC thin film, however, is slightly more diffuse compared to the LSC|STO thin film. One possible explanation might be that the introduced strain relaxes partially within the film thickness.

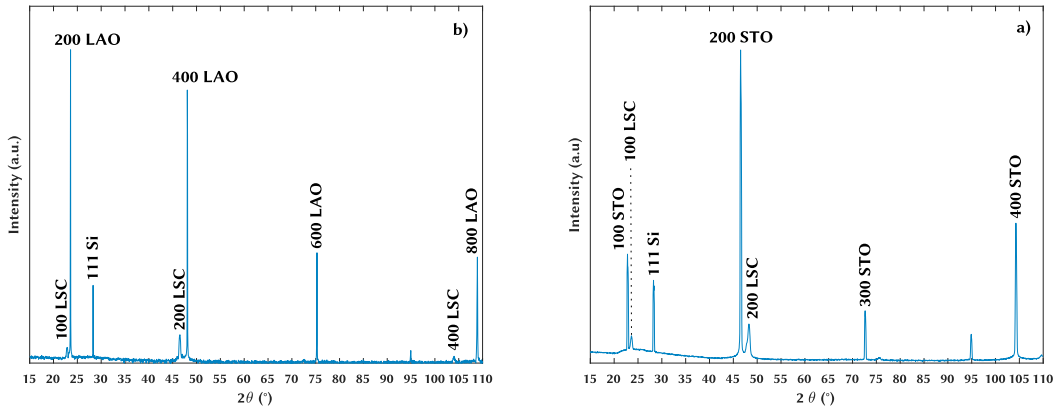

Figure 4.1.: $\theta - 2\theta$ scans of a) LSC deposited on STO, b) LSC deposited on LAO. The intensity is plotted in a square root scale. Both diffractograms show the (111) diffraction peak of the silicium sample holder and a diffraction peak at a 2θ position of approximately 95 ° which could not be assigned. Apart from that the diffractograms show only (100) diffraction peaks of LSC and the corresponding substrate.

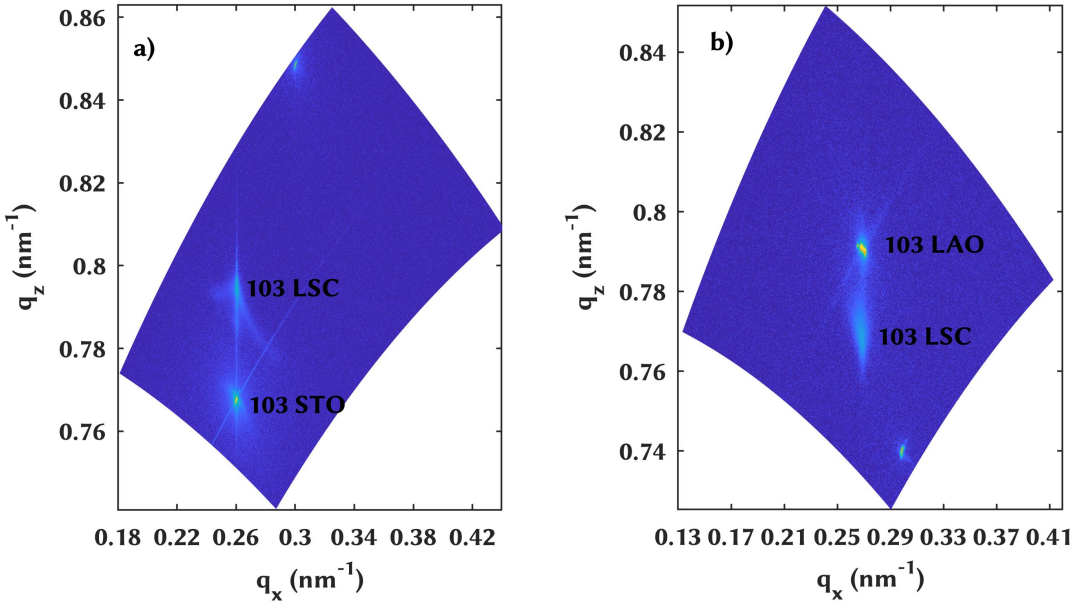

Figure 4.2.: Measured reciprocal space map for a LSC thin, which was deposited a) on STO and b) on LAO. The (103) reflex of the LSC thin film is aligned in vertical direction to the corresponding substrate in each shown instance.

4.1.2. Film thickness

The film thickness, d, of two LSC thin films was examined by profilometry (see subsection 3.2.2) to check if a desired film thickness could be achieved using the deposition parameters stated in subsection 3.1.3. The thin films, that were shown in Figure 3.2a and Figure 3.2b, are referred to as 'film 1' and 'film 2' in the following description.

'Film 1' was chosen since conductivity relaxation experiments, that were carried out on this thin film, revealed conspicuous conductivity values. It was anticipated that the thin film was slightly thicker than originally assumed. Film 1 was also deposited at an earlier point in time with a different LSC target and under slightly different deposition conditions compared to all other thin films, that were investigated in this work. 'Film 2' was measured as a substitute for these other thin films. The desired film thickness of each thin film was 20 nm.

Table 4.1.: Results from profilometry measurements on two thin films. The denotations 'film 1' and 'film 2' correspond to the thin films shown in Figure 3.2a and Figure 3.2b, respectively. The step height ($\widehat{=}$ film thickness) was measured repeatedly and subsequently averaged for each thin film.

	d(nm), film 1	**d(nm), film 2**
1.	30	19
2.	29	15
3.	26	25
4.	26	15
5.	27	25
6.	28	20
7.	28	28
8.	-	24
mean	≈ 28	≈ 21

Table 4.1 presents the results that were obtained by profilometry measurements. The step height was measured several times for both thin films. It is evident that the scatter in the obtained values of the film thickness is less pronounced for film 1 suggesting a fairly homogeneous film thickness. The observed scatter of the d values for film 2, however, is not surprising as the deposited film was of poor quality (see Figure 3.2b).

Averaging the obtained d values yields mean values of 28 nm for film 1 and 21 nm for film 2. All subsequent calculations for film 1 were carried out with the calculated mean value as the above mentioned presumption was verified. In case of film 2 the obtained average d value is

relatively close to the desired value of 20 nm, even though the d values varied more. Clearly, this does not proof beyond a doubt that the film thickness of the thin films, that were deposited with the same target as well as under the same conditions as film 2, equals in fact the desired film thickness. Nevertheless, subsequent calculations for the remaining thin films were carried out on this assumption.

It was already mentioned that the film thickness is the essential variable in the van der Pauw method. In order to eliminate arguable d values, it might be worth considering for future experiments either to prepare each film as film 1 (after the experiments are completed and even though the sample can't be reused for measurements) or to deposit a reference film which can be used to determine the film thickness instead.

4.2. STO and Fe:STO single crystals

4.2.1. Equilibrium conductivity

In the following section the oxygen partial pressure dependence as well as the temperature dependence of the equilibrium conductivity for both the STO and Fe:STO single crystal will be discussed. The equilibrium conductivity was obtained as described in subsection 3.4.1.

a) STO

Figure 4.3 shows the raw data of each conductivity relaxation experiment that was carried out on the STO single crystal.

At the beginning of the experiments shown in Figure 4.3a,g the temperature was still increasing which caused the observed increase in conductivity. The decrease in conductivity in Figure 4.3b is also caused by a non constant temperature, but the temperature was declining in this instance.

The oxygen was cut from the gas stream in the experiments which are shown in Figure 4.3c-e,g. As a result the conductivity drops significantly. It was already mentioned in subsection 3.4.1 that these steps weren't evaluated since no equilibrium state could be established with the surrounding atmosphere in the given aquisistion time. The pO_2 steps of the experiment that was carried out at 578 °C weren't evaluated for the same reason.

The second experiment that was carried out at 767 °C is plotted in two separate figures (see Figure 4.3g,h) since the calculated σ values were highly scattered throughout the 17th and 18th oxygen partial pressure step. These steps are therefore not presented. The STO single crystal was probably poorly contacted during this experiment, which caused this behavior.

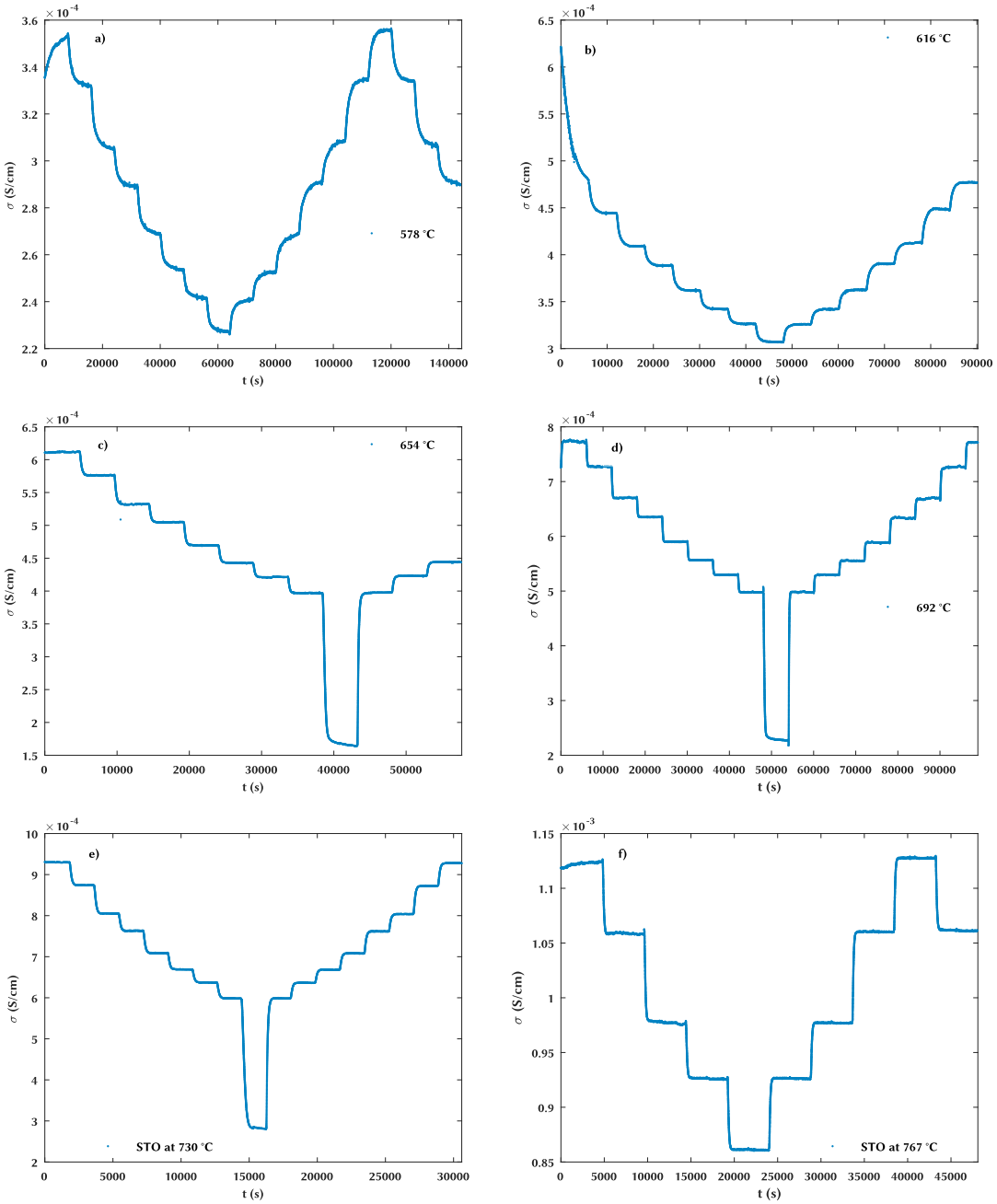

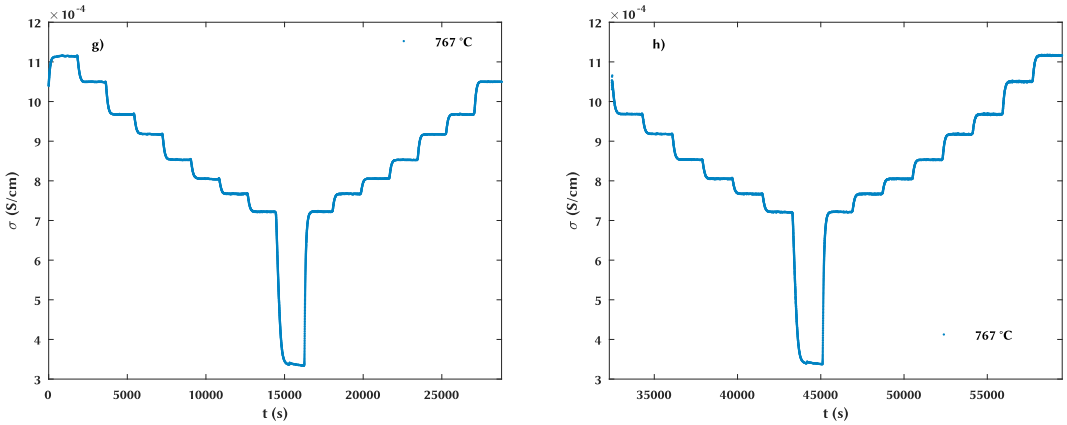

Figure 4.3.: Conductivity relaxation of a STO single crystal at different temperatures. σ is plotted against the time. The initial oxygen partial pressure was 0.2 bar for all experiments. **c)-e)** and **g)** include steps where the oxygen was cut from the gas flow.

The obtained equilibrium conductivity values of the STO single crystal are plotted against the oxygen partial pressure in a log-log plot (see Figure 4.4). Clearly, σ increases with increasing temperature and decreases with decreasing pO_2.

Figure 4.4 shows that the data points lie a on straight line for each temperature. Therefore it was assumed that a power law was applicable to describe the oxygen partial pressure dependence of σ, $\sigma \propto pO_2^n$. Fitting the data points yielded similar n values in the range of $0.1665 - 0.1954$. The fitting results are summarized in Table 4.2.

Table 4.2.: Results of fitting the obtained equilibrium σ values to a power law, $\sigma \propto pO_2^n$.

T (°C)	n
616	0.1724
654	0.1666
692	0.1717
730	0.1717
767	0.1954
767	0.1665

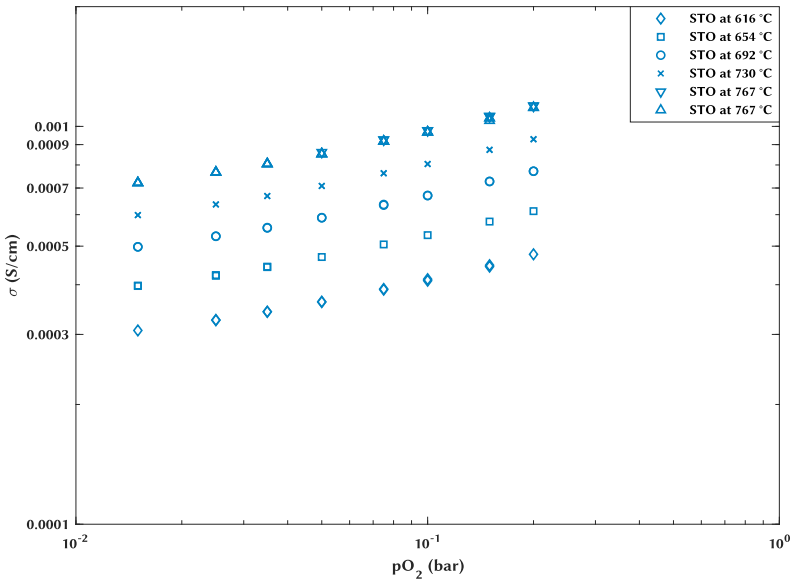

Figure 4.4.: Equilibrium conductivity σ vs. the pO_2 in the surrounding atmosphere of a STO single crystal at different temperatures. Note that a logarithmic scale is used on the x- and y-axis.

b) Fe:STO

The conductivity relaxation experiments which were conducted on the Fe:STO single crystal are shown in Figure 4.5.

An overall change in conductivity due to the oxygen partial pressure steps in reducing direction is visible for the Fe:STO single crystal at 542 °C (Figure 4.5a). The individual transient responses, however, can't be distinguished. Two factors are contributing to this behavior. Firstly, the electrical contact during the measurement was possibly not well defined as the Pt tips weren't brushed with Pt paste before contacting the sample. This might have caused contact resistances and flattened the transient response. Secondly, the surface kinetics are temperature dependent and will therefore be slower at 542 °C compared to the measurements at e.g. 616 °C. Thus, the time required to equilibrate the sample would have been longer than the chosen 7200 s.

Two experiments were carried out at 616 °C (Figure 4.5b,c). The pO_2 steps are less defined in Figure 4.5b as, again, the Pt tips weren't brushed with Pt paste before the sample was contacted. It was not possible to evaluate the equilibrium conductivity for both measurements as the sample wasn't able to reach an equilibrium state with the surrounding atmosphere in the given experimental duration in either case.

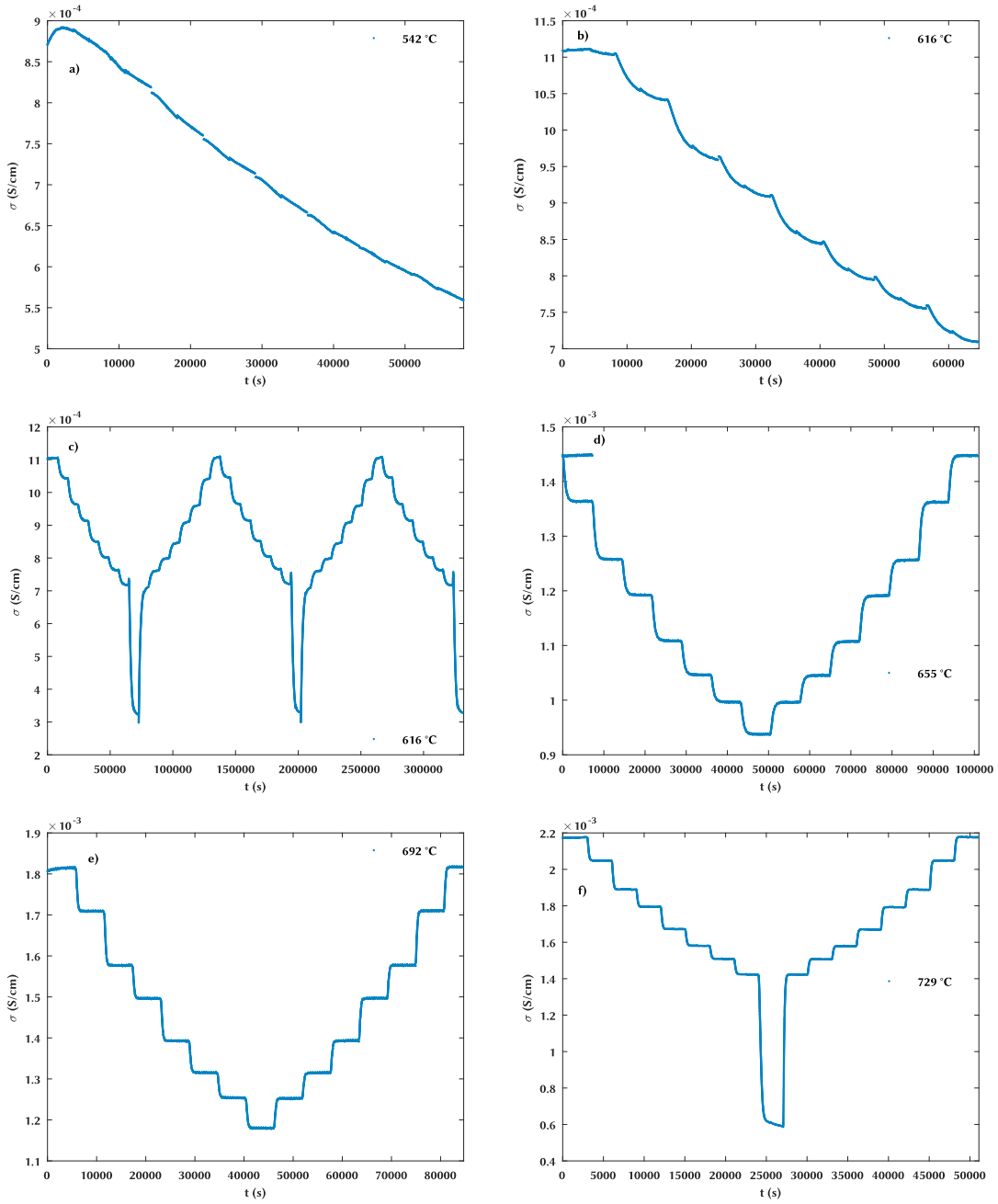

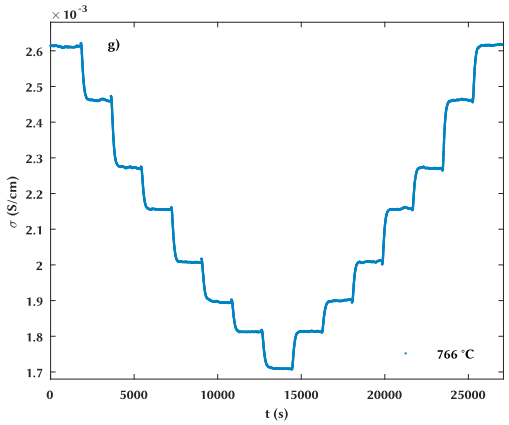

Figure 4.5.: Conductivity relaxation of a Fe:STO single crystal at different temperatures. σ is plotted against the time. The initial oxygen partial pressure was 0.2 bar for all experiments. **c)** and **f)** include steps where the oxygen was cut from the gas flow.

On a side note it is mentioned, that the experiment at 655 °C was paused before the pO_2 was switched for the first time. After restarting the experiment the time recording started again at 0 s. Nevertheless, both measurements are plotted together in Figure 4.5d. In case of the experiments which were carried out at 616 °C and 729 °C the oxygen was also cut from the gas stream (see Figure 4.5c,f).

Figure 4.6 shows the oxygen partial pressure dependence of σ for the Fe:STO single crystal at different temperatures. As for the STO single crystal, it is observed that σ increases with increasing temperature and decreases with decreasing pO_2. The absolute values of σ of the Fe:STO single crystal, however, are higher by approximately a factor of 2.3 for each temperature and independent of pO_2.

The exponents n, that were obtained from fitting the equilibrium σ values of the Fe:STO single crystal to the above mentioned power law, are quite similar to the n values of the STO single crystal and range from $0.1662 - 0.1738$ (see Table 4.3).

Table 4.3.: Results of fitting the obtained equilibrium σ values to a power law, $\sigma \propto pO_2^n$.

T (°C)	n
655	0.1738
692	0.1695
729	0.1662
766	0.1699

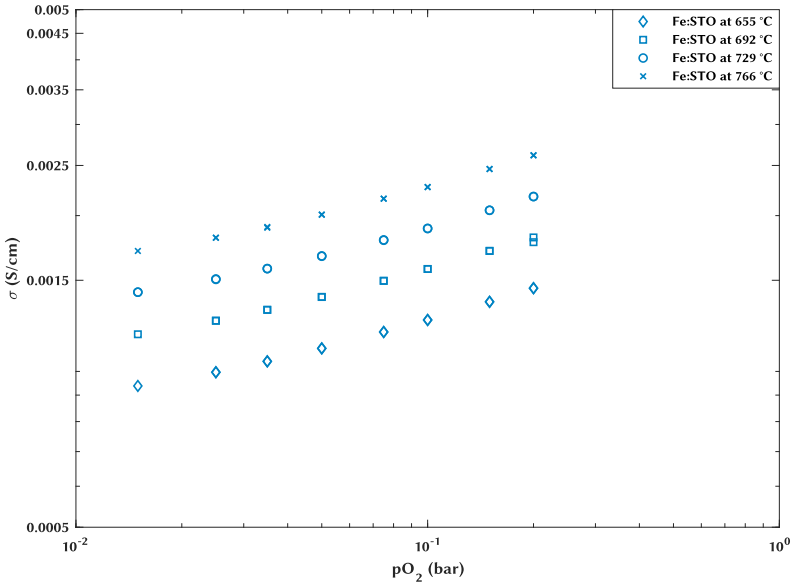

Figure 4.6.: Equilibrium conductivity σ vs. pO_2 in the surrounding atmosphere of a Fe:STO single crystal at different temperatures. Note that a logarithmic scale is used on the x- and y-axis.

c) Discussion

Equilibrium conductivity values for STO and Fe:STO single crystals were evaluated in a high pO_2 regime, in which the conductivity of the material is known to be p-type [22]. The conductivity of (Fe:)STO increases as oxygen is incorporated into the crystal lattice since two electron holes are generated simultaneously [22]:

$$\frac{1}{2}O_2 + V_O^{\bullet\bullet} \rightleftharpoons O_O^{\times} + 2h^{\bullet}. \tag{4.1}$$

This matches the observed behavior of the STO and the Fe:STO single crystal, since σ increased in each instance with increasing oxygen partial pressure in the surrounding atmosphere. The theoretical oxygen partial pressure dependence of σ in this pO_2 range can be derived using the mass action law of Equation (4.1) [22]

$$\frac{[h^{\bullet}]^2}{[V_O^{\bullet\bullet}]pO_2{}^{1/2}} = K(T), \tag{4.2}$$

with K denoting the equilibrium constant, which is temperature dependent. The charge neutrality condition (Equation (2.6), section 2.1) reduces to

$$[\mathrm{Fe}'_{\mathrm{Ti}}] \approx 2[\mathrm{V}_{\mathrm{O}}^{\bullet\bullet}], \tag{4.3}$$

in the investigated temperature and pO_2 range. That is, the electron hole concentration (as well as the concentration of electrons) is small compared to the oxygen vacancy concentration [48]. Inserting Equation (4.3) in Equation (4.2) gives the theoretically expected oxygen partial pressure dependence of the conductivity for (Fe:)STO [42]

$$[\mathrm{h}^{\bullet}] \propto (K(T)[\mathrm{Fe}'_{\mathrm{Ti}}])^{1/2} {pO_2}^{1/4}, \tag{4.4}$$

$$\sigma \propto [\mathrm{h}^{\bullet}] \propto {pO_2}^{1/4}. \tag{4.5}$$

This derivation also holds for the undoped STO single crystal in the investigated pO_2 range as strontium vacancies are introduced during fabrication which act as intrinsic acceptors since they are immobile below approximately 1000 °C [22, 42, 48].

The pO_2 dependence of the equilibrium conductivity of the STO and Fe:STO single crystal in this work was found to be roughly $\sigma \propto {pO_2}^{0.17}$ in each instance (see Figure 4.4, Figure 4.6), which is fairly close to the theoretical dependence. The higher σ values of the Fe:STO single crystal are the result of the deliberate iron doping. This can be understood by means of Equation (4.3) - Equation (4.5). Since the acceptor concentration will be higher in the Fe:STO single crystal compared to the weakly doped STO single crystal, the contribution of said concentration will result in a higher electron hole concentration and thus the conductivity of the deliberately doped Fe:STO single crystal will exceed the conductivity of the STO single crystal. Furthermore, the σ values, that were obtained for the Fe:STO single crystal, are found to be of the same order of magnitude as values, that were derived in previous works [22, 42].

4.2.2. Kinetic parameters

The following subsection will discuss the evaluation of kinetic parameters from relaxation data of the STO and Fe:STO single crystal, respectively. It should be mentioned at the beginning that flaws in the fitting procedure (e.g. unconstrained fitting parameters, unknown precise value of τ_f) as well as the influence of the flush time itself, hindered the evaluation of the relaxation data in general. The fitting process is described in subsection 3.4.2.

a) STO

Before the relaxation data could be fitted to the theoretical equations, the relaxation behavior of the STO single crystal had to be examined to ensure that the flush time of the reactor did not superpose the relaxation time of the sample, τ_r. Figure 4.7 shows example relaxation profiles of the STO single crystal at different temperatures. The normalized conductivity is plotted against the experimental duration, that was chosen for the respective pO_2 steps. The oxygen partial pressure was switched between 0.2 bar and 0.15 bar in reducing direction in each instance.

The analysis of the transient responses, which are shown in Figure 4.7, is based on their corresponding overall time constant. Additionally, the value of the reactor flush time, that was experimentally obtained from conductivity relaxation experiments on LSC thin films (τ_f =189 s, see subsection 4.4.1), is used as a reference point to asses if the evaluation of the relaxation data to obtain kinetic parameters (D_{chem} and/or k_{chem}) is valid.

Figure 4.7 shows that the relaxation process of the STO single crystal is accelerated as the temperature increases. The time constant of the whole relaxation process, which is shown in Figure 4.7a, is approximately 750 s, which means that both τ_f and τ_r are contributing to the relaxation process. This is also the case for the relaxation process of the experiment, that was carried out at 654 °C. The time constant of the transient response is approximately 290 s. The time constants of the relaxation profiles shown in Figure 4.7c,d,e are relatively similar and amount to ≈180 s, ≈160 s and ≈150 s. The fact that the time constant hardly changes with increasing temperature suggests that the underlying process is only weakly temperature dependent, which therefore indicates that only the flush time of the reactor was measured throughout these experiments [63]. Furthermore, this hypothesis is corroborated by the fact that the time constants are in the same range as the experimentally derived τ_f value.

Based on the findings from Figure 4.7, it was concluded that only the experiments at 616 °C and 654 °C could be evaluated for kinetic parameters. The surface exchange was found to be limiting during each experiment ($L < 0.03$). As a consequence only k_{chem} could be obtained from the respective relaxation data (Figure 4.3b,c).

The evaluation of the surface exchange coefficient at 616 °C was challenging and did not yield trustworthy results for k_{chem} as well as τ_f. Figure 4.8a corresponds to Figure 4.7a and exemplifies the issue. The fitted curve represents the normalized profile reasonably well, k_{chem} seems reasonable compared to literature data [28] but τ_f amounts to only 51 s, which is not plausible in comparison to the experimentally obtained τ_f value. Since both τ_f and τ_r are con-

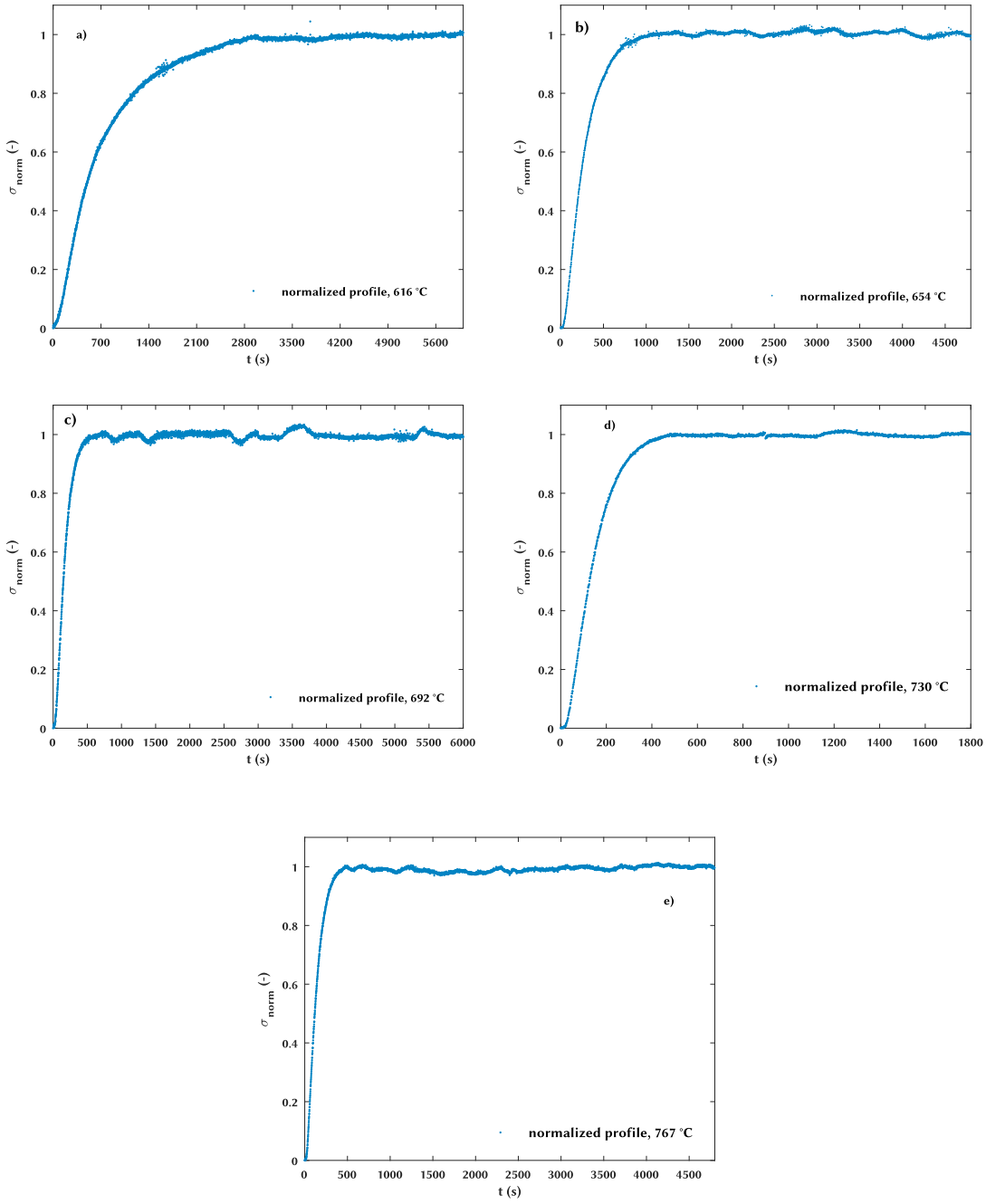

Figure 4.7.: σ_{norm} of the STO single crystal is plotted against the time. The pO_2 was switched between 0.2 bar and 0.15 bar in reducing direction for all profiles. **a) and b)** The overall time constant is ≈750 s and ≈290 s. τ_f and τ_r affect the relaxation profile. **c)-e)** The time constant is less than 200 s in each instance. k_{chem} cannot be evaluated from these profiles as τ_f is greater than τ_r.

tributing to the relaxation process, it follows that the fitted value of k_{chem} has to be doubted as well. This behavior was observed for all relaxation profiles of this measurement independent of the respective pO_2 step. Output values for the flush time were obtained in the range between ≈50 s and ≈70 s. As the precise value of the flush time is unknown and may even change depending on temperature or pO_2, it was attempted to fit the profile with a defined upper and lower bound for τ_f. However, attempts to constrain τ_f between 150 s and 250 s did not yield satisfactory results either as output values of τ_f equaled the lower bound (Figure 4.8b). The same behavior was observed after the value of the lower bound was changed. Furthermore, Figure 4.8b shows that constraining τ_f led to fitted curves, which deviate considerably from the normalized profile, which suggests that Equation (3.6) does not fully represent the relaxation process. The electrical contacts were brushed onto the four edges of the STO single crystal using a Pt paste. Since Pt coatings are known to accelerate the surface exchange on STO [12], the oxygen incorporation will probably be slower on the remaining bare STO surface. Kinetically different surface exchange rates resulting from the sample preparation, which contribute to the relaxation process and therefore influence the shape of the normalized profile, might therefore be a possible explanation as to why no plausible fitting results could be obtained. However, this behavior was only encountered for this particular measurement and has not been investigated more thoroughly during this work. Consequently, no results for k_{chem} at 616 °C could be obtained since the relaxation data could not be fitted properly to Equation (3.6).

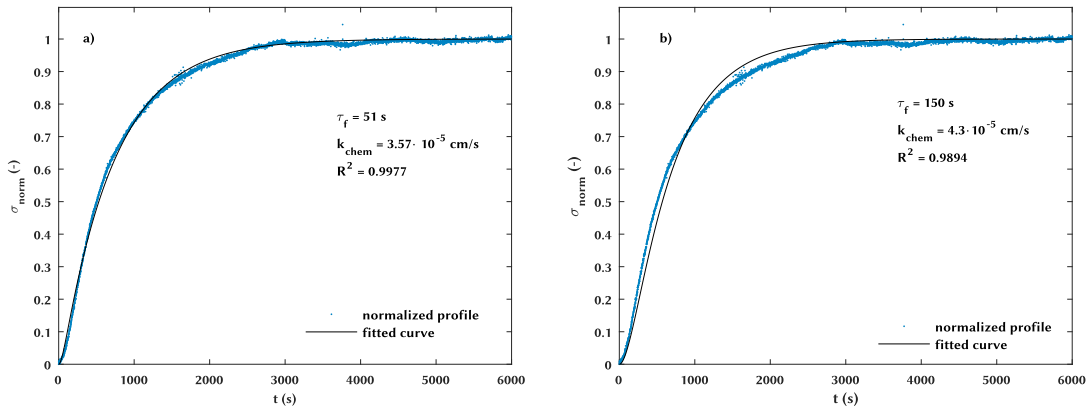

Figure 4.8.: Normalized relaxation profile of the STO single crystal at 616 °C. Fitted curves, that were obtained by fitting the measured data to Equation (3.6), are represented by solid lines. **a)** Unconstrained fit of the relaxation profile. Fitted τ_f value , **a), b)** correspond to Figure 4.3b and Figure 4.7a, respectively.

Figure 4.9a shows again the normalized relaxation profile of the pO_2 step between 0.2 bar and 0.15 bar at 654 °C as well as the fitted curve, that was obtained by fitting the relaxation data to Equation (3.6). The normalized profile and the fitted curve are in good agreement. Furthermore, in contrast to the measurement at 616 °C reasonable output values for k_{chem} ($= 2.79 \cdot 10^{-4} cm/s$) and τ_f ($= 193$ s) were obtained. However, obtained results had to be examined carefully as the overall time constant of the relaxation process, as already mentioned above, was less than 300 s for each pO_2 step. By comparing the experimentally obtained value of τ_f and the fitted τ_f value to the approximate time constant of the relaxation process, it becomes clear that the flush time mainly contributes to the transient response. According to Otter et al., the sample acts as an oxygen sensor if τ_r is less than approximately 1/3 of τ_f [63]. Fitting results, that matched this definition, were therefore disregarded. For the example profile shown in Figure 4.9a the surface exchange coefficient translates to a specific relaxation time of approximately 90 s (see Equation (3.10)), which is approximately half of τ_f. Hence, the fitting results were accepted in this instance. The specific relaxation time was found to be less than 1/3 of τ_f for the pO_2 steps 6 and 8-12 (see Figure 4.3c) and were therefore not considered.

The obtained k_{chem} values are presented in Figure 4.9b, k_{chem} is plotted against the logarithm of the final pO_2. Although the evaluation of the relaxation data yielded similar k_{chem} values in the range between $2.6 \cdot 10^{-4} cm/s$ and $3.6 \cdot 10^{-4} cm/s$, no pO_2 dependence is observed. The scatter in the obtained k_{chem} values is assumed to be the result of the flush time's major influence on the transient response since the results were obtained in close proximity to the aforementioned boundary condition. The evaluation of k_{chem} might therefore already be restricted by the superposed flush time. Furthermore, it is fair to assume that the flush time could be evaluated with higher accuracy compared to the surface exchange coefficient in these instances.

b) Fe:STO

Again, due to the strong influence of the flush time during the experiments the measured relaxation data of the Fe:STO single crystal had to be analyzed as well in order to decide if the evaluation of a specific data set was valid or not. The approach was the same as for the STO single crystal, which was already described above. Figure 4.10 shows the transient response for a pO_2 step between 0.2 bar and 0.15 bar of the Fe:STO single crystal at four different temperatures. At 655 °C as well as at 692 °C the polarization was changed every 240 s. Upon the polarization change, charge carriers were possibly shifted inside the material, which explains the visible spikes in the measured data (Figure 4.10a,b).

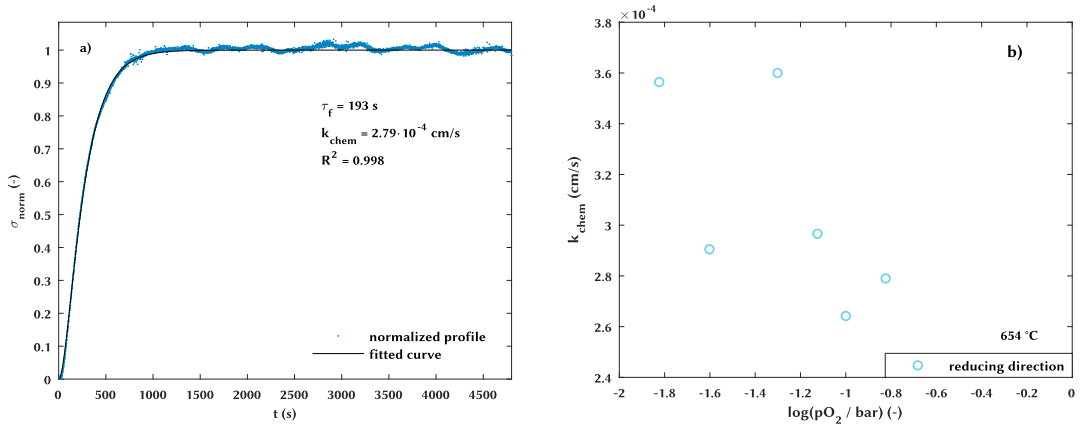

Figure 4.9.: STO single crystal at 654 °C. **a)** σ_{norm} vs. time, the pO_2 was switched between 0.2 bar and 0.15 bar. The solid line represents the fitted curve, that was obtained by fitting the relaxation data to Equation (3.6). **b)** k_{chem} vs. the logarithm of the final pO_2. No clear pO_2 dependence is visible.

The Fe:STO single crystal established a new equilibrium state with the surrounding atmosphere after a pO_2 step had been applied more slowly than the STO single crystal. At 655 °C and 692 °C it is assumed that both the flush time of the reactor and the specific relaxation time of the sample contribute to the relaxation process as the overall time constants are approximately 700 s and 350 s (Figure 4.10a,b). At 729 °C and 766 °C the overall time constants are ≈200 s and ≈180 s (Figure 4.10c,d). Thus, both values are in the range of the experimentally obtained value of τ_f and the flush time is therefore suspected to be the main contributor to these transient responses. As a result, only the experiments, which were carried out at 655 °C and 692 °C, were subsequently evaluated for kinetic parameters.

As for the STO single crystal, the relaxation process of the Fe:STO single crystal was found to be limited by the surface exchange. The surface exchange coefficient and the equillibrium conductivity were therefore the two parameters, that could be extracted from the relaxation data. Figure 4.11a,b correspond to Figure 4.10a,b. In addition to the normalized profiles the respective fitted curves are presented, which were obtained by fitting the relaxation data to Equation (3.6). Apart from minor deviations of the fitted curve in the initial increase of σ_{norm} in Figure 4.11b, the normalized profiles and the fitted curves are in agreement. Furthermore, the extracted values for k_{chem} and τ_f seem reasonable in both instances. Obviously, a higher value for k_{chem} and a lower value for τ_f are obtained in case of the experiment, that was carried out at 692 °C (Figure 4.11b), due to the higher temperature during the experiment. Comparing

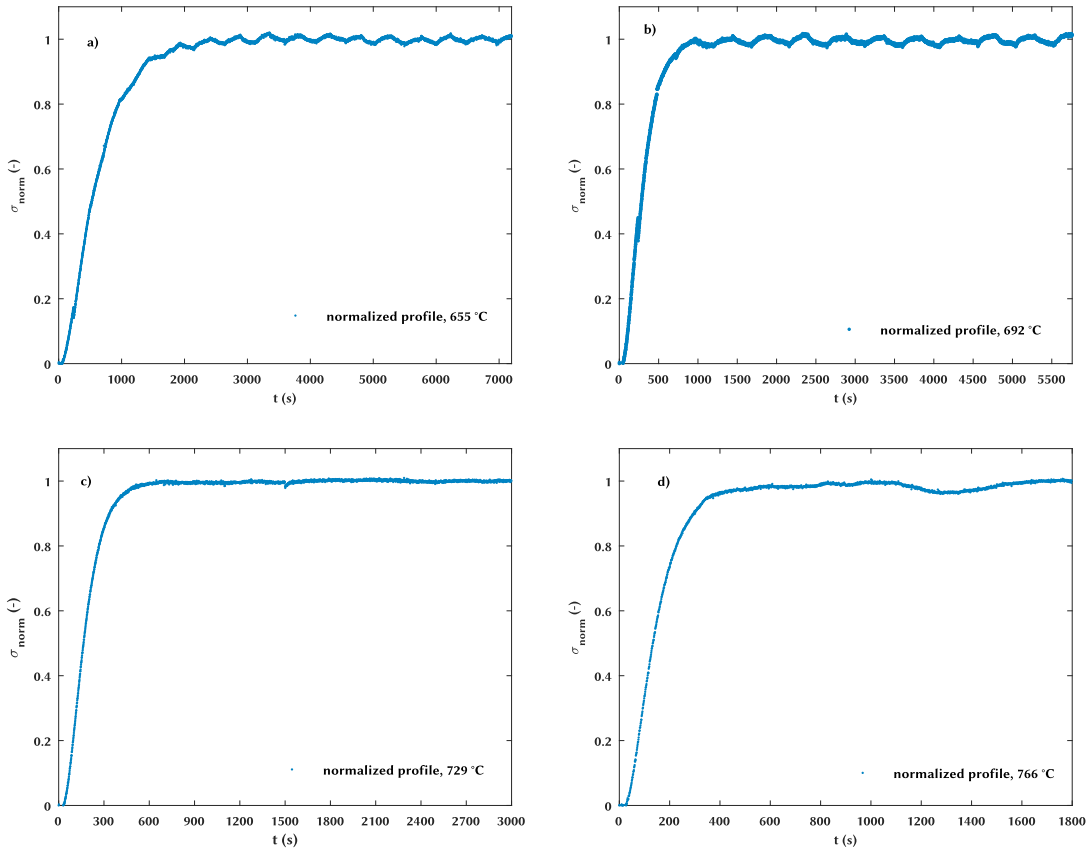

Figure 4.10.: Normalized relaxation profiles of the Fe:STO single crystal at different temperatures. The pO_2 was switched between 0.2 bar and 0.15 bar in reducing direction for all profiles. **a), b)** The time constant of these profiles is approximately 700 s and 400 s. Both τ_f and τ_r affect the relaxation profile. **c)** The time constant is approximately 200 s. **d)** The time constant is less than 200 s. The profiles in **c), d)** are mainly influenced by the flush time of the reactor.

the values of k_{chem} for the STO and Fe:STO single crystal at 654 °C and 655 °C shows that the surface exchange coefficient of the STO single crystal exceeds the surface exchange coefficient of the Fe:STO single crystal by approximately a factor of 6.

As the overall time constant of the relaxation process shown in Figure 4.10b was only roughly 350 s, it is mentioned that the value of the fitted surface exchange coefficient of this relaxation profile corresponds to a specific relaxation time of 167 s (Figure 4.11b). Thus, τ_f and τ_r were approximately equal in this instance. Similar values of τ_f and τ_r were also obtained for the remaining pO_2 steps, which enabled an evaluation of k_{chem} for each transient response at 692 °C.

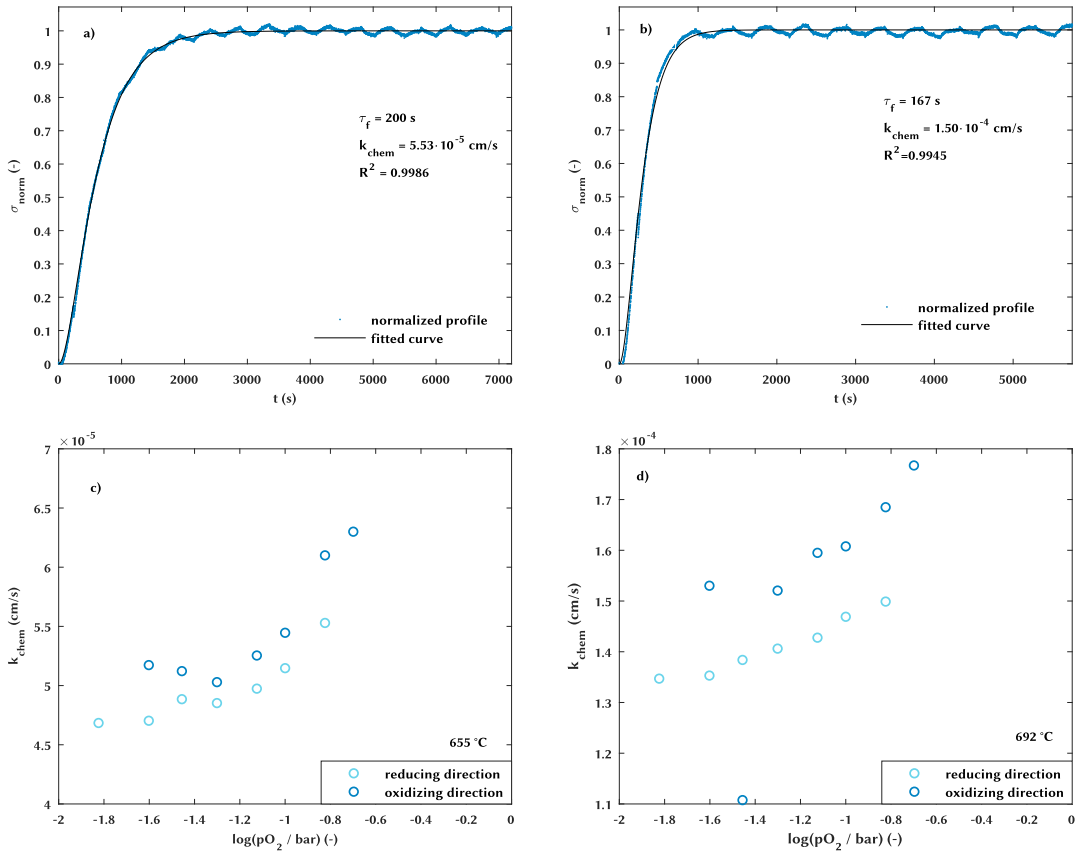

Figure 4.11.: Fe:STO single crystal at 655 °C and 692 °C. **a), b)** σ_{norm} vs. time, the pO_2 was switched between 0.2 bar and 0.15 bar. The solid lines represent the fitted curves, that were obtained by fitting the relaxation data to Equation (3.6). **c), d)** pO_2 dependence of the surface exchange coefficient. Markers in light blue show values, that were obtained from reducing subcycles, whereas markers in dark blue represent values, that were obtained form oxidation subcycles.

In Figure 4.11c,d the obtained surface exchange coefficients are plotted against the logarithm of the final oxygen partial pressure of the respective pO_2 step. Irrespective of the direction in which the pO_2 was switched, k_{chem} decreased at 655 °C as well as at 692 °C with decreasing pO_2. However, k_{chem} values, that were extracted from oxidation runs, are found to be slightly higher compared to the values, which were obtained from reducing runs. Plotting k_{chem} against pO_2 in a log-log plot, revealed that a power law ($k_{chem} \propto {pO_2}^n$) was applicable. The obtained n values are summarized in Table 4.4. The outlier in Figure 4.11d was not included in the fitting process. Table 4.4 shows that the pO_2 dependence is slightly higher for both measurements if the pO_2 is switched in oxidizing direction.

Table 4.4.: Results of fitting the obtained k_{chem} values (see Figure 4.11c,d) to a power law, $k_{chem} \propto {pO_2}^n$.

T (°C)	n_{red}	n_{ox}
655	0.07	0.10
692	0.05	0.07

The k_{chem} value, which was obtained for the pO_2 step between 0.025 bar and 0.035 bar in oxidizing direction at 692 °C, is somewhat lower compared to all other extracted surface exchange coefficients of this measurement (see Figure 4.11d). In this instance the obtained flush time value was only ≈122 s, which translated to a lower k_{chem} value since the specific relaxation time was seemingly increased (τ_r ≈226 s) in relation to the other pO_2 steps. The 'real' value of τ_f was inaccessible since no oxygen sensor was included in the measurement setup and outliers like this were therefore accepted.

c) Discussion

It was observed, that the relaxation kinetics of the STO single crystal were faster compared to the Fe:STO single crystal. This can be understood by means of the following equation, that was given by Merkle and Maier for Fe-doped STO [22]:

$$k_{chem} = 4\frac{\mathscr{R}_0}{RT}\frac{\partial \mu_O}{\partial c_O} = 4\mathscr{R}_0\left(\frac{1}{[V_O^{\bullet\bullet}]} + \chi_{h^\bullet}\frac{4}{[h^\bullet]}\right), \tag{4.6}$$

with $\mathscr{R}_0$ denoting the equilibrium exchange rate and $\chi_{h^\bullet}$ denoting a differential 'trapping factor' ($0 < \chi < 1$). The trapping factor describes differential change of the free electron hole concentration to the differential change of the total concentration of holes in the material [13].

It has to be taken into account if an internal source and sink term, such as $Fe_{Ti}^{\times} \rightleftharpoons Fe'_{Ti} + h^{\bullet}$ for Fe:STO, has to be considered. Consequently, oxygen incorporation not only leads to simultaneous annihilation of oxygen vacancies and formation of electron holes but also to formation of holes, which are trapped ($\widehat{=}$ immobilized) at $Fe_{Ti}^{\times}$ sites [22]. As a result of the internal redox reaction, the material is able to undergo a greater change in the oxygen nonstochiometry, causing $(\partial c_O/\partial \mu_O)^{-1}$ ($\widehat{=}$ chemical capacitance) in Equation (4.6) to increase [22]. Since the other quantities in Equation (4.6) are assumed to be constant, the value of the surface exchange coefficient has to decrease. Generally, trapping effects also cannot be ignored for nominally undoped materials since, as already mentioned, redox active impurities might be present [22]. However, in context of this work Equation (4.6) is merely used to comprehend the observed differences in the relaxation behavior of the STO and Fe:STO single crystal. Assuming that the trapping effect has a greater impact on the deliberately doped Fe:STO single crystal, it follows from Equation (4.6) that the surface kinetics of said sample are slower and thus, the obtained values of k_{chem} are lower compared to the nominally undoped STO single crystal.

A comparison of the obtained k_{chem} values to literature data in terms of absolute values is not straightforward since the surface kinetics do not only depend on temperature, surrounding pO_2 and doping content but also on surface decoration, e.g. metal or metal oxide films [12]. Both the STO and Fe:STO single crystal had four Pt electrical contacts. It is reasonable to assume that the oxygen incorporation (or release) following a pO_2 step was accelerated at the triple phase boundary of the Pt contacts compared to the remaining bare surface of the respective single crystal. Thus, the impact of the Pt contacts on the surface kinetics can't be neglected and an interpretation of the obtained k_{chem} values has to be carried out accordingly.

The iron concentration of the Fe:STO single crystal was 0.16 mol%, which translates to a Fe content of $2.7 \cdot 10^{19} cm^{-3}$ based on the Ti content and a STO lattice constant of 0.391 nm [79]. Leonhardt et al. investigated the oxygen incorporation into Fe:STO single crystals by optical absorption spectroscopy [12]. They obtained a k_{chem} value of $\approx 5 \cdot 10^{-6} cm/s$ for a pO_2 step between 0.1 bar and 1 bar at approximately 653 °C for bare Fe:STO ([Fe]= $4.6 \cdot 10^{19} cm^{-3}$). In contrast, the obtained values of the surface exchange coefficient at 655 °C in this work exceed the values obtained by Leonhardt et al. by approximately one order of magnitude. This pronounced difference is possibly the result of two factors. Firstly, the Pt contacts, that were used for the van der Pauw measurement, may have accelerated the surface kinetics. Secondly, the iron concentration of the single crystal used in this work was slightly lower and the previously discussed trapping effect might therefore be reduced resulting in higher k_{chem} values. Merkle and Maier also investigated the surface kinetics of Fe:STO single crystals by optical absorption spectroscopy [28]. At 650 °C and 700 °C they obtained k_{chem} values for a Fe:STO single crystal

([Fe]= $1.4 \cdot 10^{19} cm^{-3}$) of $\approx 6 \cdot 10^{-5} cm/s$ and $\approx 3 \cdot 10^{-4} cm/s$, respectively [28]. The pO_2 was 0.08 bar in both instances. These values are in good agreement with the values of the surface exchange coefficient, which were obtained in this work, even though the previous line of argumentation would suggest that slower surface kinetics prevailed during the experiments since the Fe content of the single crystal used in this work was higher. Since the cited values of Merkle and Maier were, however, also obtained for bare Fe:STO it seems plausible to attribute the close correspondence between the data sets to the fact that the Pt contacts reduced the impact of the trapping effect since, as already mentioned, the surface kinetics are accelerated in presence of metal films [12]. Consequently, the comparison to literature data shows that the order of magnitude of the obtained k_{chem} values appears to be reasonable. Moreover, the observed pO_2 dependence of the surface exchange coefficient for the Fe:STO single crystal, decreasing k_{chem} values with decreasing pO_2, is also in accordance with both cited works [12, 28].

In regard to absolute values of k_{chem} the role of τ_f should also be discussed. One might have noticed that the fitted values of τ_f at 654 °C and 655 °C were approximately 200 s (Figure 4.8a, Figure 4.11a), which is well within the range of the experimentally estimated value of the flush time, that was derived from measurements on LSC thin films at a furnace set temperature of 500 °C (see subsection 4.4.1). This seems somewhat inconsistent since τ_f should decrease with increasing temperature due to thermal expansion of the gas. However, estimating the level of uncertainty with respect to the obtained values is difficult as no oxygen sensor was installed in the measurement setup. Still, it seems reasonable to assume that the 'reality' is reflected more accurately by the experimentally derived τ_f value as the majority of the fitted values from the four respective experiments were all scattered around 200 s (see subsection 4.4.1). It would therefore follow that the obtained absolute values of the surface exchange coefficient for the STO and the Fe:STO single crystal are in fact lower than the values shown in Figure 4.8b and Figure 4.11c,d since the actual flush time values are possibly lower than the fitted values, which were obtained from Equation (3.6). Furthermore, this discussion shows that the chosen fitting approach with τ_f being a fitting parameter is only advisable, if knowledge of the flushing behavior of the reactor is available. Even though in this case, setting bounds for τ_f or fixing τ_f would certainly seem like a more appropriate approach.

Previous investigations of the oxygen exchange kinetics of different mixed ionic and electronic conducting materials, that were carried out using the conductivity relaxation method, frequently showed differences in the relaxation behavior of oxidation and reduction runs [9, 11, 80]. Preis showed by finite element modeling that deviations in the kinetic parameters (D_{chem}, k_{chem}) from oxidation and reduction runs are explainable, if the concentration dependence of

the kinetic parameters is taken into account [81]. Differences might also originate from mass transport limitations [82]. Generally, the surface exchange coefficient depends on the final pO_2 of a respective oxygen partial pressure step [62]. In theory, the final pO_2 should be attained rapidly, if the reactor volume is small and fast gas changes can be ensured. However, in case of this work the final pO_2 was gradually reached due to a large reactor volume ($> 500\,cm^3$), which would theoretically give rise to mass transport limitations [82]. Obviously, this is also dependent on the gas flow rate. A high gas flow rate minimizes the risk of mass transport limitations to some extend. Nevertheless, if said limitations prevail the pO_2 steps in reducing direction are faster compared to the respective steps in oxidizing direction [82]. The measured relaxation behavior of the Fe:STO single crystal, however, doesn't point to limitations in the gas phase. Figure 4.12 shows that the pO_2 step in oxidizing direction is slightly faster for both temperatures, at which the surface exchange coefficient could be evaluated. This behavior was already reflected by Figure 4.11.

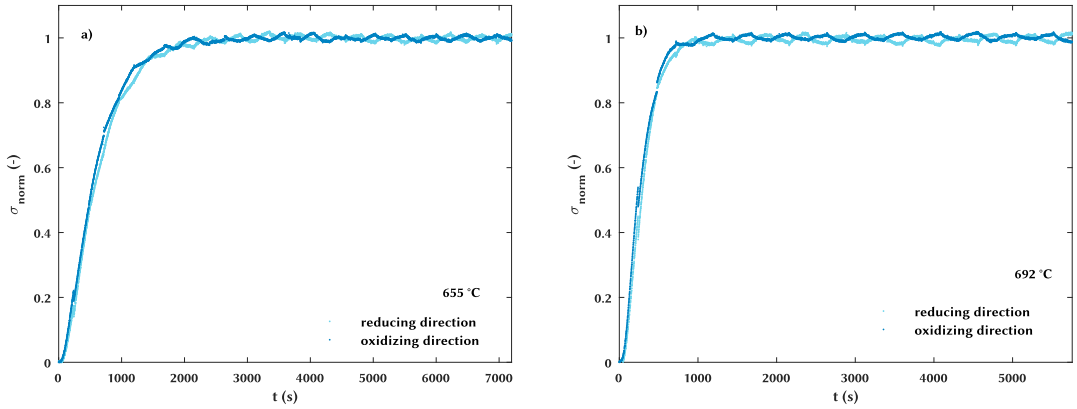

Figure 4.12.: Fe:STO single crystal at **a)** 655 °C and **b)** 692 °C. The data, which is plotted in light blue, corresponds to a pO_2 step between 0.2 bar and 0.15 bar in reducing direction. The data, which is plotted in dark blue, was obtained from a pO_2 step between 0.1 bar and 0.15 bar in oxidizing direction.

According to Preis, it might be possible that, dependent on the chosen gas flow rate and the chosen pO_2 step magnitude, mass transport limitations prevail but that the resulting effect is canceled by the contrary effect of the oxygen non-stoichiometry dependence of the kinetic parameters, which leads to faster oxidation runs [81]. In context of this work, the Pt contacts might also play a role. Table 4.4 showed that the pO_2 dependence was slightly higher for the pO_2 steps in oxidizing direction. A possible explanation might be that even though Pt accelerates the oxygen incorporation, it might not necessarily contribute to the oxygen release and thus, slightly faster oxidation steps might be the result. However, this hypothesis has not been

tested in the course of this work. Furthermore, at this point it can't be determined which of the previously discussed factors effectively contributed to the differences between oxidation and reduction runs. In summary, several shortcomings of the setup were identified and considering these, a completely new setup was designed. Main aspects are structural changes to allow for minimal reactor volume in the range of few mL and the possibility to measure the pO_2 of the reactor on-line.

4.3. LSC polycrystals

The conductivity relaxation experiments, which were conducted on the LSC pellets, were extremely challenging and did neither yield reliable results for the kinetic parameters nor for the equilibrium conductivity. The experimental execution was optimized continuously, including the following steps: reducing the sample thickness to achieve a higher sample resistance, upgrading the shielding of the measurement setup to prevent signal interference and placing the multimeter next to the switch box to reduce the length of the wires and along with that minimize potential interfering lead resistances. As neither of these changes allowed the desired measurement quality, only a short overview of the measurements is shown here, and more experimental focus was laid on LSC thin films, see section 4.4.

Figure 4.13 shows a measurement that was performed on a 0.056 cm thick LSC pellet at 560 °C with an applied input voltage of 0.1 V. The experiment was conducted after the shielding of measurement setup had been renewed.

In addition to the extreme noise in the measured signal, it is not possible to distinguish the single pO_2 steps. This is due to the low resistance of LSC, resulting in low voltages. Only 0.08 % - 0.5 % of the applied input voltage instead of the required 10 % could be read from the multimeter for all experiments that were conducted on polycrystalline LSC. In addition, the electrical resistance, which stemmed from the van der Pauw measurement setup, complicated the experiments. The temperature dependence of the setup's electrical resistance was obtained by measuring a Pt sheet in the temperature range between 180 °C and 745 °C. Before placing the sheet into the measurement setup, the Pt sheet was ground with a 4000 grit grinding paper (Struers), washed in ethanol and dried with N_2. For both configurations of the switch box, 1234 and 2341, the resistance increased linearly with increasing temperature and the resistances varied between approximately 7 Ω and 11 Ω in the above mentioned temperature range. Consequently, in order to obtain accurate data the electrical resistance of a sample

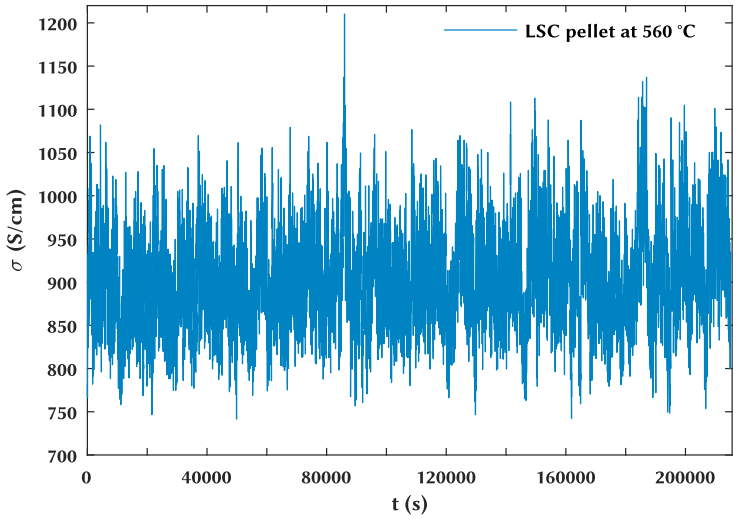

Figure 4.13.: Conductivity relaxation experiment conducted on a 0.056 cm thick LSC sample at 560 °C. The applied input voltage was 0.1 V.

had to exceed the resistance stemming from the setup. However, in case of the LSC pellets, the electrical resistance, which was calculated from the applied voltage and the measured current, was in the same range.

Conductivity relaxation of polycrystalline LSC was observed when higher input voltages were applied. Figure 4.14 shows a measurement that was done on the same 0.056 cm thick LSC sample. The average temperature during the experiment that was read out by the thermocouple was 648 °C, the applied input voltage was 4 V. In this case the single oxygen partial pressure switches are distinguishable. The signal is again very noisy and in some cases the transient responses exhibit a drift in the measured conductivity. Fitting these relaxation profiles to the theoretical equations would be challenging. However, in addition to the poor quality of the data, the sample was exposed to Joule heating. The average current during the course of the experiment was approximately 0.38 A, which results in an input power of 1.52 W. This value is greater than the value of 0.01 W that was originally postulated to avoid heating of the material. Consequently, an evaluation of the data would produce questionable results since the temperature of the sample is unknown.

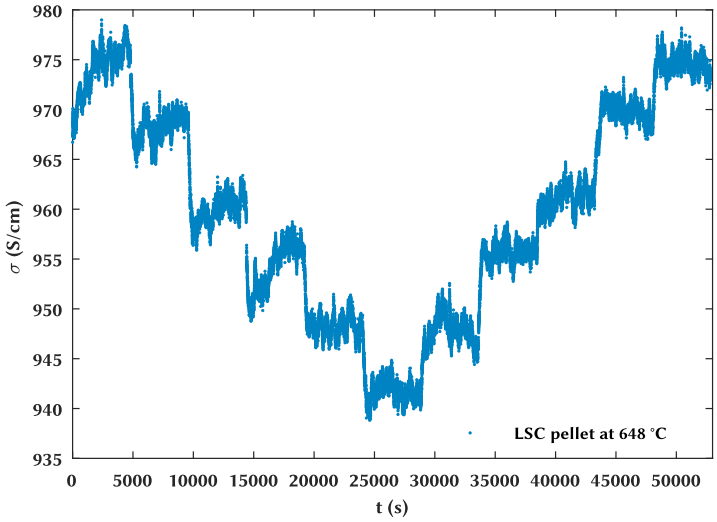

Figure 4.14.: Conductivity relaxation experiment conducted on a 0.056 cm thick LSC pellet at 648 °C. The applied input voltage was 4 V.

Egger et al. succeeded to obtain kinetic parameters and values of the electrical conductivity of a 0.204 mm thick LSC sample using the van der Pauw method [6]. Compared to this work, the sample was thinner resulting in a higher resistance. In addition they used a nanovoltmeter that is sensitive to low voltages.

4.4. LSC thin films

4.4.1. Estimation of the reactor flush time

As described in subsection 3.4.2, the relaxation profiles of the LSC thin films in the temperature range between 267 °C and 466 °C were fitted against Equation (3.17). This was done because an estimation of τ_r showed that the time needed to flush the reactor superposes the specific relaxation time of the LSC thin films in said temperature range. The sample therefore acts as a fast-responding oxygen sensor and hence, the only parameter, apart from the equilibrium conductivity, that can be derived from these transient profiles is the flush time. The normalized profiles were generated as described in subsection 3.4.1. The raw data of each conductivity relaxation experiment that was conducted in the temperature range between 267 °C and 466 °C can be found in the appendix (see Appendix C). Figure 4.15 shows six examples of fitted nor-

malized relaxation profiles of a 40 nm LSC|LAO thin film at different temperatures. The oxygen partial pressure was switched between 0.1 bar and 0.075 bar in all instances. Figure 4.15a,c,e show pO_2 switches in reducing direction, Figure 4.15b,d,f in oxidizing direction.

Following the initial ascent, σ_{norm} fluctuates considerably for all normalized profiles in Figure 4.15. Since it is assumed that the sample acts as an oxygen sensor, which means that the sample and the surrounding atmosphere are in equilibrium during the whole experiment, the fluctuation in σ can be attributed to slight changes in the supplied oxygen. The variations in σ appear in the fifth and sixth significant figures. In case of Figure 4.15c the σ values close to the feature in the first third of the transient response are scattered around 2089.8 S/cm and σ_∞ is 2089.1 S/cm, which translates to a relative change in oxygen content in the gas stream of only 0.03 %. The relative change in σ apart from the feature is even less. Figure 4.15a,f also show deviations from the postulated continuous ideally stirred tank behavior of the reactor (see subsection 3.4.1), that results in Equation (3.17). These deviations affect the quality of the fit and cause τ_f to scatter at each temperature for all LSC thin films. The reason for the slight fluctuations of the supplied oxygen and therefore an explanation for the observed deviations from the ideal model of the reactor might be connected to the fluid dynamics of the reactor. However, since the objective was to estimate τ_f in order to evaluate k_{chem} at lower temperatures, the specific characteristics of the reactor were not investigated. To estimate τ_f, the fit needs to match the initial increase of the normalized conductivity profile sufficiently well. Figure 4.15 shows that, apart from Figure 4.15a,c, Equation (3.17) can satisfy this requirement. Generally, comparing average values of the fitted flush times for different LSC thin films in the same temperature range showed that the values were fairly similar, which justified the approach. The experiment, which is shown in Figure 4.15e, was started directly after the thin film had already been measured at 462 °C. This caused the electrical contacts to degrade and explains the outliers that appear in Figure 4.15e. The fit was accepted since the majority of the σ values are fitted sufficiently well.

The fitting results for τ_f for all LSC thin films are shown in Figure 4.16. The value of the fitted flush time for each oxygen partial pressure step is plotted against the logarithm of the oxygen partial pressure. The value of the pO_2 corresponds to the final oxygen partial pressure following a pO_2 switch, e.g. if the oxygen partial pressure is switched between 0.2 bar and 0.15 bar in reducing direction, the fitted value of τ_f is plotted against the logarithm of the latter. Experiments, that were done at the same furnace set temperature, were grouped and plotted together in one figure.

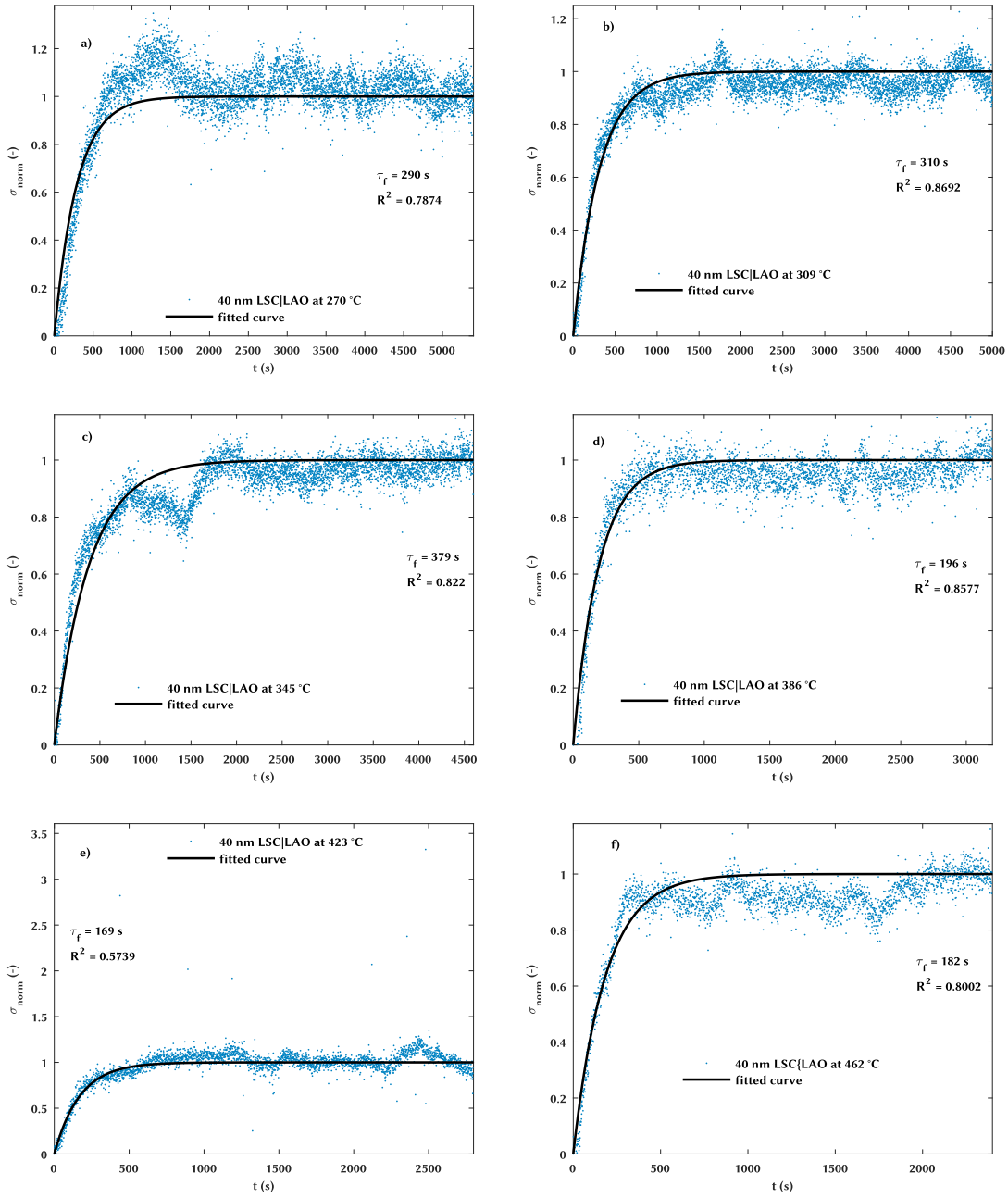

Figure 4.15.: Relaxation profiles of a 40 nm LSC|LAO thin film at different temperatures. The profiles are fitted to Equation (3.17). **a), c) and e)** show oxygen partial pressure switches in reducing direction between 0.10 bar and 0.075 bar. **b), d) and f)** show oxygen partial pressure switches between the same pO_2 values but in oxidizing direction.

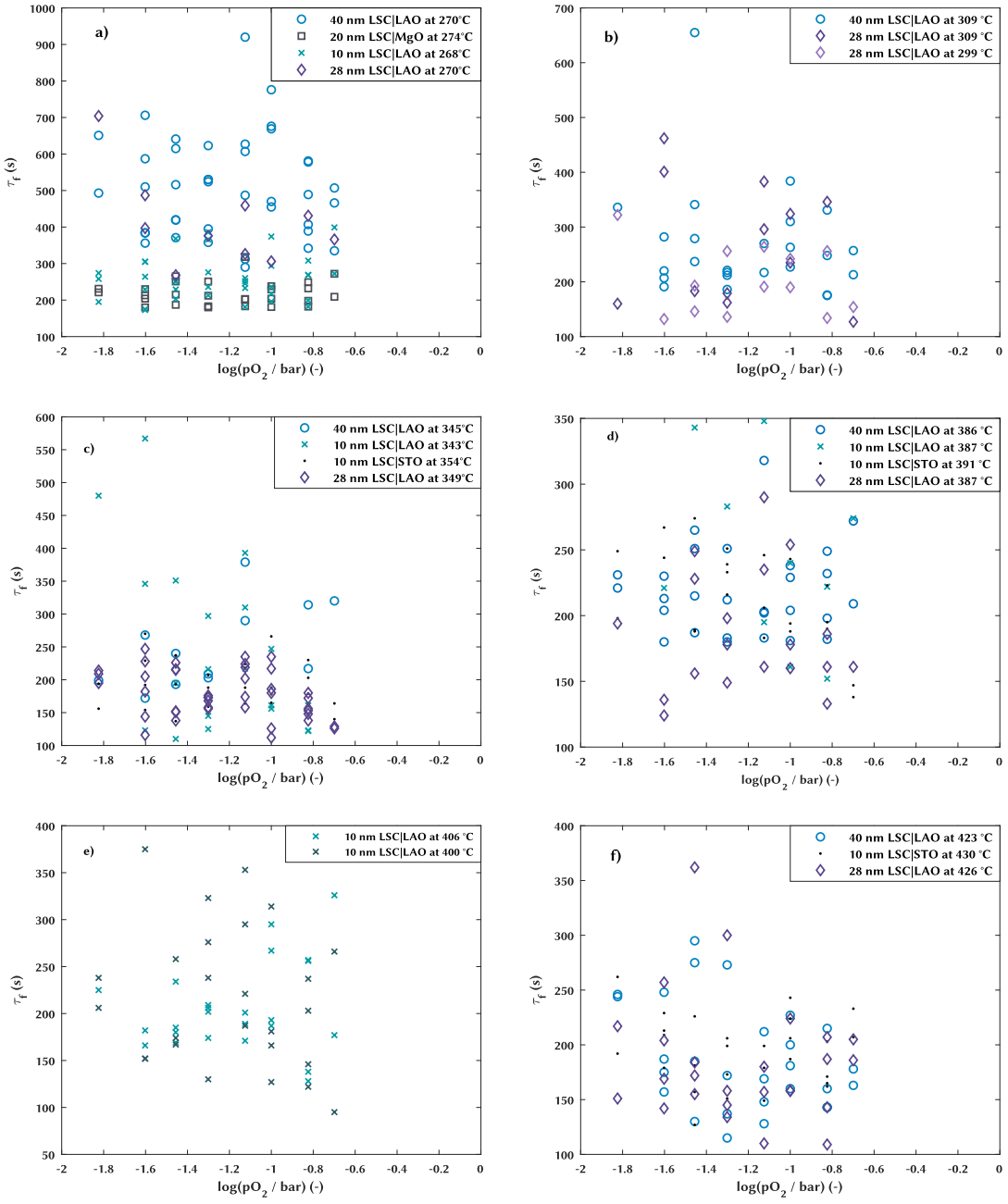

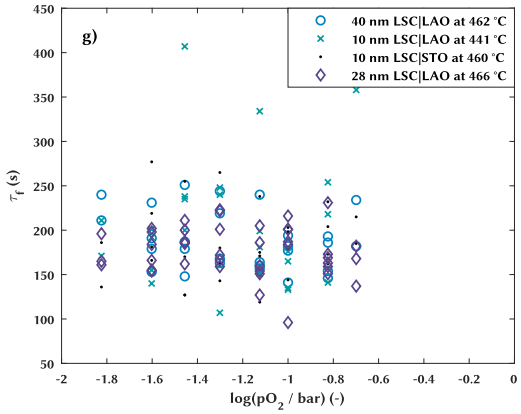

Figure 4.16.: Fitted τ_f values vs. logarithm of the surrounding pO_2 of LSC thin films at different temperatures. Results are grouped and plotted according to the furnace set temperature.

The fitted values of τ_f are scattered for all LSC thin films. This can be attributed, as already mentioned earlier, to normalized conductivity profiles that show deviations from the continuous ideally stirred tank behavior of the reactor. At lower temperatures (see Figure 4.16a-Figure 4.16c) the scatter in τ_f is more pronounced. At higher temperatures the range of the fitted τ_f values becomes more narrow (see Figure 4.16d - Figure 4.16g). Generally, no pO_2 dependence of τ_f is recognizable in these fitting results.

Otter et al. described τ_f as follows [63]:

$$\tau_f = \frac{V_r}{\Phi_{v,tot}} \cdot \frac{T_{STP}}{T_r}. \tag{4.7}$$

V_r, $\Phi_{r,tot}$, T_{STP}, T_r denote the reactor volume, the gas flow rate, room temperature and the temperature inside the reactor, respectively. According to Equation (4.7) τ_f should show little temperature dependence.

Table 4.5 presents the average value of τ_f for each plot of Figure 4.16. The tables containing the numerical values of τ_f for each plot of Figure 4.16 can be found in the appendix (see Appendix A). First, the fitted τ_f values were averaged for each LSC thin film. The average flush time values that were derived for the LSC thin films in Figure 4.16a,b,c exhibited a larger variation amongst each other than the average τ_f values that were obtained for Figure 4.16d - Figure 4.16g. In a subsequent step the mean of these average values was taken for each group

Table 4.5.: Average values of τ_f for each plot in Figure 4.16.

	$\varnothing\tau_f$ (s)
Figure 4.16a	350
Figure 4.16b	246
Figure 4.16c	216
Figure 4.16d	204
Figure 4.16e	210
Figure 4.16f	188
Figure 4.16g	189

of LSC thin films. The average of τ_f decreases with increasing temperature except for the thin films shown in Figure 4.16e and Figure 4.16g. However, the temperature dependence of the average τ_f values is small for Figure 4.16c - Figure 4.16g as presumed by Equation (4.7).

To ensure that τ_f is also independent of the direction in which the pO_2 was switched, τ_f was again plotted against the logarithm of the surrounding oxygen partial pressure, but the points were labeled according to the direction. The results are shown in Figure 4.17, a) -g) correspond to Figure 4.16a - Figure 4.16g.

The fitted τ_f values are randomly scattered independent of the direction in which the oxygen partial pressure step is applied. This observation holds for all measured LSC thin films. As τ_f shows neither a dependence on pO_2 nor on the direction in which the pO_2 is switched and additionally shows only a small temperature dependence, it is valid to employ a single τ_f value for the estimation of k_{chem}.

Since the scatter in the fitted τ_f values in Figure 4.16g is, except for a few outliers, concentrated around approximately 200 s, the average τ_f value of 189 s of these LSC thin films was taken to subsequently estimate the surface exchange coefficient of the LSC thin films at lower temperatures.

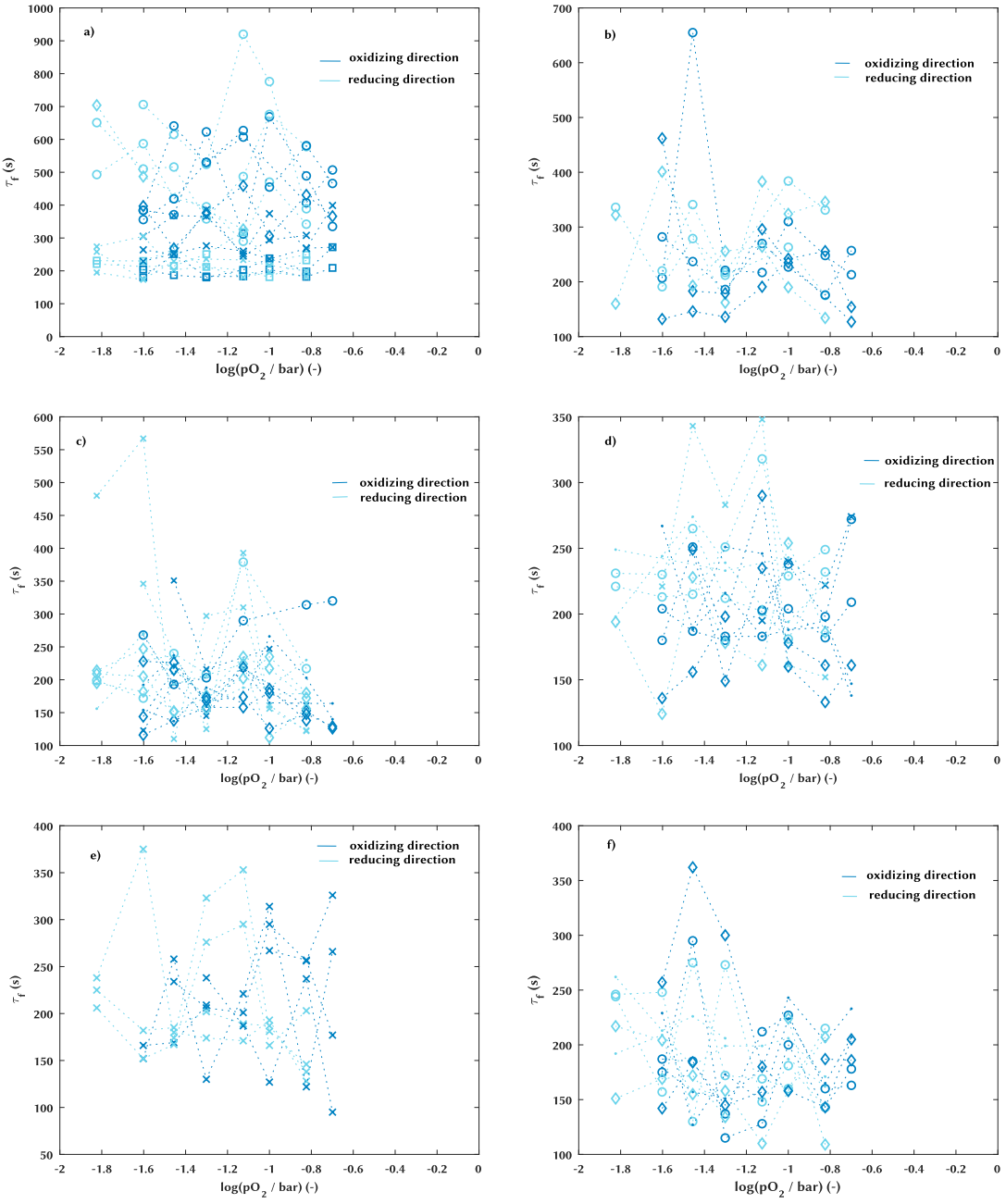

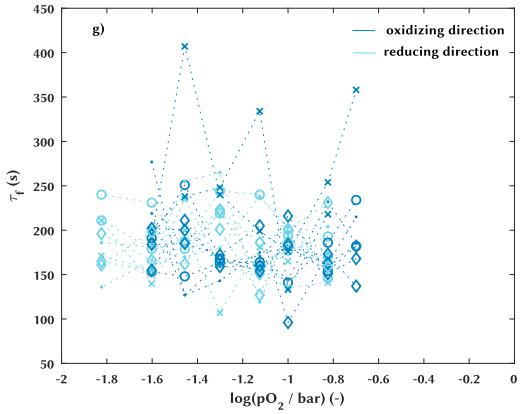

Figure 4.17.: τ_f values vs. logarithm of the surrounding pO_2 of LSC thin films at different temperatures. Fitted τ_f values are marked according to the direction in which the pO_2 was changed. **a) - g)** correspond to Figure 4.16a - Figure 4.16g. The dotted lines are inserted to guide the eye.

4.4.2. Estimation of the surface exchange coefficient at low temperatures

The surface exchange coefficient k_{chem} of a 10 nm LSC|LAO, 10 nm LSC|STO and 20 nm LSC|MgO thin film was evaluated in the temperature range between 144 °C and 204 °C. All relaxation profiles in the aforementioned temperature range were fitted to Equation (3.18) in order to obtain τ. Subtracting the flush time of the reactor τ_f from τ resulted in the value of the specific relaxation time τ_r (see Equation (3.19)). The estimation of the flush time is described in subsection 4.4.1.

The conductivity in all experiments between 144 °C and 204 °C exhibited a drift that spanned over the whole measurement. Before fitting the relaxation profiles to Equation (3.18), the measured relaxation data had to be drift corrected as described in section 3.5. The calculation of the relative change of the oxygen content in relation to the film thickness Δd for each pO_2 switch is also described in section 3.5. The obtained results from these calculations are presented in Appendix B for all measured thin films. The surface exchange coefficient is calculated using Equation (3.10).

a) LSC|STO

Figure 4.18a) shows a conductivity relaxation experiment of a 10 nm LSC|STO thin film, which was conducted at 146 °C. The conductivity is plotted against the time. In addition to the measured data, the drift corrected data is plotted in Figure 4.18b).

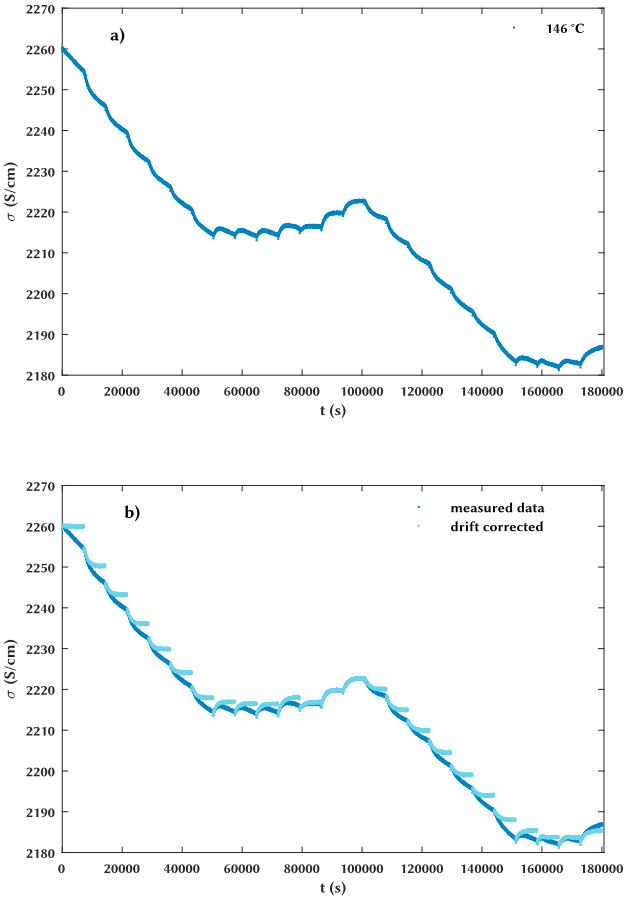

Figure 4.18.: 10 nm LSC|STO thin film measured at 146 °C. **a)** shows σ as a function of time. The conductivity is drifting over the span of the measurement. In **b)** the drift corrected data is shown. Evaluated pO_2 steps are shown in Table 4.6. The initial pO_2 was 0.15 bar.

The single oxygen partial pressure switches are distinguishable in both reducing and oxidizing direction. However, the measured conductivity values are shifting towards lower values throughout the whole measurement and only in case of the pO_2 steps 13 and 14 it seems that the sample reached an equilibrium state with the surrounding atmosphere in the given 7200 s after the oxygen partial pressure had been switched (see Figure 4.18b)).

Figure 4.19 shows two normalized relaxation profiles of the experiment shown in Figure 4.18. The pO_2 was switched between 0.15 bar and 0.1 bar in reducing and oxidizing direction. Both profiles were calculated using drift corrected data of the correspondent pO_2 steps. In contrast to Figure 4.19a), the ascent of σ_{norm} in Figure 4.19b) is broadened. This behavior stems from a smaller relative change in conductivity, σ_∞ was only 0.05 % higher compared to starting value σ_0, which therefore compresses the profile.

Both normalized profiles exhibit a gradual increase within the first 1000 s, which is assumed to be caused by the flush time of the reactor. As already mentioned at the beginning of this subsection, the normalized profiles were fitted to Equation (3.18). Since the fitting process yields τ, the sum of τ_r and τ_f, the gradual initial increase of the normalized profiles isn't represented by Equation (3.18) and as a result, the fitted curves show stronger deviations from the data in this region.

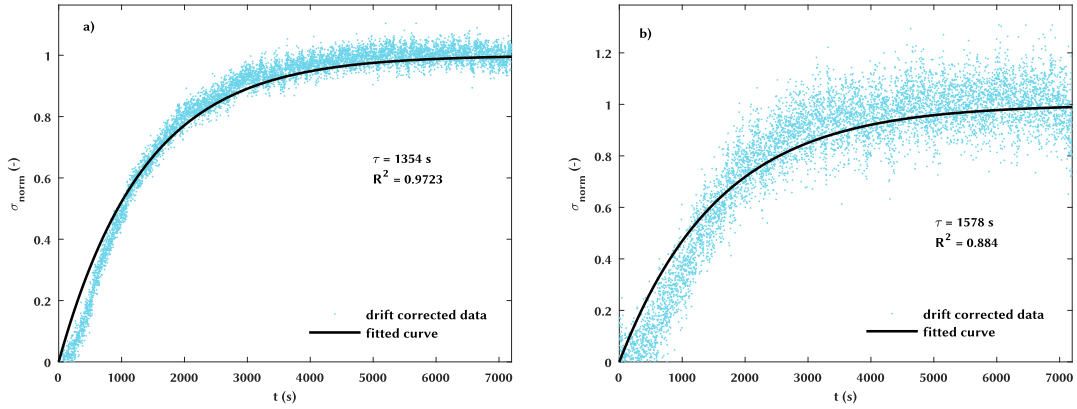

Figure 4.19.: 10 nm LSC|STO thin film at 146 °C. **a)** Normalized relaxation profile of an oxygen partial pressure switch in reducing direction between 0.15 bar and 0.1 bar. **b)** Normalized relaxation profile of an oxygen partial pressure switch in oxidizing direction between 0.1 bar and 0.15 bar. Both profiles in **a)** and **b)** were calculated using drift corrected data.

The fitting results of the experiment shown in Figure 4.18 as well as the results for τ_r, the estimation of Δd and k_{chem} are presented in Table 4.6. Additionally, the change in oxygen content in respect to the film thickness is converted into a change of oxygen atoms related to the area of the sample, ΔO, and also presented in Table 4.6.

Fitting the drift corrected relaxation profiles to Equation (3.18) yielded τ values that reside in a similar range around 1300 s. τ_r is, apart from three exceptions, greater than 1000 s. The estimation of the change of oxygen content in respect to the film thickness, Δd, produced values in the range of $10^{-10} cm$.

For the calculation of ΔO the lattice parameter of the LSC thin films is assumed to be $a = 0.3830$ nm [32]. Three oxygen atoms are therefore present in $5.62 \cdot 10^{-23} cm^3$, which translates to one oxygen atom in $1.87 \cdot 10^{-23} cm^3$. Hence, a total amount of $5.34 \cdot 10^{22}$ oxygen atoms per cubic centimeter is present in the LSC thin films and this corresponds to a total oxygen concentration, c, of $8.87 \cdot 10^{-2} mol/cm^3$. The change in oxygen atoms related to the sample area for each oxygen partial pressure step is therefore

$$\Delta O \approx \Delta d \cdot c \cdot N_A, \tag{4.8}$$

with N_A denoting the Avogadro constant. ΔO of the 10 nm LSC|STO thin film is in the range of $10^{13} atoms/cm^2$ (see Table 4.6), which is remarkable considering that the measurement was conducted at 146 °C. In this context the detection limit of the measurement technique shall be briefly discussed. For the measurements of the 10 nm LSC|STO, 10 nm LSC|LAO and 20 nm LSC|MgO thin films at temperatures above 300 °C the drift in the obtained relaxation data was less pronounced (see Appendix C) and thus, the estimation of the detection limit is based on these experiments. Specifically, the assessment is based on the detectable change in σ in the part of the relaxation profile after the initial increase or decrease of σ is completed ($\widehat{=}$ close to the new equilibrium state). Taking the noise in the recorded data into account, it is still possible to distinguish changes in σ in the first decimal place. Following the calculation of Δd in subsection 3.4.2, Equation (4.8), on average, yields ΔO values in the range of $2 \cdot 10^{12} atoms/cm^2 - 5 \cdot 10^{12} atoms/cm^2$. Thus, a change in oxygen atoms per sample area below this range can't be detected. As a comparison of how small this detection limit is we can compare it to the typical number of surface atoms of a solid, which is about $10^{15} atoms/cm^2$. That means we can detect changes less than 1 % of a monolayer of oxygen, which is evenly distributed in the whole thin film.

Table 4.6.: Results of fitting relaxation profiles from Figure 4.18 to Equation (3.18). τ_r was calculated by subtracting the reactor flush time from the fitted value of τ. The relative change in oxygen content with respect to the film thickness Δd for each oxygen partial pressure step is given, which, in addition, is converted to a change in oxygen atoms related to the sample area ΔO. The calculated k_{chem} values are presented.

pO_2 (bar)	τ (s)	τ_r (s)	Δd (cm)	$\Delta O \left(\frac{atoms}{cm^2}\right)$	k_{chem} (cm/s)
0.1	1354	1165	$3.74 \cdot 10^{-10}$	$2.00 \cdot 10^{13}$	$3.21 \cdot 10^{-13}$
0.075	1205	1016	$2.30 \cdot 10^{-10}$	$1.23 \cdot 10^{13}$	$2.26 \cdot 10^{-13}$
0.05	1313	1124	$2.82 \cdot 10^{-10}$	$1.50 \cdot 10^{13}$	$2.50 \cdot 10^{-13}$
0.035	1194	1005	$2.25 \cdot 10^{-10}$	$1.20 \cdot 10^{13}$	$2.24 \cdot 10^{-13}$
0.025	1225	1036	$1.74 \cdot 10^{-10}$	$9.27 \cdot 10^{12}$	$1.68 \cdot 10^{-13}$
0.015	1221	1032	$2.21 \cdot 10^{-10}$	$1.18 \cdot 10^{13}$	$2.14 \cdot 10^{-13}$
0.025	1078	889	$2.33 \cdot 10^{-10}$	$1.25 \cdot 10^{13}$	$2.63 \cdot 10^{-13}$
0.035	1107	918	$1.84 \cdot 10^{-10}$	$9.83 \cdot 10^{12}$	$2.01 \cdot 10^{-13}$
0.05	1191	1002	$2.20 \cdot 10^{-10}$	$1.18 \cdot 10^{13}$	$2.20 \cdot 10^{-13}$
0.075	1398	1209	$3.44 \cdot 10^{-10}$	$1.84 \cdot 10^{13}$	$2.84 \cdot 10^{-13}$
0.1	1578	1389	$1.09 \cdot 10^{-10}$	$5.83 \cdot 10^{12}$	$7.86 \cdot 10^{-14}$
0.15	1268	1079	$3.14 \cdot 10^{-10}$	$1.68 \cdot 10^{13}$	$2.91 \cdot 10^{-13}$
0.2	1414	1225	$2.72 \cdot 10^{-10}$	$1.45 \cdot 10^{13}$	$2.22 \cdot 10^{-13}$
0.15	1468	1279	$2.27 \cdot 10^{-10}$	$1.21 \cdot 10^{13}$	$1.78 \cdot 10^{-13}$
0.1	1472	1283	$2.85 \cdot 10^{-10}$	$1.52 \cdot 10^{13}$	$2.22 \cdot 10^{-13}$
0.075	1637	1448	$1.93 \cdot 10^{-10}$	$1.03 \cdot 10^{13}$	$1.33 \cdot 10^{-13}$
0.05	1464	1275	$2.56 \cdot 10^{-10}$	$1.37 \cdot 10^{13}$	$2.01 \cdot 10^{-13}$
0.035	1466	1277	$1.92 \cdot 10^{-10}$	$1.03 \cdot 10^{13}$	$1.51 \cdot 10^{-13}$
0.025	1219	1030	$1.43 \cdot 10^{-10}$	$7.62 \cdot 10^{12}$	$1.38 \cdot 10^{-13}$
0.015	1493	1304	$1.96 \cdot 10^{-10}$	$1.04 \cdot 10^{13}$	$1.50 \cdot 10^{-13}$
0.025	1557	1368	$1.87 \cdot 10^{-10}$	$9.97 \cdot 10^{12}$	$1.36 \cdot 10^{-13}$
0.05	930	741	$1.53 \cdot 10^{-10}$	$8.16 \cdot 10^{12}$	$2.06 \cdot 10^{-13}$
0.075	1570	1381	$2.38 \cdot 10^{-10}$	$1.27 \cdot 10^{13}$	$1.73 \cdot 10^{-13}$

Since the drift is superimposed on the whole measurement, it is not valid to attribute the calculated k_{chem} values to the single oxygen partial pressure steps. The values of k_{chem} are therefore averaged and the resulting mean k_{chem} value serves as an estimation of how fast the surface exchange kinetics of the 10 nm thick LSC|STO thin film are at 146 °C independent of the oxygen partial pressure. This approach was also chosen for all other measurements in the temperature range between 144 °C - 204 °C, since all data there were superimposed by drift.

The mean k_{chem} value at 146 °C is $2.02 \cdot 10^{-13} cm/s$.

Figure 4.20a) shows the conductivity relaxation of the 10 nm LSC|STO thin film at 194 °C, in Figure 4.20b) the drift corrected data is shown in addition to the measured data. The drift is less pronounced compared to the measurement that was conducted at 146 °C, but is still superimposed over the span of the experiment with an overall negative slope. The pO_2 steps are, again, distinguishable in both reducing and oxidizing direction and since the drift is less pronounced, the drift corrected data practically coincide with the measured data. The temperature hadn't reached a constant value when the measurement was started, which explains the increase of σ in the first three pO_2 steps. Consequently, the first four pO_2 steps were disregarded for the evaluation of τ.

In Figure 4.21 two drift corrected, normalized relaxation profiles of the measurement at 194 °C are shown. The oxygen partial pressure was switched between 0.10 bar and 0.05 bar in reducing and oxidizing direction, respectively. The two example profiles are presented to illustrate how the shape of the relaxation profiles changed due to the higher temperature during the experiment. The ascent of σ_{norm} is faster compared to the measurement at 146 °C (see Figure 4.19), showing that the relaxation process is accelerated as a result of the higher temperature. Additionally, the visible influence of the reactor flush time on the normalized relaxation profile is diminished for the same reason. In Figure 4.21a) the gradual increase of σ_{norm} can still be identified whereas in Figure 4.21b) the gradual increase is already compressed and can only be suspected. Deviations of the fitted curve are, again, mainly observed at the initial increase of σ_{norm}.

Since all calculations were carried out with the same τ_f value (τ_f =189 s) the presumption of $\tau_f < \tau_r$ is still satisfied at 194 °C as the values of the overall time constant are scattered around 640 s (see Table 4.7). Obviously, this approach constitutes an oversimplification of the reality, since τ_f will probably be slightly higher at 194 °C than the experimentally derived τ_f value. Assuming that τ_r approaches τ_f at 194 °C ($\tau_f \approx \tau_r$), yields k_{chem} values, that exceed the values shown in Table 4.7 by approximately a factor of 2.

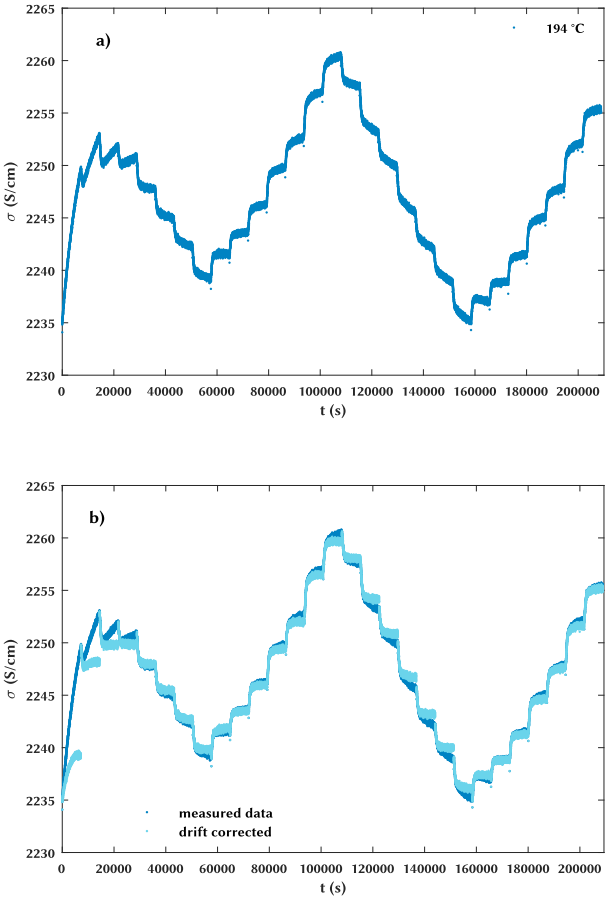

Figure 4.20.: 10 nm LSC|STO thin film measured at 194 °C. **a)** shows σ as a function of time. The conductivity is drifting over the span of the measurement. In **b)** the drift corrected data is shown. Evaluated pO_2 steps are shown in Table 4.7. The experiment was started at an initial pO_2 of 0.2 bar.

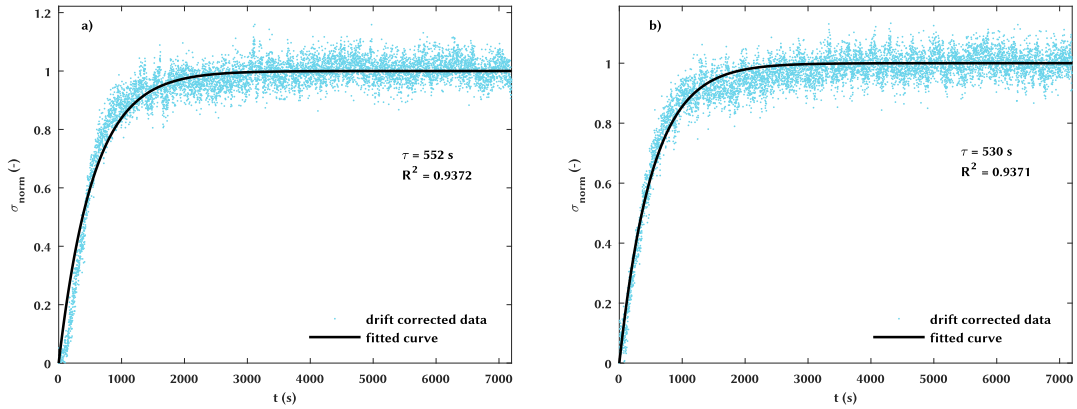

Figure 4.21.: 10 nm LSC|STO thin film measured at 194 °C. **a)** σ_{norm} is plotted against the time. The pO_2 is switched between 0.075 bar and 0.05 bar in reducing direction. **b)** The oxygen partial pressure step in oxidizing direction between 0.035 bar and 0.05 bar is shown. Both profiles were fitted to Equation (3.18). The influence of τ_f is reduced in each instance due to the higher temperature.

The results of fitting the relaxation data to Equation (3.18) are shown in Table 4.7. The specific relaxation time, τ_r, is scattered around 450 s. Again, the oxygen content changes in the range of $10^{-10} cm$ in relation to the film thickness for all evaluated pO_2 steps and the change in oxygen atoms related to sample area is approximately $10^{13} atoms/cm^2$. Averaging the calculated k_{chem} values yields a mean k_{chem} value of $5.34 \cdot 10^{-13} cm/s$.

In Figure 4.22a) the conductivity relaxation experiment of the 10 nm LSC|STO thin film at 204 °C is shown. Compared to the experiment that was conducted at 194 °C, the drift is again more pronounced with an overall negative slope. The reason for this behavior is so far unknown. In Figure 4.22b) the drift corrected data is plotted in addition to the measured data. In some instances, the drift correction wasn't sufficient enough and the pO_2 steps could not be leveled. These pO_2 steps were not evaluated as the drift corrected conductivity did not relax to a constant σ value. Table 4.8 shows which pO_2 steps were evaluated and presents the fitted values of τ as well as the corresponding τ_r values.

Overall, the fitted τ values are in the same range as the evaluated τ values at 194 °C. The values of τ are scattered around the mean value of 630 s, which is slightly lower compared to the to experiment at 194 °C and can be attributed to the slightly higher temperature. The values of the specific relaxation time are scattered around 440 s. Δd and ΔO are again in the

Table 4.7.: Results of fitting relaxation profiles from Figure 4.20 to Equation (3.18). τ_r was calculated by subtracting the reactor flush time from the fitted value of τ. The relative change in oxygen content with respect to the film thickness Δd for each oxygen partial pressure step is given, which, in addition, is converted to a change in oxygen atoms related to the sample area ΔO. The calculated k_{chem} values are presented.

pO_2 (bar)	τ (s)	τ_r (s)	Δd (cm)	$\Delta O \left(\frac{\text{atoms}}{\text{cm}^2}\right)$	k_{chem} (cm/s)
0.05	552	363	$2.40 \cdot 10^{-10}$	$1.28 \cdot 10^{13}$	$6.61 \cdot 10^{-13}$
0.035	537	348	$1.85 \cdot 10^{-10}$	$9.88 \cdot 10^{12}$	$5.32 \cdot 10^{-13}$
0.025	804	615	$1.97 \cdot 10^{-10}$	$1.05 \cdot 10^{13}$	$3.21 \cdot 10^{-13}$
0.015	646	457	$2.02 \cdot 10^{-10}$	$1.08 \cdot 10^{13}$	$4.41 \cdot 10^{-13}$
0.025	591	402	$2.50 \cdot 10^{-10}$	$1.34 \cdot 10^{13}$	$6.23 \cdot 10^{-13}$
0.035	502	313	$1.95 \cdot 10^{-10}$	$1.04 \cdot 10^{13}$	$6.23 \cdot 10^{-13}$
0.05	530	341	$2.18 \cdot 10^{-10}$	$1.16 \cdot 10^{13}$	$6.39 \cdot 10^{-13}$
0.075	641	452	$2.80 \cdot 10^{-10}$	$1.49 \cdot 10^{13}$	$6.18 \cdot 10^{-13}$
0.1	579	390	$2.12 \cdot 10^{-10}$	$1.13 \cdot 10^{13}$	$5.43 \cdot 10^{-13}$
0.15	692	503	$3.47 \cdot 10^{-10}$	$1.85 \cdot 10^{13}$	$6.90 \cdot 10^{-13}$
0.2	654	465	$2.28 \cdot 10^{-10}$	$1.22 \cdot 10^{13}$	$4.91 \cdot 10^{-13}$
0.15	633	444	$1.95 \cdot 10^{-10}$	$1.04 \cdot 10^{13}$	$4.39 \cdot 10^{-13}$
0.1	640	451	$3.04 \cdot 10^{-10}$	$1.62 \cdot 10^{13}$	$6.74 \cdot 10^{-13}$
0.075	713	524	$1.91 \cdot 10^{-10}$	$1.02 \cdot 10^{13}$	$3.65 \cdot 10^{-13}$
0.05	745	556	$2.75 \cdot 10^{-10}$	$1.47 \cdot 10^{13}$	$4.95 \cdot 10^{-13}$
0.035	602	413	$1.96 \cdot 10^{-10}$	$1.04 \cdot 10^{13}$	$4.74 \cdot 10^{-13}$
0.025	686	497	$1.83 \cdot 10^{-10}$	$9.77 \cdot 10^{12}$	$3.68 \cdot 10^{-13}$
0.015	736	547	$2.41 \cdot 10^{-10}$	$1.29 \cdot 10^{13}$	$4.40 \cdot 10^{-13}$
0.025	522	333	$2.04 \cdot 10^{-10}$	$1.09 \cdot 10^{13}$	$6.13 \cdot 10^{-13}$
0.035	535	346	$1.69 \cdot 10^{-10}$	$9.02 \cdot 10^{12}$	$4.88 \cdot 10^{-13}$
0.05	534	345	$2.25 \cdot 10^{-10}$	$1.20 \cdot 10^{13}$	$6.51 \cdot 10^{-13}$
0.075	656	467	$2.85 \cdot 10^{-10}$	$1.52 \cdot 10^{13}$	$6.10 \cdot 10^{-13}$
0.1	833	644	$2.33 \cdot 10^{-10}$	$1.25 \cdot 10^{13}$	$3.62 \cdot 10^{-13}$
0.15	690	501	$3.53 \cdot 10^{-10}$	$1.89 \cdot 10^{13}$	$7.05 \cdot 10^{-13}$
0.2	746	557	$2.66 \cdot 10^{-10}$	$1.42 \cdot 10^{13}$	$4.77 \cdot 10^{-13}$

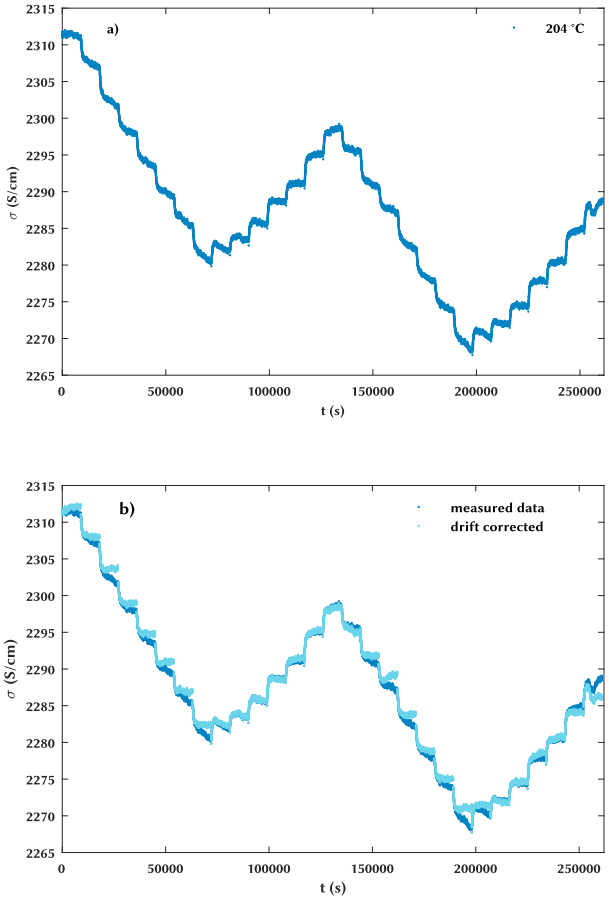

Figure 4.22.: 10 nm LSC|STO thin film measured at 204 °C. **a)** shows σ as a function of time. The conductivity is drifting over the span of the measurement. In **b)** the drift corrected data is shown. Evaluated pO_2 steps are shown in Table 4.8. The initial pO_2 of the experiment was 0.2 bar.

range of $10^{-10} cm$ and $10^{13} atoms/cm^2$, respectively. The mean k_{chem} value at 204 °C is higher by approximately a factor of 1.2 compared to the average k_{chem} value at 194 °C and amounts to $6.63 \cdot 10^{-13} cm/s$.

Table 4.8.: Results of fitting relaxation profiles from Figure 4.22 to Equation (3.18). τ_r was calculated by subtracting the reactor flush time from the fitted value of τ.The relative change in oxygen content with respect to the film thickness Δd for each oxygen partial pressure step is given, which, in addition, is converted to a change in oxygen atoms related to the sample area ΔO. The calculated k_{chem} values are presented.

pO_2 (bar)	τ (s)	τ_r (s)	Δd (cm)	$\Delta O \left(\frac{atoms}{cm^2}\right)$	k_{chem} (cm/s)
0.15	695	506	$2.49 \cdot 10^{-10}$	$1.33 \cdot 10^{13}$	$4.93 \cdot 10^{-13}$
0.1	465	276	$2.67 \cdot 10^{-10}$	$1.42 \cdot 10^{13}$	$9.67 \cdot 10^{-13}$
0.075	709	520	$2.24 \cdot 10^{-10}$	$1.19 \cdot 10^{13}$	$4.30 \cdot 10^{-13}$
0.05	639	450	$2.54 \cdot 10^{-10}$	$1.36 \cdot 10^{13}$	$5.64 \cdot 10^{-13}$
0.025	527	338	$1.98 \cdot 10^{-10}$	$1.06 \cdot 10^{13}$	$5.87 \cdot 10^{-13}$
0.015	682	493	$2.64 \cdot 10^{-10}$	$1.41 \cdot 10^{13}$	$5.36 \cdot 10^{-13}$
0.075	412	223	$2.56 \cdot 10^{-10}$	$1.37 \cdot 10^{13}$	$1.15 \cdot 10^{-12}$
0.15	725	536	$3.73 \cdot 10^{-10}$	$1.99 \cdot 10^{13}$	$6.96 \cdot 10^{-13}$
0.2	717	528	$2.88 \cdot 10^{-10}$	$1.54 \cdot 10^{13}$	$5.46 \cdot 10^{-13}$
0.1	634	445	$3.15 \cdot 10^{-10}$	$1.68 \cdot 10^{13}$	$7.08 \cdot 10^{-13}$
0.05	574	385	$2.81 \cdot 10^{-10}$	$1.50 \cdot 10^{13}$	$7.30 \cdot 10^{-13}$
0.035	804	615	$2.94 \cdot 10^{-10}$	$1.57 \cdot 10^{13}$	$4.78 \cdot 10^{-13}$
0.025	733	544	$2.20 \cdot 10^{-10}$	$1.18 \cdot 10^{13}$	$4.05 \cdot 10^{-13}$
0.015	411	222	$2.32 \cdot 10^{-10}$	$1.24 \cdot 10^{13}$	$1.04 \cdot 10^{-12}$
0.025	574	385	$2.57 \cdot 10^{-10}$	$1.37 \cdot 10^{13}$	$6.68 \cdot 10^{-13}$
0.05	533	344	$2.18 \cdot 10^{-10}$	$1.16 \cdot 10^{13}$	$6.34 \cdot 10^{-13}$
0.075	972	783	$3.77 \cdot 10^{-10}$	$2.01 \cdot 10^{13}$	$4.81 \cdot 10^{-13}$
0.1	738	549	$2.73 \cdot 10^{-10}$	$1.46 \cdot 10^{13}$	$4.96 \cdot 10^{-13}$
0.15	482	293	$2.87 \cdot 10^{-10}$	$1.53 \cdot 10^{13}$	$9.80 \cdot 10^{-13}$

One might notice, that no example fits of the drift corrected relaxation profiles were given for the measurement at 204 °C. The normalized profiles are similar to the profiles that were obtained for the measurement at 194 °C since only 10 °C separate the two measurements. A discussion of the observed effects was already given above and since the profiles of the experiment at 204 °C could not offer additional information beyond that, only the fitted values of τ are given in Table 4.8.

b) LSC|LAO

In Figure 4.23a) the conductivity of a 10 nm thick LSC|LAO thin film at 144 °C is plotted against the time. The relaxation behavior differs from the behavior of the 10 nm LSC|STO thin film, that was already discussed above. Oxygen partial pressure steps are only distinguishable in the first third of the measurement. In the remaining two thirds, σ is still changing due to the applied pO_2 steps but the change in σ for each oxygen partial pressure step is too small, which ultimately prevents the evaluation of these steps. Figure 4.23b) shows the drift corrected data of the experiment shown in Figure 4.23a). The temperature had not reached a constant value when the experiment was started, which explains the decrease of σ in the beginning of the measurement. Hence, the first two pO_2 steps weren't evaluated.

Figure 4.24 shows a example fit for the measurement that was carried out at 144 °C. The oxygen partial pressure was switched between 0.10 bar and 0.075 bar in reducing direction. As for the 10 nm LSC|STO thin film at 146 °C, σ_{norm} increases gradually in the beginning, which, as already mentioned above, can be attributed to the reactor flush time. Compared to the LSC|STO thin film, the relaxation process of the LSC|LAO thin film is slower. It seems that σ_∞ was attained in the drift corrected profiles. However, if the value of σ_∞ would have been maintained beyond the given aquisistion time of 7200 s can only be speculated. Overall, the relaxation profile barely resembles a exponential progress. As a consequence, Figure 4.24 shows that fitting the drift corrected data to Equation (3.18) yields fitted curves that, in comparison to fits that were shown for the LSC|STO thin film, differ considerably from the data.

The fitting results of the measurement at 144 °C are presented in Table 4.9. The values of σ are scattered around 2000 s. The corresponding values of τ_r are scattered around 1800 s. As for the LSC|STO thin film, the oxygen content of the LSC|LAO thin film changes in the range of $10^{-10} cm$ in relation to the film thickness. However, since the change in conductivity following a pO_2 step decreased as the experiment progressed, decreasing ΔO values were derived. The ΔO value of $5 \cdot 10^{12} atoms/cm^2$, which was evaluated for the pO_2 step between 0.025 bar and 0.015 bar, practically coincides with the above discussed detection limit. The mean k_{chem} value of the 10 nm LSC|LAO thin film is $1.09 \cdot 10^{-13} cm/s$, which is lower by approximately a factor of 0.5 compared to the average k_{chem} value of the 10 nm LSC|STO thin film at 146 °C.

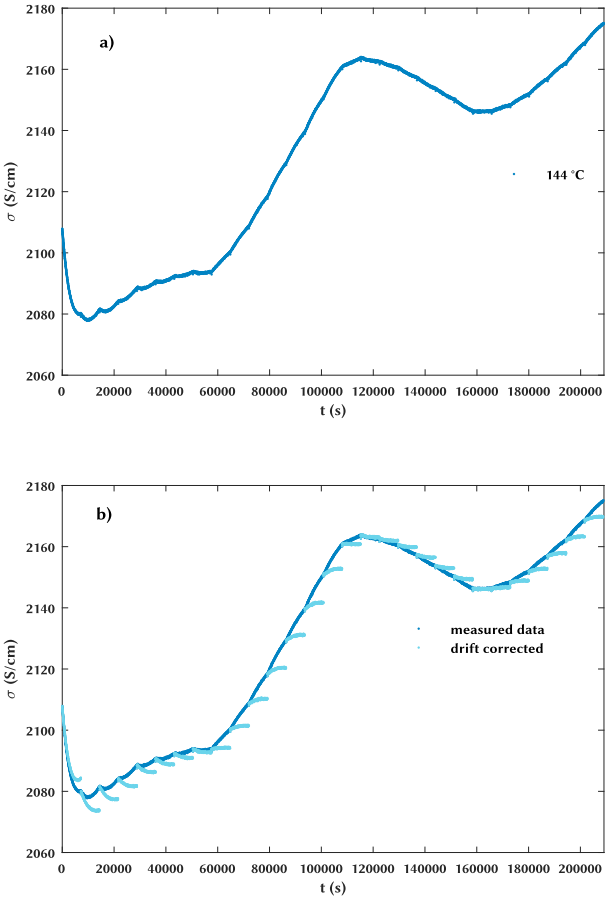

Figure 4.23.: 10 nm LSC|LAO thin film measured at 144 °C. **a)** shows σ as a function of time. The conductivity is drifting over the span of the measurement. In **b)** the drift corrected data is shown. Evaluated pO_2 steps are shown in Table 4.9. The initial pO_2 of the experiment was 0.2 bar.

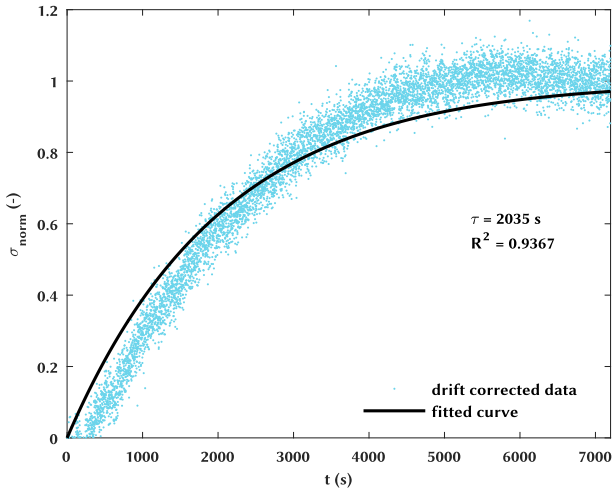

Figure 4.24.: 10 nm LSC|LAO thin film at 144 °C. σ_{norm} is plotted against the time. The pO_2 was switched between 0.1 bar and 0.075 bar in reducing direction. Compared to the LSC|STO thin film at 146 °C, the relaxation behavior is slower, which leads to deviations of the fitted curve from the normalized profile.

Table 4.9.: Results of fitting relaxation profiles from Figure 4.23 to Equation (3.18). τ_r was calculated by subtracting the reactor flush time from the fitted value of τ.The relative change in oxygen content with respect to the film thickness Δd for each oxygen partial pressure step is given, which, in addition, is converted to a change in oxygen atoms related to the sample area ΔO. The calculated k_{chem} values are presented.

pO_2 (bar)	τ (s)	τ_r (s)	Δd (cm)	$\Delta O \left(\frac{atoms}{cm^2}\right)$	k_{chem} (cm/s)
0.1	2001	1812	$3.73 \cdot 10^{-10}$	$1.99 \cdot 10^{13}$	$2.06 \cdot 10^{-13}$
0.075	2035	1846	$2.28 \cdot 10^{-10}$	$1.22 \cdot 10^{13}$	$1.23 \cdot 10^{-13}$
0.05	1940	1751	$2.02 \cdot 10^{-10}$	$1.08 \cdot 10^{13}$	$1.15 \cdot 10^{-13}$
0.035	1967	1778	$1.54 \cdot 10^{-10}$	$8.24 \cdot 10^{12}$	$8.68 \cdot 10^{-14}$
0.025	2063	1874	$1.26 \cdot 10^{-10}$	$6.73 \cdot 10^{12}$	$6.72 \cdot 10^{-14}$
0.015	1838	1649	$9.41 \cdot 10^{-11}$	$5.03 \cdot 10^{12}$	$5.71 \cdot 10^{-14}$

c) LSC|MgO

The surface exchange coefficient was also estimated for a 20 nm thick LSC|MgO thin film at 144 °C. Figure 4.25a) shows the measured conductivity, which exhibited a drift with an overall positive slope, plotted against the time. The drift corrected oxygen partial pressure steps are shown in addition to the measured data in Figure 4.25b). The characteristics of this measurement are similar to the experiment of the 10 nm LSC|LAO thin film, which was discussed above. The pO_2 steps are distinguishable in the first third of the measurement. However, in contrast to the measurement of the LSC|LAO thin film, also three pO_2 steps from the first oxidizing run could be evaluated. The first three pO_2 steps at the beginning of the measurement weren't considered in the evaluation since the temperature had not reached a constant value.

Figure 4.26 shows a drift corrected relaxation profile of the LSC|MgO thin film at 144 °C. The pO_2 step was applied in oxidizing direction between 0.075 bar and 0.1 bar. The profile shows great similarities with the example relaxation profile of the LSC|LAO thin film at 144 °C. The influence of the reactor flush time is, again, apparent at the initial ascent of σ_{norm}. Pronounced deviations of the fitted curve from the normalized profile are also observed in this instance since the relaxation behavior of the LSC|MgO thin film also deviates from the ideal exponential progression. Consequently, fitting the drift corrected data of the LSC|MgO thin film to Equation (3.18) yields results for τ that are comparable to the results, that were obtained for the LSC|LAO thin film. The fitting results as well as the calculated τ values are summarized in Table 4.10. As for the LSC|STO and the LSC|LAO thin film, the oxygen content was estimated to change in the range of $10^{-10} cm$ in relation to the film thickness. The corresponding change in oxygen atoms related to the sample area is in the range of $10^{13} atoms/cm^2$. Averaging the calculated k_{chem} values resulted in a mean k_{chem} value of $1.44 \cdot 10^{-13} cm/s$, which is, compared to mean surface exchange coefficient of the LSC|STO thin film, lower by approximately a factor of 0.3.

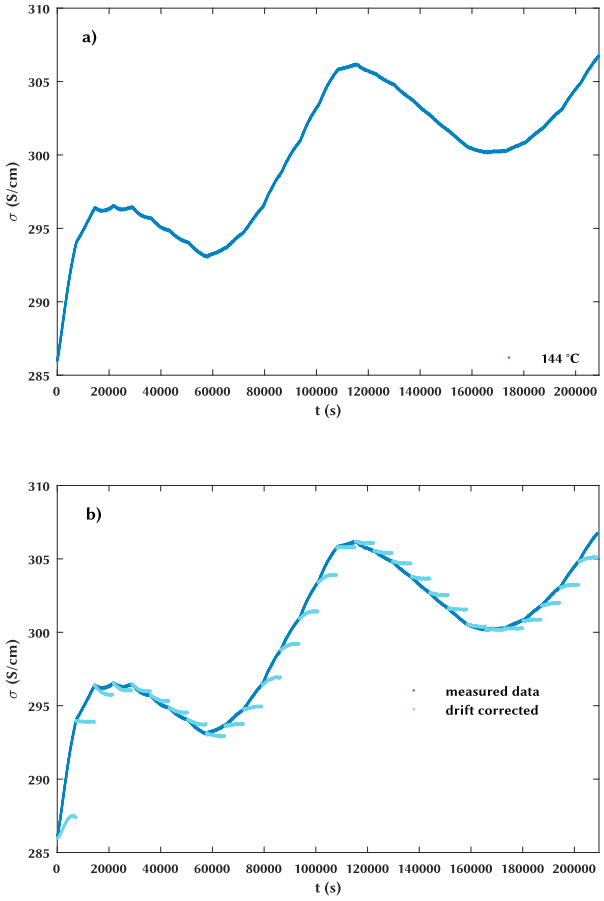

Figure 4.25.: 20 nm LSC|MgO thin film measured at 144 °C. **a)** shows σ as a function of time. The conductivity is drifting over the span of the measurement. In **b)** the drift corrected data is shown. Evaluated pO_2 steps are shown in Table 4.10. The experiment was started at an initial pO_2 of 0.2 bar.

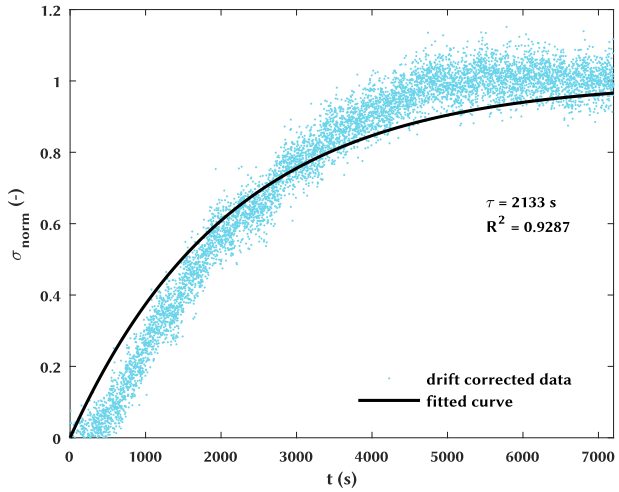

Figure 4.26.: 20 nm LSC|MgO thin film at 144 °C. σ_{norm} is plotted against the time. The pO_2 was switched between 0.1 bar and 0.075 bar in oxidizing direction. Compared to the LSC|STO thin film at 146 °C, the relaxation behavior is slower, which leads to deviations of the fitted curve from the normalized profile.

Table 4.10.: Results of fitting relaxation profiles from Figure 4.25 to Equation (3.18). τ_r was calculated by subtracting the reactor flush time from the fitted value of τ. The relative change in oxygen content with respect to the film thickness Δd for each oxygen partial pressure step is given, which, in addition, is converted to a change in oxygen atoms related to the sample area ΔO. The calculated k_{chem} values are presented.

pO_2 (bar)	τ (s)	τ_r (s)	Δd (cm)	$\Delta O \left(\frac{\text{atoms}}{\text{cm}^2}\right)$	k_{chem} (cm/s)
0.075	2029	1840	$3.08 \cdot 10^{-10}$	$1.65 \cdot 10^{13}$	$1.68 \cdot 10^{-13}$
0.05	2172	1983	$3.00 \cdot 10^{-10}$	$1.60 \cdot 10^{13}$	$1.51 \cdot 10^{-13}$
0.035	2223	2034	$2.54 \cdot 10^{-10}$	$1.35 \cdot 10^{13}$	$1.25 \cdot 10^{-13}$
0.025	2329	2140	$2.09 \cdot 10^{-10}$	$1.12 \cdot 10^{13}$	$9.79 \cdot 10^{-14}$
0.015	2140	1951	$2.12 \cdot 10^{-10}$	$1.13 \cdot 10^{13}$	$1.09 \cdot 10^{-13}$
0.1	2133	1944	$2.76 \cdot 10^{-10}$	$1.47 \cdot 10^{13}$	$1.42 \cdot 10^{-13}$
0.15	2008	1819	$3.20 \cdot 10^{-10}$	$1.71 \cdot 10^{13}$	$1.76 \cdot 10^{-13}$
0.2	2042	1853	$3.34 \cdot 10^{-10}$	$1.79 \cdot 10^{13}$	$1.80 \cdot 10^{-13}$

d) Discussion

The results of estimating the surface exchange coefficient at lower temperatures are summarized in Table 4.11. All k_{chem} values were obtained in the range of $10^{-13} cm/s$. Comparing the mean k_{chem} values at 144 °C and 146 °C, respectively, in connection to the thin film's substrate shows that, even though the highest value was obtained for the 10 nm LSC|STO thin film, the values are fairly similar. However, it is noted that the level of uncertainty for the k_{chem} values of the LSC|LAO and the LSC|MgO thin films is presumably higher since the relaxation behavior wasn't represented satisfactorily by Equation (3.18). Furthermore, it should be pointed out that the evaluation and thus, also the order of magnitude of the estimated k_{chem} values highly depend on the performed drift correction. The drift correction focuses merely on the faster time constant, which results from the oxygen exchange, thereby neglecting the slower relaxation process ($\widehat{=}$ drift) entirely, which superposed each measurement in considered the temperature range between 144 °C and 204 °C. Often similar drift phenomena are caused by the sample stochiometry not being in equilibrium with the set temperature or pO_2. Here, for oxygen, this is clearly not the case, as such an equillibration would occur with the time constant of oxygen exchange, which is much faster than the drift's time constant. On the other hand, cations are considered to be too immobile at temperatures below 200 °C, which is why it seems unlikely that cationic defects are responsible for the drift. However, as already mentioned in section 3.5, phase instabilities of LSC at these low temperatures might be a possible explanation for the observed drift in the data. That is, in a multi-phase sample phases with lower affinity towards oxygen exchange might be present. If that were the case, the approach of the drift correction would ultimately not be valid as it would lead to erroneous values for the surface exchange coefficient. So far, however, the origin of drift has not been determined and thus, the drift correction was used as it allowed for a preliminary assessment of the thin film's surface exchange coefficient.

Table 4.11.: Summary of the derived average k_{chem} values for the LSC thin films that were measured at low temperatures.

	T (°C)	k_{chem} (cm/s)
10 nm LSC|STO	146 °C	$2.02 \cdot 10^{-13}$
	194 °C	$5.34 \cdot 10^{-13}$
	204 °C	$6.63 \cdot 10^{-13}$
10 nm LSC|LAO	144 °C	$1.09 \cdot 10^{-13}$
20 nm LSC|MgO	144 °C	$1.44 \cdot 10^{-13}$

Since three measurements at different temperatures were carried out for the 10 nm LSC|STO thin film, the temperature dependence of these obtained k_{chem} values is also examined. In Figure 4.27 the logarithm of the surface exchange coefficient is plotted against the inverse temperature. k_{chem} values from this work are compared to extrapolated literature data.

Chen et al. investigated the surface kinetics of an 500 nm $La_{0.5}Sr_{0.5}CoO_{3-\delta}$ thin film, that was deposited on (100) orientated LAO, via conductivity relaxation in the temperature range between 700 °C and 760 °C [80]. The k_{chem} values shown in Figure 4.27 were obtained by Chen et al. at an oxygen partial pressure of 0.5 atm. The results of the other two literature references were also obtained by conductivity relaxation, but for bulk $La_{0.6}Sr_{0.4}CoO_{3-\delta}$. Egger et al. investigated the oxygen exchange kinetics of LSC in the temperature range between 525 °C and 725 °C [6]. The k_{chem} values in Figure 4.27 were obtained at an oxygen partial pressure of 0.1 bar. Søgaard et al. evaluated the shown k_{chem} values in the temperature range between 700 °C and 900 °C at an pO_2 of 0.21 atm [52].

It is emphasized that the k_{chem} values of the LSC|STO thin film are merely compared to the aforementioned literature references to assess how the estimated mean surface exchange coefficients behave in relation to literature data. As all quoted k_{chem} values were obtained at different oxygen partial pressures, a direct comparison normally wouldn't seem legitimate, since the surface exchange coefficient is not only dependent on temperature but also on surrounding oxygen partial pressure.

Figure 4.27 shows that the logarithm of k_{chem} is linearly dependent on the inverse temperature and that the surface exchange coefficient increases with increasing temperature, which is in accordance with the literature data. However, comparing the absolute k_{chem} values of the LSC thin films at 144 °C/146 °C to the plotted literature data, suggests that the obtained values in this work are overestimated. Even though deviations between the extrapolated literature data evidently exist, all extrapolated curves point to lower absolute values of k_{chem} at said temperature.

At 194 °C the extrapolated k_{chem} values of the work of Søgaard et al. and Chen et al. are $2.71 \cdot 10^{-14} cm/s$ and $3.86 \cdot 10^{-16} cm/s$ and are therefore lower compared to the k_{chem} of the LSC|STO thin film by approximately a factor of 20 and 1000, respectively. However, the estimated average k_{chem} values at 194 °C and 204 °C coincide with the extrapolated data of Egger et al.

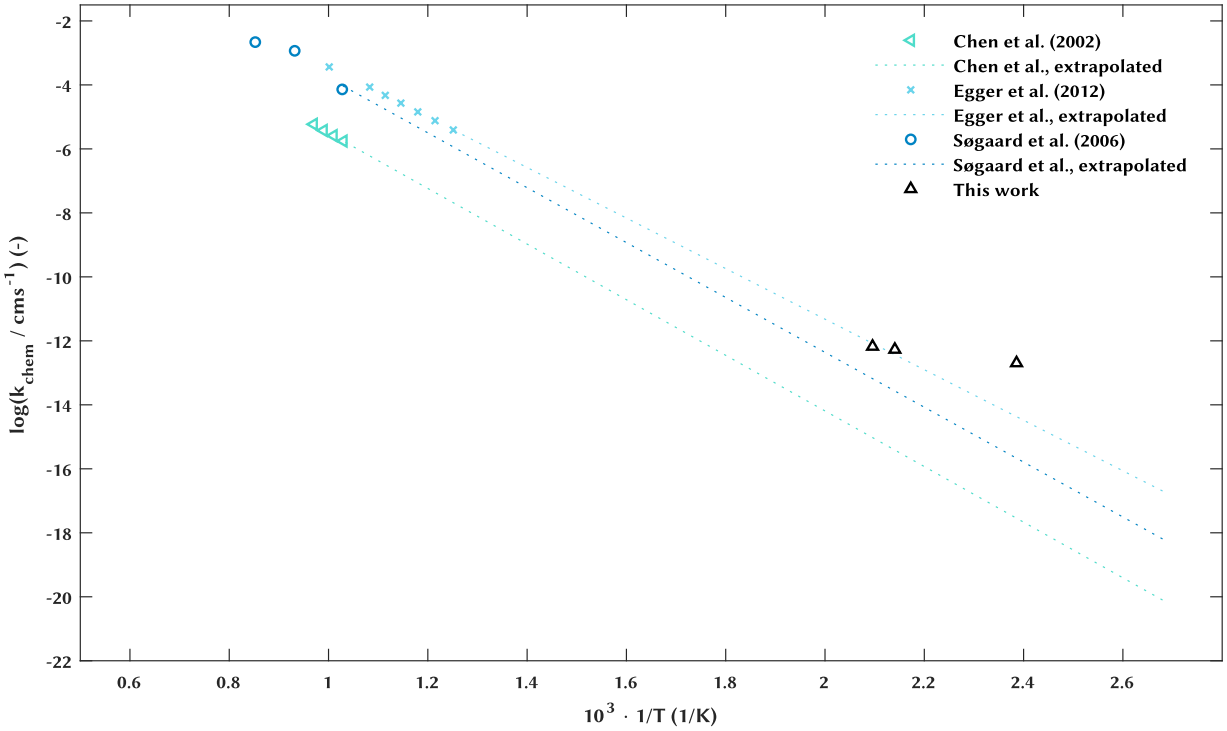

Figure 4.27.: Logarithm of k_{chem} dependent on the inverse temperature. k_{chem} values of the 10 nm LSC|STO thin film are compared to literature data from Chen et al. [80], Egger et al. [6] and Søgaard et al. [52]. The values, that were taken from literature, were fitted with a linear function and extrapolated to the considered temperature range of this work.

Even though reports of epitaxial LSC thin films exist, that either had higher [83] or similar [84] surface exchange coefficients compared to bulk LSC, a discussion, as to why k_{chem} of the LSC|STO thin film shows a similar behavior, is difficult, since the surface exchange coefficients in this work were derived on presumptions in regard to the observed drift. Thus, further research is required in order to elucidate the origin of the drift at elevated temperatures in the measured data. Again, it would be beneficial to rerun the experiments on the thin films in a setting, in which the influence of the flush time is either eliminated or at least drastically minimized, as this would enable experiments also at higher temperatures.

4.4.3. Equilibrium conductivity

This subsection will present how the conductivity of the LSC thin films changes with oxygen partial pressure, temperature and chosen substrate. The values of the equilibrium conductivity were obtained as described in subsection 3.4.1. Raw conductivity relaxation data for each LSC thin film at different temperatures can be found in the appendix (see Appendix C).

a) LSC|LAO

Three LSC thin films with different thicknesses were deposited on LAO. In Figure 4.28 the electrical conductivity of a 10 nm thick LSC thin film is plotted against the logarithm of the oxygen partial pressure in the surrounding atmosphere.

The conductivity of the sample decreases with decreasing pO_2 in the surrounding atmosphere at all temperatures. The observed behavior is in accordance with the defect model for LSC. A clear temperature dependence of σ is not visible. Even though the values of the equilibrium conductivity of the LSC thin film at 400 °C and 406 °C are lower than the σ values that were derived at 343 °C, the thin film exhibits the highest conductivity at 360 °C.

A pronounced drift in the data for experiments that were conducted at 268 °C, 387 °C and 441 °C was observed (see Figure C.2), therefore the equilibrium conductivity was not evaluated for these experiments.

Figure 4.29 shows the pO_2 dependence of σ for a 28 nm thick LSC thin film at different temperatures. The conductivity of said thin film is higher compared to that of the 10 nm thick thin film. The value of σ at 349 °C of the 28 nm LSC|LAO thin film is higher compared to the σ value

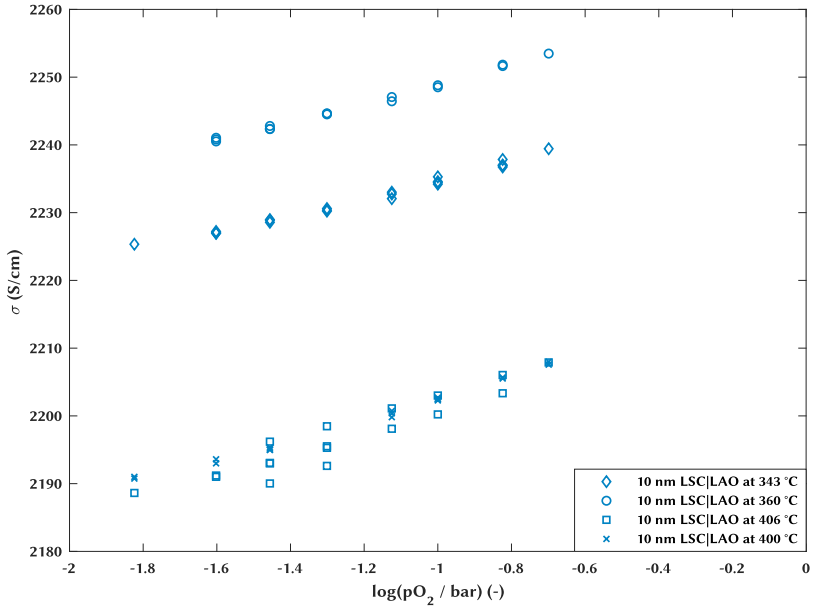

Figure 4.28.: Electrical conductivity σ vs. the logarithm of the pO_2 in the surrounding atmosphere of a 10 nm LSC|LAO thin film at different temperatures.

at 343 °C of the 10 nm LSC|LAO thin film by approximately a factor of 1.33. The conductivity decreases with increasing temperature except for the experiments that were carried out at 299 °C and 309 °C.

σ also decreases with decreasing pO_2. Even though the pO_2 dependence seems to be less distinct, it is in fact the same compared to the other two LSC thin films that were deposited on LAO.

In Figure 4.30 the pO_2 dependence of σ of the third LSC|LAO thin film is shown. The film has a thickness of 40 nm. The σ values of this thin film are comparable to the σ values that were obtained for the 10 nm thick thin film. σ at 343 °C of the 10 nm LSC|LAO thin film is higher by approximately a factor of 1.13 compared to the value of the 40 nm thick thin film at 345 °C. Again, decreasing σ values are observed with decreasing pO_2. The conductivity also decreases with increasing temperature with the exception of two experiments that were conducted at 423 °C and 462 °C.

The significant difference in conductivity between the single LSC|LAO thin films could be connected to different conditions during film deposition. Firstly, the 28 nm LSC|LAO thin film was deposited with a different target. The resulting strain effects in the deposited film due

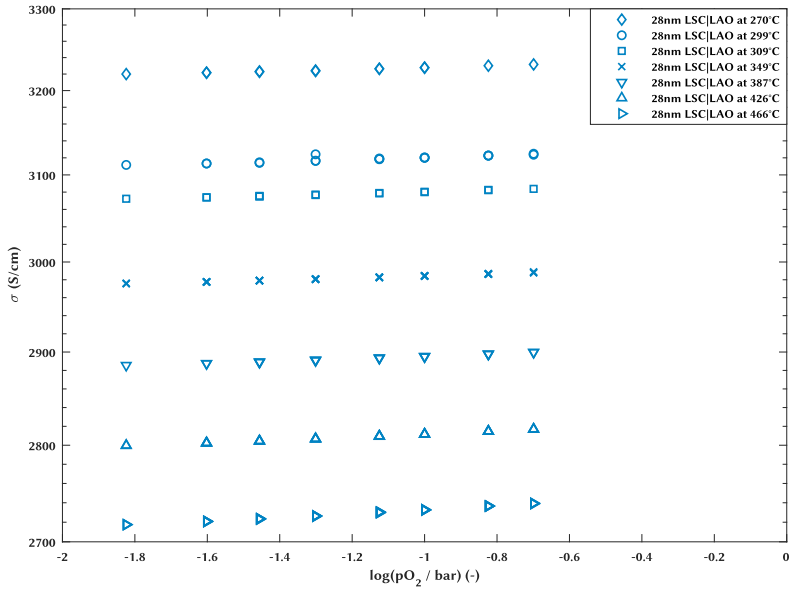

Figure 4.29.: Electrical conductivity σ vs. the logarithm of the pO_2 in the surrounding atmosphere of a 28 nm LSC|LAO thin film at different temperatures.

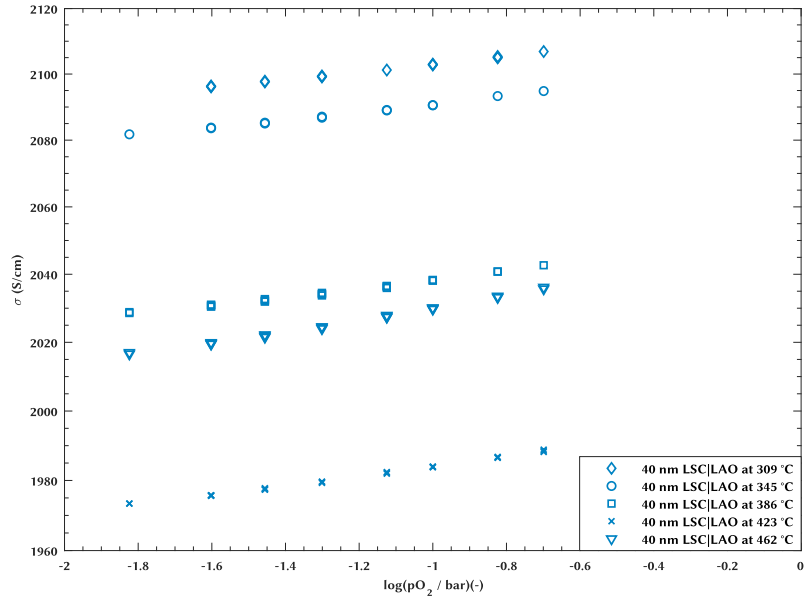

Figure 4.30.: Electrical conductivity σ vs. the logarithm of the pO_2 in the surrounding atmosphere of a 40 nm LSC|LAO thin film at different temperatures.

to the lattice mismatch between LSC and LAO and relaxation thereof, might therefore differ and may be the reason for the discrepancy of the absolute σ values of the LSC|LAO thin films. Secondly, different heating rates were used during deposition. The heating rate was fixed at 88 % for the 28 nm thick film, for the other two LSC|LAO thin films the heating rate was fixed at 80 % and therefore slightly lower.

b) LSC|STO

Figure 4.31 presents oxygen partial pressure dependence of σ for a 10 nm thick LSC thin film that was deposited on STO. The conductivity of this thin film is well within the range of the conductivity that was obtained for the 40 nm LSC|LAO thin film, which was slightly lower compared to the conductivity of the 10 nm LSC|LAO thin film. Again, σ decreases with decreasing pO_2 as expected from defect chemistry. The σ values for the two experiments that were done at 430 °C are in agreement. However, they are lower than the conductivity values that were evaluated at 460 °C and are therefore different to the otherwise observed decreasing conductivity with increasing temperature in the other samples.

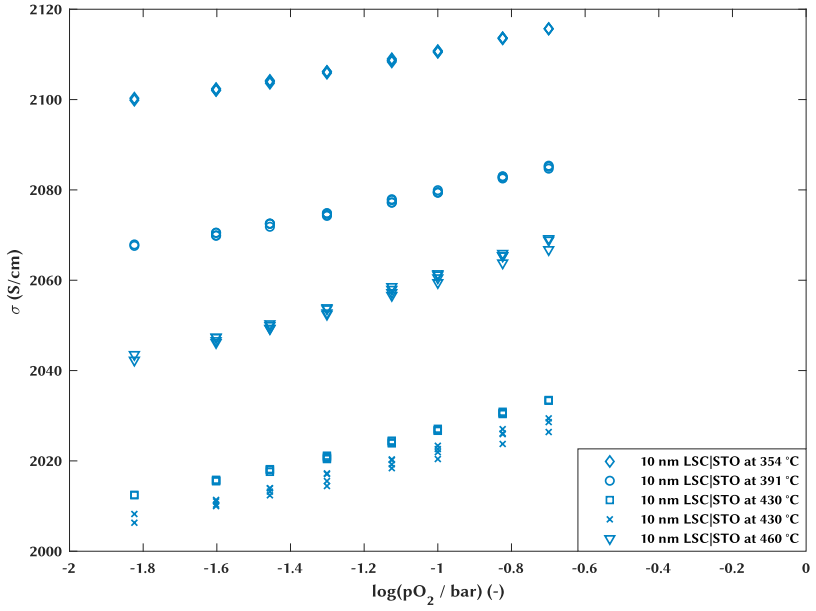

Figure 4.31.: Electrical conductivity σ vs. the logarithm of the pO_2 in the surrounding atmosphere of a 10 nm LSC|STO thin film at different temperatures.

c) LSC|MgO

The pO_2 dependence of the conductivity of a 20 nm LSC|MgO thin film is shown in Figure 4.32. In contrast to the previously presented LSC thin films, that were either deposited on LAO or STO, the LSC|MgO thin film exhibits a much lower conductivity at all temperatures. The highest σ values are approximately 620 S/cm at 471 °C, the lowest σ values are approximately 480 S/cm at 274 °C. σ increases with increasing temperature for this thin film. Although one exception is observed for the measurement, that was carried out at 435 °C. The oxygen partial pressure dependence of the electrical conductivity, however, matches the dependence of the LSC|LAO and LSC|STO thin films, σ decreases with decreasing pO_2.

The LSC|MgO thin film exhibited a drift in the measured data at all considered temperatures (Figure C.5), which explains the fluctuating σ values at constant temperatures in Figure 4.32. The transient response was only measured at 274 °C. For all other experiments the acquisition time for each pO_2 was 300 s. The polarization of the applied voltage was changed every 60 s. After the pO_2 was switched, the reactor was flushed for 900 s before the measurement was started again to ensure that the new oxygen partial pressure was reached.

The outlier in Figure C.5e,f was caused by an input error. The values of the O_2 and N_2 gas streams were interchanged in each instance and due to the higher oxygen partial pressure the conductivity of the sample increased.

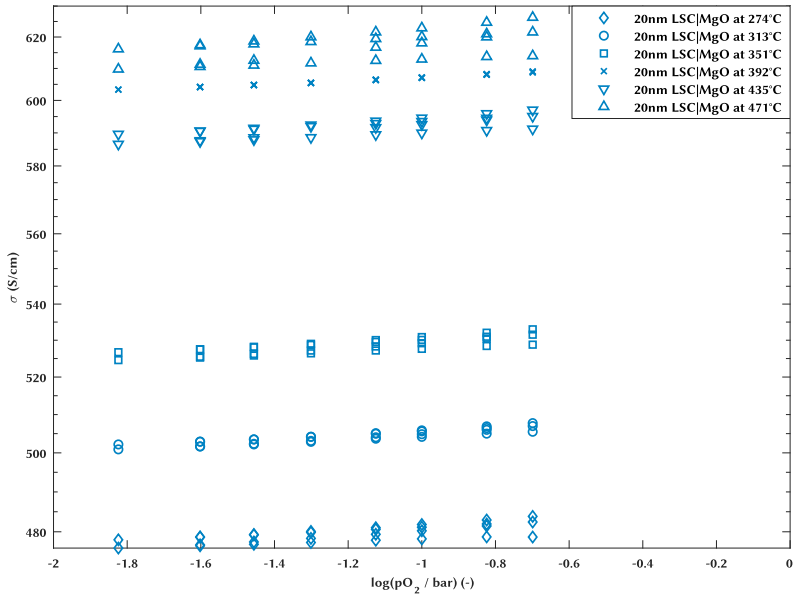

Figure 4.32.: Electrical conductivity σ vs. the logarithm of the pO_2 in the surrounding atmosphere of a 20 nm LSC|MgO thin film at different temperatures.

d) Discussion

The electrical conductivity of $La_{1-x}Sr_xCoO_{3-\delta}$ depends on the Sr content x, the oxygen partial pressure and the temperature [51].

Petrov et al. found that σ decreases with increasing temperature for $x \geq 0.3$ [49]. Similar results were obtained by Mineshige et al., they found that the conductivity decreases with increasing temperature for $0.25 < x \leq 0.7$ [50]. Both studies were carried out on bulk LSC. The $La_{1-x}Sr_xCoO_{3-\delta}$ thin films in this work were prepared with $x = 0.4$. The overall temperature dependence of σ for the thin films, that were deposited on LAO and STO, is in good agreement with the literature. The LSC|MgO thin film, however, showed an overall deviant behavior compared to temperature dependence of bulk LSC found in the literature.

$La_{1-x}Sr_xCoO_{3-\delta}$ is a p-type conductor, its conductivity is connected to the concentration of electron holes. As the oxygen nonstoichiometry δ (= $[V_O^{\bullet\bullet}]$) increases with decreasing pO_2, the hole concentration decreases [6, 49, 52, 53]. As a result the conductivity of the material decreases. This is consistent with the observed behavior of the LSC thin films. σ decreased with decreasing pO_2 for all thin films. The conductivity also becomes more dependent on the surrounding oxygen partial pressure with increasing temperature, since the oxygen nonstoichiometry increases with increasing temperature [53]. The higher concentration of oxygen vacancies at elevated temperatures is balanced by a decreasing electron hole concentration [49]. At higher temperatures the slope of the pO_2 dependence became more steep for all thin films, showing a growing oxygen partial pressure dependence (see Figure 4.28 - Figure 4.32). This behavior is also in accordance with the data obtained by Bucher et al., Mizusaki et al. and Søgaard et al. [51, 52, 85].

The absolute values of σ, that were found for the 10 nm and 40 nm thick LSC|LAO thin films as well as for the 10 nm LSC|STO thin film, are slightly lower compared to the bulk conductivities, that were obtained by Egger et al., Petrov et al. and Søgaard et al. Egger et al. found σ to be above 2200 S/cm at 525 °C and an oxygen partial pressure of 0.1 bar. At 650 °C and 0.2 bar Søgaard et al. obtained a σ value slightly above 2100 S/cm. The quoted σ values were all evaluated for $La_{0.6}Sr_{0.4}CoO_{3-\delta}$.

The conductivity of the 28 nm LSC|LAO thin film stands out. At 270 °C σ was slightly above 3200 S/cm at 0.2 bar. This value is well above the bulk value of approximately 2500 S/cm at 0.21 bar and approximately 298 °C, which was obtained by Petrov et al. [49].

In addition to the overall deviant temperature dependence of σ of the LSC|MgO thin film, the absolute values of σ are also lower than the values for bulk LSC. The mismatch between the lattice parameters of MgO and LSC produces a columnar structure in the grown thin film. In this structure, the grains are separated by grain boundaries, which could be less conductive. Since the van der Pauw method measures the sheet resistivity, the obtained conductivity will stem from both grains and grain boundaries and will, because of the higher resistivity of the grain boundaries, be decreased.

In order to asses the influence of the grain boundaries on the conductivity of the LSC|MgO film, the grain size and the grain boundary width are assumed to be 40 nm and 1 nm, respectively. For a grain conductivity of 2100 S/cm and an absolute conductivity of 530 S/cm, the estimation shows that

$$\frac{\sigma_g}{\sigma_{gb}} \approx 117, \tag{4.9}$$

with σ_g and σ_{gb} denoting the conductivity of the grains and the conductivity of the grain boundaries, respectively. Therefore σ_{gb} can be estimated to be $\approx$ 18 S/cm according to our simple model, a value that is difficult to obtain and not available from literature for LSC thin films.

Sata et al. found the same overall temperature dependence in air of a $La_{0.6}Sr_{0.4}CoO_{3-\delta}$ thin film, that was deposited on MgO [86]. Moreover, the absolute σ values, that were obtained by Sata et al., are in excellent agreement with the obtained conductivity values of this work [86]. Joo et al. measured the conductivity of a 50 nm thick $La_{0.6}Sr_{0.4}CoO_{3-\delta}$ thin film, that was deposited on MgO, by ac impedance at different temperatures and oxygen partial pressures. They obtained σ values, that were also lower than values obtained for bulk LSC. However, the absolute values of σ were higher than the values obtained in this work, e.g. at 450 °C Joo et al. obtained a σ value, that was slightly less than 1000 S/cm at a pO_2 of 0.1 bar [87]. The higher conductivity could be connected to a higher oxygen partial pressure during film deposition (= factor 10), possibly resulting in fewer oxygen vacancies. However, this doesn't account for the fact, that the conductivity of the LSC|MgO thin film obtained by Joo et al. decreased with increasing temperature, which is in accordance with the above mentioned literature data.

At the outset of these experiments it was anticipated that the conductivity of the LSC|LAO thin film would exceed the conductivity of the LSC|STO thin film as the oxygen deficiency is expected to be lower in the compressive strained LSC|LAO thin film. The conductivity of

the 10 nm LSC|LAO thin film is indeed slightly higher compared to the 10 nm LSC|STO thin film at all considered temperatures. At 360 °C the obtained σ of the 10 nm LSC|LAO thin film is approximately 6 % higher than the σ value of the 10 nm LSC|STO film at 354 °C. So far, a comparison of the conductivity dependent on the film thickness between films on different substrates isn't possible. Even a comparison between the three LSC|LAO films can't be justified because the films were not deposited under the exact same conditions and different targets were used.

5. Summary

The oxygen exchange kinetics of (Fe:)STO single crystals, $La_{0.6}Sr_{0.4}CoO_{3-\delta}$ polycrystals and $La_{0.6}Sr_{0.4}CoO_{3-\delta}$ thin films were investigated by employing the electrical conductivity relaxation method. Sample geometries allowed for application of the van der Pauw method for measurement of the dc-conductivity. Relaxation profiles were fitted to a flush time corrected solution of Fick's 2nd law assuming a plane sheet geometry and one-dimensional transport processes. In addition, the equilibrium conductivity was derived from the recorded data, which provided insight into the oxygen partial pressure dependence of σ. The pO_2 steps were applied in both oxidizing and reducing direction with the pO_2 ranging from 0.015 bar to 0.2 bar. In addition to the experimental work, large focus was laid on the evaluation of conductivity relaxation profiles. For this reason a data analysis procedure was developed in MATLAB, which allowed for determination of the respectively desired fitting parameters (e.g. τ_f, k_{chem}).

Measurements on the (Fe:)STO single crystals were performed in the temperature range between 542 °C and 767 °C. In the considered pO_2 range the conductivity was found to be p-type with a pO_2 dependence of roughly $\sigma \propto {pO_2}^{1/6}$ for both single crystals. As a consequence of the higher acceptor concentration in the deliberately doped Fe:STO single crystal, which results in a higher charge carrier concentration ($\widehat{=}$ electron holes), the conductivity of the Fe:STO single crystal exceeded the conductivity of the nominally undoped STO single crystal by approximately a factor of 2.3.

For both single crystals the relaxation process was dominated by the surface reaction. Thus, only the surface exchange coefficient could be evaluated from the respective relaxation data. Within the considered temperature range the surface kinetics of the STO single crystal were faster compared to the Fe:STO single crystal suggesting that the trapping effect had a greater impact on the Fe:STO single crystal [22]. Generally, the obtained absolute values were reasonable in comparison to literature data [12, 28].

$La_{0.6}Sr_{0.4}CoO_{3-\delta}$ thin films were deposited on LAO, STO and MgO via pulsed laser deposition. The evaluation of surface exchange coefficient for the LSC thin films was complicated by two factors. Firstly, τ_f superposed the thin films' specific relaxation time above $\approx$ 200 °C. As a consequence, experiments for the evaluation of k_{chem} were carried out in the temperature range between 144 °C and 204 °C. Secondly, a pronounced drift in the measured data was observed in said temperature range. The drift in the data necessitated a drift correction as well as an adaption of the fitting routine. Furthermore, single k_{chem} values could not be attributed to respective pO_2 steps as the drift was superimposed on entire data sets. Hence, obtained k_{chem} values were averaged over the entire pO_2 range and served merely as estimates at the respectively considered temperature. In addition, the estimation of k_{chem} also required the approximate value of τ_f, which was evaluated from measurements of the LSC thin films in the temperature range between 267 °C and 466 °C, within which the samples effectively acted as oxygen sensors. All obtained k_{chem} values at 144 °C/146 °C were fairly similar independent of the respective substrate. However, in comparison to extrapolated literature data the absolute values seemed too high, suggesting that the drift correction might have overestimated the surface kinetics at said temperature. It is noted that the drift in the relaxation data of the LSC thin films was also observed in the temperature range between 267 °C and 466 °C, however, less pronounced. The origin of the drift has not been determined yet and thus, remains an open question.

The conductivity of the LSC thin films was obtained from measurements in the temperature range between 267 °C and 466 °C. In accordance with literature data the conductivity was found to be p-type independent of the thin film's substrate [6, 51–53]. Generally, the conductivity of the epitaxial grown thin films on LAO and STO decreased with increasing temperature. Absolute σ values of the compressive strained thin films on LAO were slightly higher compared to the values, which were obtained for the tensile strained films on STO. This was attributed to a lower oxygen deficiency in the compressive strained thin films. In both instances the conductivity was comparable to values, which were previously obtained for bulk LSC [6, 49, 52]. Contrary to the expitaxial grown films, σ, overall, increased with increasing temperature for the LSC|MgO thin film. Grain boundaries in the columnar structure of the LSC|MgO thin film were responsible for absolute σ values, that were considerably lower compared to the epitaxial grown thin films. The magnitude of the grain boundary influence on σ was estimated, revealing that the conductivity of the grains exceeded the conductivity of the grain boundaries by approximately two orders of magnitude.

Further, it was noticed that experiments could only be carried out successfully, if the resistance of the samples exceeded the resistance stemming from the setup itself. This requirement wasn't fulfilled in case of the polycrystalline LSC pellets and as consequence the conductivity relaxation experiments did neither yield results for the kinetic parameters nor could the equilibrium conductivity be obtained for these samples.

A. Results of estimating the reactor flush time

Table A.1.: Results of fitting relaxation data to Equation (3.17). The values presented in this table correspond to the values that are shown in Figure 4.16a.

	40 nm LSC|LAO			28 nm LSC|LAO	20 nm LSC|MgO	10 nm LSC|LAO		
pO_2 (bar)	τ_f (s)							
0.15	342	578	389	-	249	-	182	199
0.1	470	676	776	-	229	-	196	217
0.075	290	487	920	326	318	-	181	233
0.05	395	358	524	-	251	-	213	236
0.035	420	516	615	-	215	-	203	229
0.025	587	510	706	487	213	173	305	175
0.015	493	651	-	704	221	195	274	258
0.025	384	356	384	397	180	305	229	264
0.035	371	419	641	268	251	368	252	250
0.05	623	530	530	376	183	366	276	386
0.075	312	607	627	459	183	252	260	245
0.1	669	-	455	306	204	374	236	294
0.15	489	407	581	431	182	269	268	308
0.2	335	507	466	366	209	272	399	-

Table A.2.: Results of fitting relaxation data to Equation (3.17). The values presented in this table correspond to the values that are shown in Figure 4.16b.

	40 nm LSC|LAO		**28 nm LSC|LAO, 309 °C**	**28 nm LSC|LAO, 299 °C**	
pO_2 (bar)	**τ_f (s)**				
0.15	331	175	346	-	134
0.1	384	263	324	-	190
0.075	-	-	383	-	264
0.05	217	212	162	-	256
0.035	279	341	-	-	193
0.025	191	220	401	-	-
0.015	336	-	160	322	-
0.025	207	282	462	132	-
0.035	655	237	183	146	-
0.05	221	186	179	136	-
0.075	217	270	296	191	-
0.1	310	227	235	242	-
0.15	248	176	-	256	-
0.2	213	257	127	154	-

Table A.3.: Results of fitting relaxation data to Equation (3.17). The values presented in this table correspond to the values that are shown in Figure 4.16c.

	40 nm LSC|LAO	**10 nm LSC|LAO**		**10 nm LSC|STO**		**28 nm LSC|LAO**		
pO_2 (bar)	**τ_f (s)**							
0.15	217	122	123	179	230	172	156	180
0.1	-	161	156	178	188	217	112	235
0.075	379	310	393	224	188	235	224	202
0.05	209	297	125	207	162	176	156	173
0.035	240	110	-	193	237	216	151	152
0.025	172	567	346	270	229	247	205	182
0.015	199	480	-	194	156	214	209	195
0.025	268	123	-	154	192	116	228	144
0.035	193	195	351	137	237	138	226	215
0.05	203	145	216	188	159	158	168	173
0.075	290	217	-	164	218	158	174	219
0.1	-	-	247	266	165	180	126	186
0.15	314	161	-	203	164	153	148	138
0.2	320	-	-	140	164	126	129	-

Table A.4.: Results of fitting relaxation data to Equation (3.17). The values presented in this table correspond to the values that are shown in Figure 4.16d.

	40 nm LSC|LAO		**10 nm LSC|LAO**	**10 nm LSC|STO**		**28 nm LSC|LAO**	
pO_2 (bar)	**τ_f (s)**						
0.15	163	174	152	223	-	186	161
0.1	136	193	161	194	243	254	178
0.075	157	187	348	206	-	161	235
0.05	171	157	283	239	233	178	149
0.035	130	195	343	274	-	228	249
0.025	150	134	221	244	-	124	-
0.015	184	230	-	198	249	194	-
0.025	134	197	-	267	-	136	-
0.035	193	165	-	188	189	156	-
0.05	198	-	-	216	251	198	-
0.075	199	178	195	183	246	290	-
0.1	196	164	240	-	188	160	-
0.15	183	194	222	195	190	133	-
0.2	139	200	274	147	138	161	-

Table A.5.: Results of fitting relaxation data to Equation (3.17). The values presented in this table correspond to the values that are shown in Figure 4.16e.

	10 nm LSC|LAO, 406 °C		**10 nm LSC|LAO, 400 °C**	
pO_2 (bar)	**τ_f (s)**			
0.15	128	138	146	203
0.1	193	187	181	166
0.075	171	189	353	295
0.05	174	202	323	276
0.035	180	185	174	167
0.025	-	182	375	152
0.015	-	225	238	206
0.025	-	166	152	-
0.035	234	169	258	-
0.05	206	209	130	238
0.075	201	-	221	187
0.1	295	267	314	127
0.15	256	257	122	237
0.2	326	177	266	95

Table A.6.: Results of fitting relaxation data to Equation (3.17). The values presented in this table correspond to the values that are shown in Figure 4.16f.

	40 nm LSC|LAO		10 nm LSC|STO		28 nm LSC|LAO	
pO_2 (bar)	τ_f (s)					
0.15	215	143	171	162	207	109
0.1	160	181	206	187	158	224
0.075	169	148	199	-	110	-
0.05	172	273	199	206	158	134
0.035	275	130	181	226	155	172
0.025	157	248	209	213	204	169
0.015	244	246	192	262	217	151
0.025	175	187	229	179	142	257
0.035	295	185	127	157	184	362
0.05	115	137	173	151	145	300
0.075	128	212	149	179	157	180
0.1	200	227	224	243	-	158
0.15	143	160	165	203	187	143
0.2	178	163	207	233	186	205

Table A.7.: Numerical values of τ_f for different LSC thin films at a furnace set temperature of 500 °C. The fitting results correspond to the τ_f values shown in Figure 4.16g and Figure 4.17g.

	40 nm LSC|LAO		10 nm LSC|LAO		10 nm LSC|STO		28 nm LSC|LAO		
pO_2 (bar)	τ_f (s)								
0.15	146	193	-	141	173	204	169	231	159
0.1	194	177	165	135	203	198	187	201	201
0.075	240	157	181	151	238	119	151	186	127
0.05	244	219	107	160	180	265	223	222	201
0.035	187	179	200	235	170	255	187	162	186
0.025	179	231	140	155	181	166	154	166	198
0.015	211	240	211	171	186	136	165	196	161
0.025	191	153	192	201	277	219	202	155	184
0.035	251	148	407	238	127	127	200	211	185
0.05	168	163	240	248	163	143	166	159	172
0.075	160	164	199	334	171	175	154	160	205
0.1	182	141	176	133	144	179	184	216	96
0.15	154	186	254	218	232	162	163	151	173
0.2	182	234	358	-	185	215	182	168	137

B. Calculation of the relative change in oxygen content with respect to the thin film thickness

Table B.1.: Results of calculating the relative change in oxygen content in respect to the film thickness Δd for a 10 nm LSC|STO thin film at 146 °C. σ_0 and σ_∞ were obtained from drift corrected data. The corresponding raw data is shown in Figure 4.18.

pO_2	σ_0	σ_∞	σ_0/σ_∞	$\Delta\,[h^\bullet]$	$\Delta\,[V_O^{\bullet\bullet}]$	$\Delta\,d$
0.1	2254.49	2250.27	0.99813	0.0018706	0.00037413	$3.74 \cdot 10^{-10}$
0.075	2245.86	2243.27	0.99885	0.0011502	0.00023004	$2.30 \cdot 10^{-10}$
0.05	2239.27	2236.12	0.99859	0.0014076	0.00028153	$2.82 \cdot 10^{-10}$
0.035	2232.41	2229.89	0.99887	0.0011266	0.00022531	$2.25 \cdot 10^{-10}$
0.025	2226.10	2224.16	0.99913	0.0008683	0.00017365	$1.74 \cdot 10^{-10}$
0.015	2220.41	2217.95	0.99889	0.0011052	0.00022104	$2.21 \cdot 10^{-10}$
0.025	2214.34	2216.93	1.00117	0.0011669	0.00023339	$2.33 \cdot 10^{-10}$
0.035	2214.47	2216.51	1.00092	0.0009207	0.00018414	$1.84 \cdot 10^{-10}$
0.05	2213.98	2216.42	1.00110	0.0011011	0.00022023	$2.20 \cdot 10^{-10}$
0.075	2214.22	2218.02	1.00172	0.0017183	0.00034367	$3.44 \cdot 10^{-10}$
0.1	2215.64	2216.85	1.00055	0.0005461	0.00010923	$1.09 \cdot 10^{-10}$
0.15	2216.32	2219.80	1.00157	0.0015688	0.00031375	$3.14 \cdot 10^{-10}$
0.2	2219.69	2222.71	1.00136	0.0013606	0.00027213	$2.72 \cdot 10^{-10}$
0.15	2222.63	2220.11	0.99886	0.0011354	0.00022709	$2.27 \cdot 10^{-10}$
0.1	2218.19	2215.03	0.99857	0.0014251	0.00028503	$2.85 \cdot 10^{-10}$
0.075	2212.09	2209.96	0.99903	0.0009665	0.00019330	$1.93 \cdot 10^{-10}$
0.05	2207.32	2204.50	0.99872	0.0012796	0.00025592	$2.56 \cdot 10^{-10}$
0.035	2201.18	2199.07	0.99904	0.0009622	0.00019245	$1.92 \cdot 10^{-10}$
0.025	2195.58	2194.02	0.99929	0.0007133	0.00014265	$1.43 \cdot 10^{-10}$
0.015	2190.18	2188.04	0.99902	0.0009777	0.00019553	$1.96 \cdot 10^{-10}$
0.025	2183.36	2185.40	1.00093	0.0009332	0.00018664	$1.87 \cdot 10^{-10}$
0.035	2182.82	2183.79	1.00045	0.0004452	0.00008905	$8.90 \cdot 10^{-11}$
0.05	2181.98	2183.65	1.00076	0.0007644	0.00015287	$1.53 \cdot 10^{-10}$
0.075	2182.70	2185.30	1.00119	0.0011911	0.00023823	$2.38 \cdot 10^{-10}$

Table B.2.: Results of calculating the relative change in oxygen content in respect to the film thickness Δd for a 10 nm LSC|STO thin film at 194 °C. σ_0 and σ_∞ were obtained from drift corrected data. The corresponding raw data is shown in Figure 4.20.

pO_2	σ_0	σ_∞	σ_0/σ_∞	$\Delta\,[h^\bullet]$	$\Delta\,[V_O^{\bullet\bullet}]$	$\Delta\,d$
0.05	2250.69	2247.99	0.99880	0.0011994	0.00023987	$2.40 \cdot 10^{-10}$
0.035	2247.56	2245.48	0.99908	0.0009249	0.00018498	$1.85 \cdot 10^{-10}$
0.025	2244.92	2242.71	0.99901	0.0009860	0.00019719	$1.97 \cdot 10^{-10}$
0.015	2242.09	2239.83	0.99899	0.0010077	0.00020155	$2.02 \cdot 10^{-10}$
0.025	2239.04	2241.85	1.00125	0.0012524	0.00025049	$2.50 \cdot 10^{-10}$
0.035	2241.32	2243.50	1.00097	0.0009748	0.00019496	$1.95 \cdot 10^{-10}$
0.05	2243.52	2245.97	1.00109	0.0010898	0.00021795	$2.18 \cdot 10^{-10}$
0.075	2246.27	2249.41	1.00140	0.0013978	0.00027955	$2.80 \cdot 10^{-10}$
0.1	2249.66	2252.04	1.00106	0.0010580	0.00021159	$2.12 \cdot 10^{-10}$
0.15	2252.61	2256.52	1.00174	0.0017351	0.00034701	$3.47 \cdot 10^{-10}$
0.2	2257.08	2259.66	1.00114	0.0011407	0.00022815	$2.28 \cdot 10^{-10}$
0.15	2260.28	2258.07	0.99902	0.0009756	0.00019513	$1.95 \cdot 10^{-10}$
0.1	2257.60	2254.17	0.99848	0.0015195	0.00030391	$3.04 \cdot 10^{-10}$
0.075	2253.00	2250.85	0.99904	0.0009559	0.00019119	$1.91 \cdot 10^{-10}$
0.05	2249.80	2246.71	0.99862	0.0013768	0.00027535	$2.75 \cdot 10^{-10}$
0.035	2245.41	2243.21	0.99902	0.0009778	0.00019557	$1.96 \cdot 10^{-10}$
0.025	2242.02	2239.97	0.99909	0.0009147	0.00018293	$1.83 \cdot 10^{-10}$
0.015	2238.81	2236.11	0.99880	0.0012046	0.00024092	$2.41 \cdot 10^{-10}$
0.025	2235.10	2237.38	1.00102	0.0010213	0.00020426	$2.04 \cdot 10^{-10}$
0.035	2236.95	2238.84	1.00084	0.0008444	0.00016889	$1.69 \cdot 10^{-10}$
0.05	2238.76	2241.27	1.00112	0.0011236	0.00022472	$2.25 \cdot 10^{-10}$
0.075	2241.44	2244.63	1.00142	0.0014245	0.00028490	$2.85 \cdot 10^{-10}$
0.1	2244.98	2247.60	1.00117	0.0011661	0.00023323	$2.33 \cdot 10^{-10}$
0.15	2247.66	2251.63	1.00177	0.0017658	0.00035317	$3.53 \cdot 10^{-10}$
0.2	2252.15	2255.14	1.00133	0.0013290	0.00026580	$2.66 \cdot 10^{-10}$

Table B.3.: Results of calculating the relative change in oxygen content in respect to the film thickness Δd for a 10 nm LSC|STO thin film at 204 °C. σ_0 and σ_∞ were obtained from drift corrected data. The corresponding raw data is shown in Figure 4.22.

pO_2	σ_0	σ_∞	σ_0/σ_∞	$\Delta\,[h^\bullet]$	$\Delta\,[V_O^{\bullet\bullet}]$	$\Delta\,d$
0.15	2310.86	2307.98	0.99875	0.0012463	0.00024925	$2.49 \cdot 10^{-10}$
0.1	2306.80	2303.72	0.99867	0.0013341	0.00026682	$2.67 \cdot 10^{-10}$
0.075	2301.56	2298.99	0.99888	0.0011179	0.00022359	$2.24 \cdot 10^{-10}$
0.05	2297.65	2294.73	0.99873	0.0012701	0.00025402	$2.54 \cdot 10^{-10}$
0.025	2289.18	2286.91	0.99901	0.0009918	0.00019835	$1.98 \cdot 10^{-10}$
0.015	2285.38	2282.35	0.99868	0.0013224	0.00026448	$2.64 \cdot 10^{-10}$
0.075	2285.61	2288.54	1.00128	0.0012814	0.00025627	$2.56 \cdot 10^{-10}$
0.15	2290.98	2295.25	1.00187	0.0018652	0.00037303	$3.73 \cdot 10^{-10}$
0.2	2295.08	2298.39	1.00144	0.0014419	0.00028839	$2.88 \cdot 10^{-10}$
0.1	2295.40	2291.78	0.99842	0.0015755	0.00031510	$3.15 \cdot 10^{-10}$
0.05	2287.04	2283.83	0.99860	0.0014047	0.00028093	$2.81 \cdot 10^{-10}$
0.035	2282.18	2278.82	0.99853	0.0014711	0.00029421	$2.94 \cdot 10^{-10}$
0.025	2277.53	2275.02	0.99890	0.0011011	0.00022022	$2.20 \cdot 10^{-10}$
0.015	2273.76	2271.13	0.99884	0.0011581	0.00023162	$2.32 \cdot 10^{-10}$
0.025	2268.51	2271.43	1.00129	0.0012866	0.00025732	$2.57 \cdot 10^{-10}$
0.05	2272.10	2274.58	1.00109	0.0010903	0.00021805	$2.18 \cdot 10^{-10}$
0.075	2274.31	2278.60	1.00188	0.0018831	0.00037662	$3.77 \cdot 10^{-10}$
0.1	2277.64	2280.75	1.00136	0.0013629	0.00027257	$2.73 \cdot 10^{-10}$
0.15	2280.75	2284.02	1.00144	0.0014352	0.00028704	$2.87 \cdot 10^{-10}$

Table B.4.: Results of calculating the relative change in oxygen content in respect to the film thickness Δd for a 10 nm LSC|LAO thin film at 144 °C. σ_0 and σ_∞ were obtained from drift corrected data. The corresponding raw data is shown in Figure 4.23.

pO_2	σ_0	σ_∞	σ_0/σ_∞	$\Delta\,[h^\bullet]$	$\Delta\,[V_O^{\bullet\bullet}]$	$\Delta\,d$
0.1	1040.65	1038.71	0.99813	0.0018664	0.00037327	$3.73 \cdot 10^{-10}$
0.075	1042.03	1040.84	0.99886	0.0011394	0.00022788	$2.28 \cdot 10^{-10}$
0.05	1044.20	1043.14	0.99899	0.0010104	0.00020207	$2.02 \cdot 10^{-10}$
0.035	1045.22	1044.42	0.99923	0.0007714	0.00015427	$1.54 \cdot 10^{-10}$
0.025	1046.14	1045.48	0.99937	0.0006301	0.00012602	$1.26 \cdot 10^{-10}$
0.015	1046.87	1046.38	0.99953	0.0004707	0.00009415	$9.41 \cdot 10^{-11}$

Table B.5.: Results of calculating the relative change in oxygen content in respect to the film thickness Δd for a 20 nm LSC|MgO thin film at 144 °C. σ_0 and σ_∞ were obtained from drift corrected data. The corresponding raw data is shown in Figure 4.25.

$\mathbf{pO_2}$	σ_0	σ_∞	σ_0/σ_∞	$\Delta\,[\mathrm{h}^\bullet]$	$\Delta\,[\mathrm{V}_\mathrm{O}^{\bullet\bullet}]$	$\Delta\,\mathbf{d}$
0.075	296.50	296.05	0.99846	0.0015411	0.00030821	$3.08 \cdot 10^{-10}$
0.05	296.43	295.99	0.99850	0.0015014	0.00030028	$3.00 \cdot 10^{-10}$
0.035	295.69	295.31	0.99873	0.0012676	0.00025352	$2.54 \cdot 10^{-10}$
0.025	294.85	294.54	0.99895	0.0010474	0.00020948	$2.09 \cdot 10^{-10}$
0.015	294.05	293.73	0.99894	0.0010587	0.00021174	$2.12 \cdot 10^{-10}$
0.1	298.80	299.21	1.00138	0.0013787	0.00027574	$2.76 \cdot 10^{-10}$
0.15	300.94	301.42	1.00160	0.0016002	0.00032005	$3.20 \cdot 10^{-10}$
0.2	303.40	303.90	1.00167	0.0016718	0.00033435	$3.34 \cdot 10^{-10}$

C. Conductivity relaxation of LSC thin films

C.1. 10 nm LSC|STO

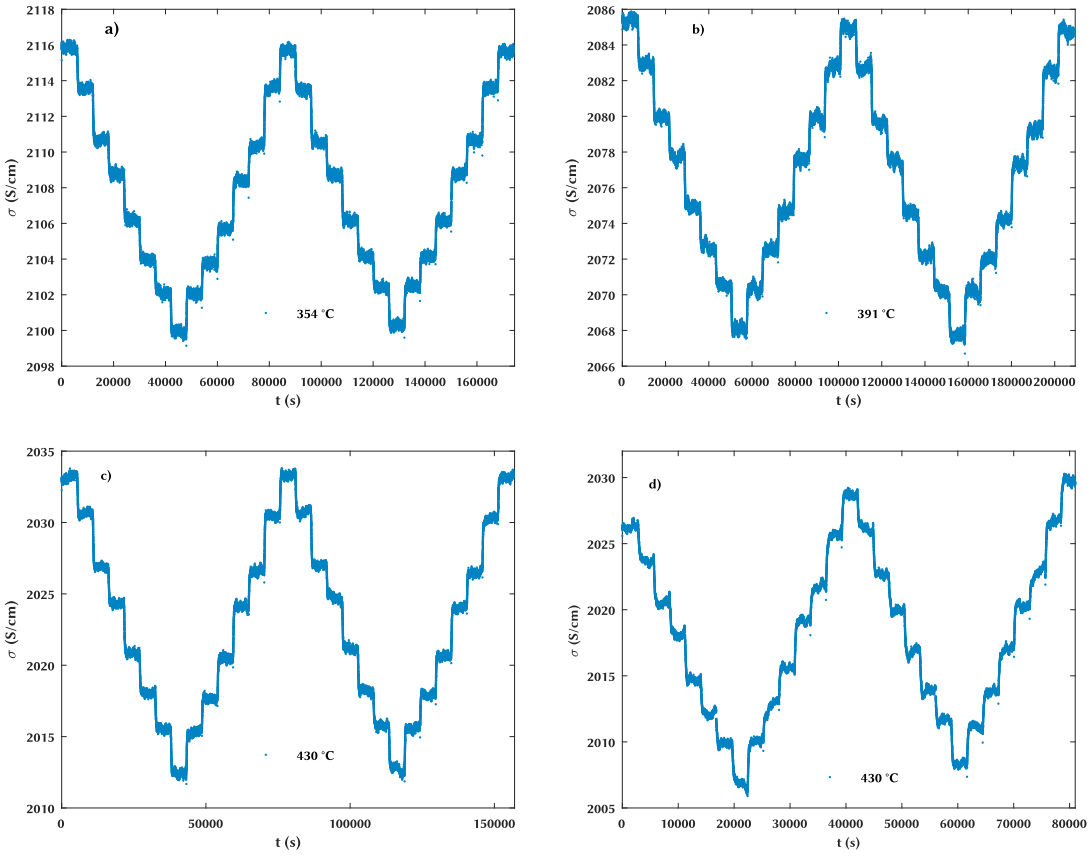

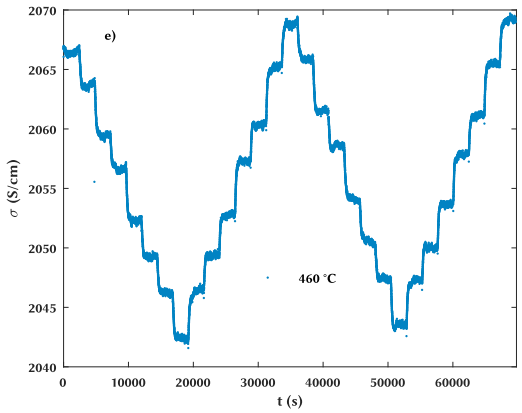

Figure C.1.: 10 nm LSC|STO measured at: **a)** 354 °C, **b)** 391 °C, **c)** 430 °C and **d)** 460 °C. All experiments were started at a pO_2 of 0.2 bar.

C.2. 10 nm LSC|LAO

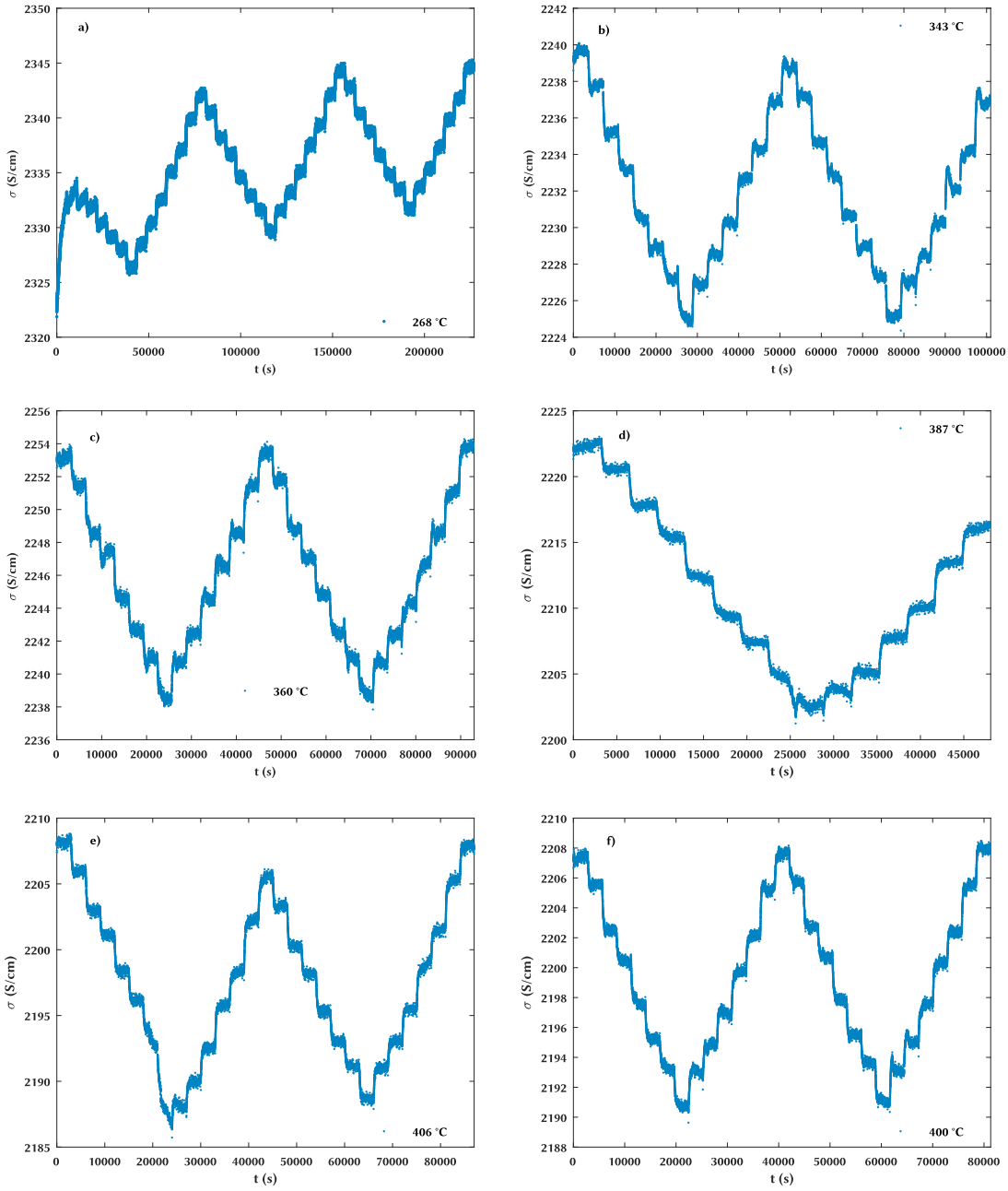

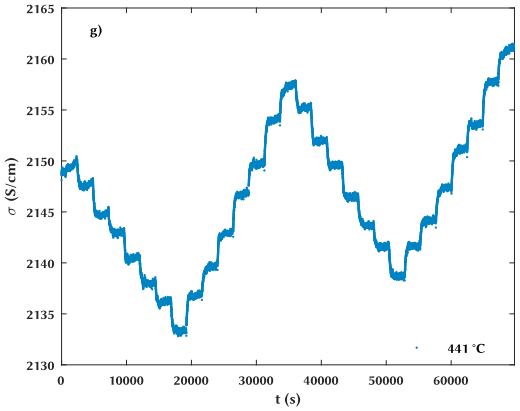

Figure C.2.: 10 nm LSC|LAO measured at: **a)** 268 °C, **b)** 343 °C, **c)** 387 °C, **d)** 406 °C, **e)** 400 °C and **f)** 441 °C. All experiments were started at a pO_2 of 0.2 bar.

C.3. 28 nm LSC|LAO

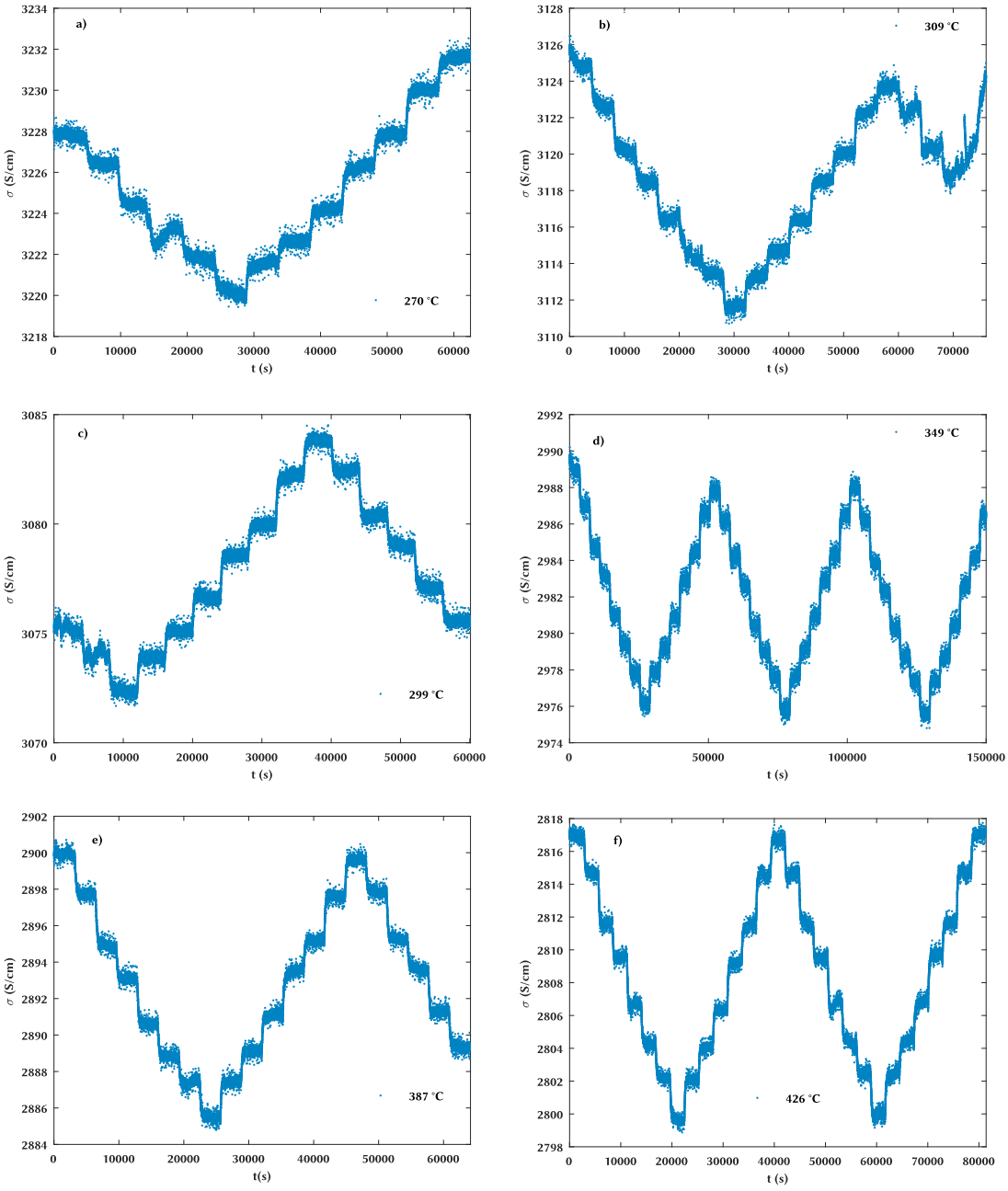

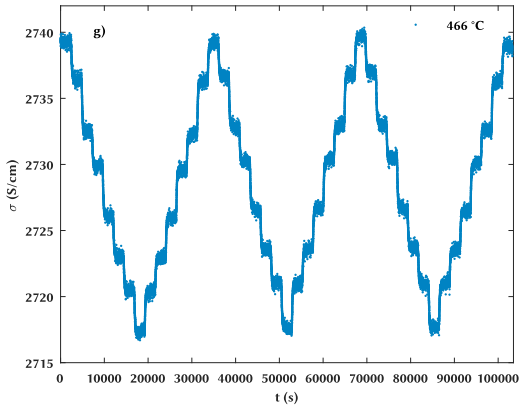

Figure C.3.: 28 nm LSC|LAO measured at: **a)** 270 °C, **b)** 309 °C, **c)** 299 °C, **d)** 349 °C, **e)** 387 °C, **f)** 426 °C and **g)** 466 °C. The experiments shown in **a)** and **c)** were started at an initial pO_2 of 0.1 bar and 0.035 bar, respectively. All other measurements were started at a pO_2 of 0.2 bar.

C.4. 40 nm LSC|LAO

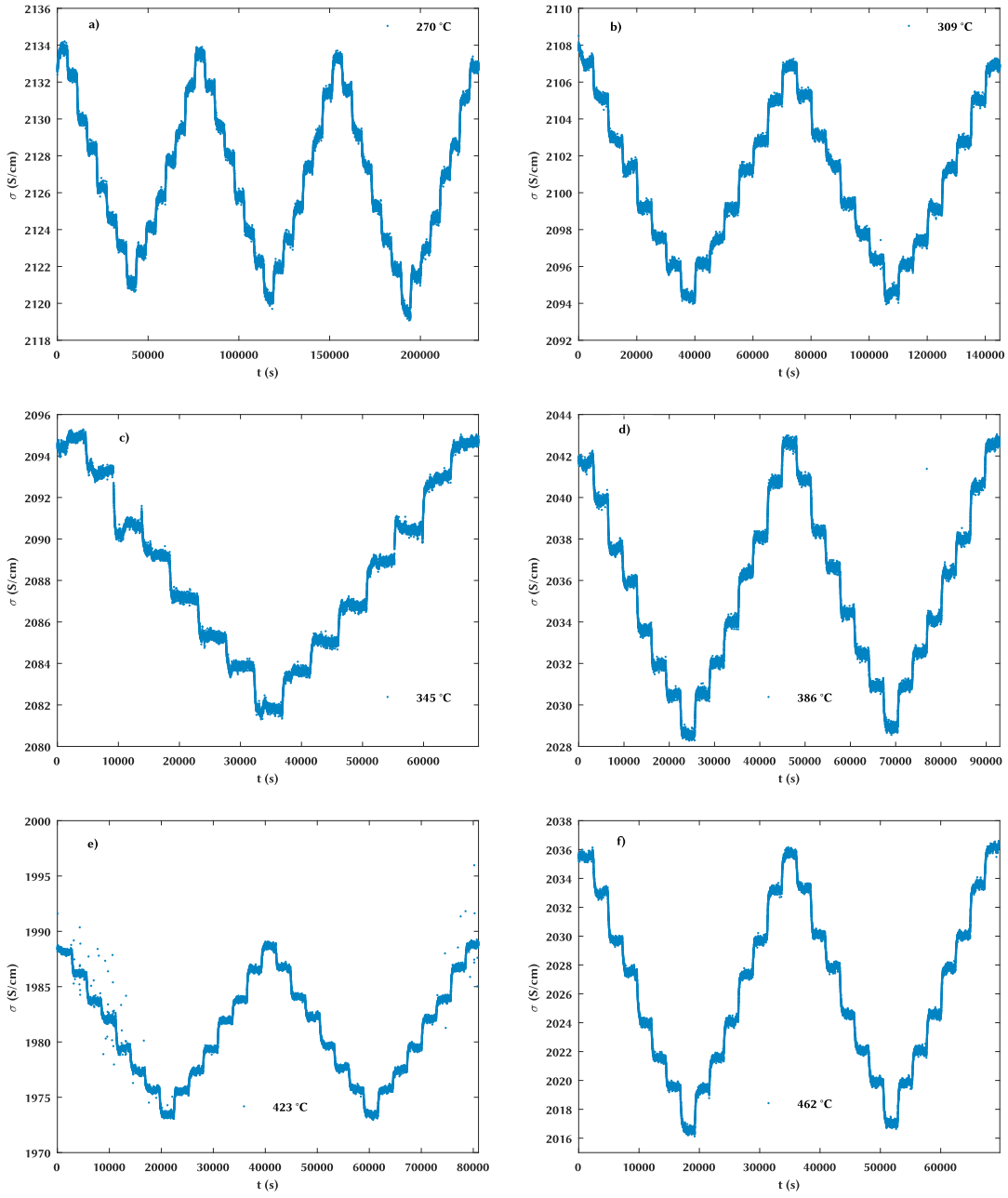

Figure C.4.: 40 nm LSC|LAO measured at: **a)** 270 °C, **b)** 309 °C, **c)** 345 °C, **d)** 386 °C, **e)** 423 °C and **f)** 462 °C. All experiments were started at a pO_2 of 0.2 bar.

C.5. 20 nm LSC|MgO

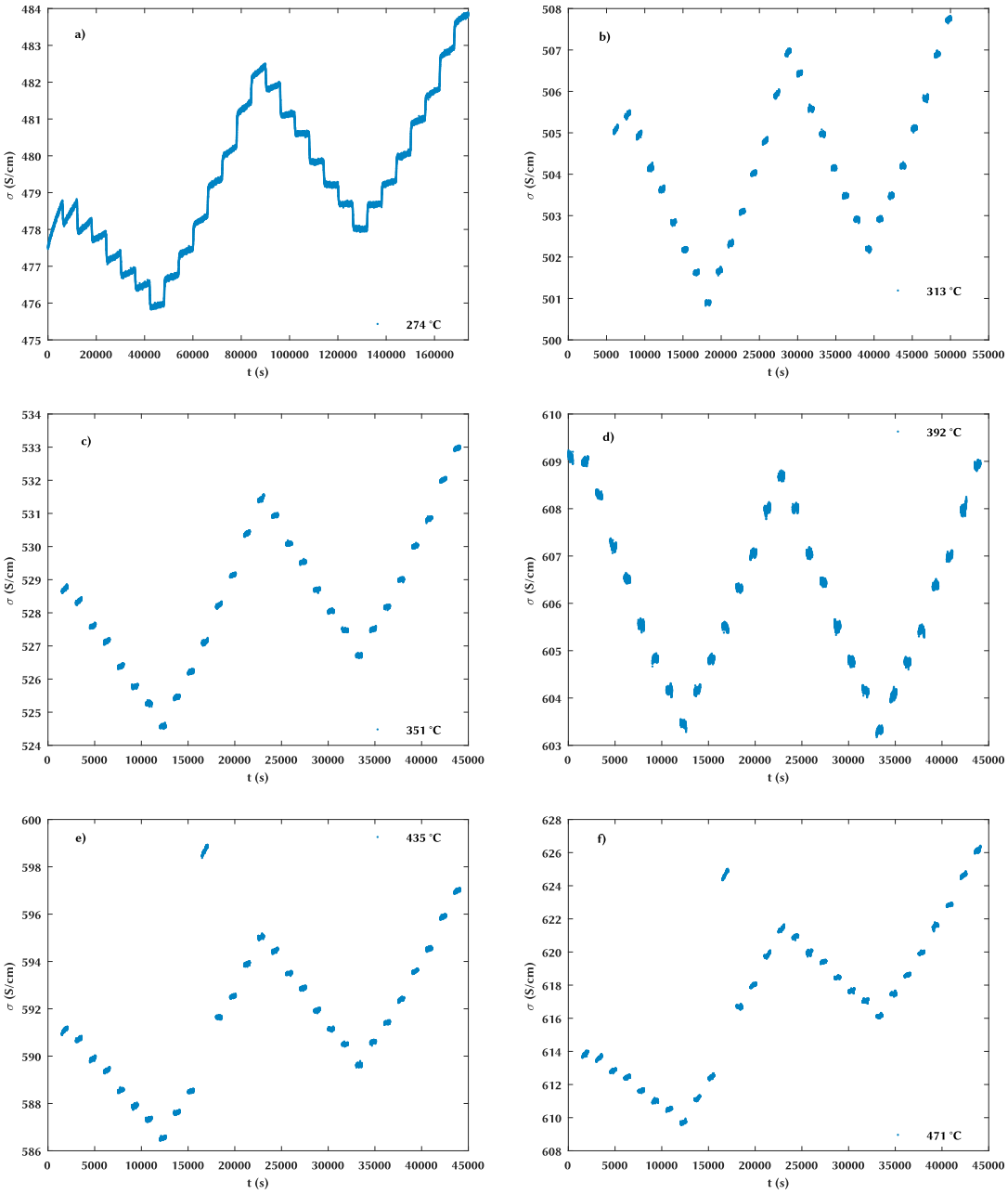

Figure C.5.: 20 nm LSC|MgO measured at: **a)** 274 °C, **b)** 313 °C, **c)** 351 °C, **d)** 392 °C, **e)** 435 °C and **f)** 471 °C. All experiments were started at a pO_2 of 0.2 bar. The outliers in **e)** and **f)** were caused by an input error. The values for the O_2 and N_2 gas streams were interchanged.

Bibliography

[1] John A. Kilner and Mónica Burriel. "Materials for Intermediate-Temperature Solid-Oxide Fuel Cells". In: *Annual Review of Materials Research* 44.1 (2014), pp. 365–393. DOI: 10.1146/annurev-matsci-070813-113426.

[2] J. Sunarso, S. Baumann, J. M. Serra, W. A. Meulenberg, S. Liu, Y. S. Lin, and J. C. Diniz da Costa. "Mixed ionic–electronic conducting (MIEC) ceramic-based membranes for oxygen separation". In: *Journal of Membrane Science* 320.1-2 (2008), pp. 13–41. DOI: 10.1016/j.memsci.2008.03.074.

[3] Ch. Tragut and K. H. Härdtl. "Kinetic behaviour of resistive oxygen sensors". In: *Sensors and Actuators B: Chemical* 4.3-4 (1991), pp. 425–429. DOI: 10.1016/0925-4005(91)80146-b.

[4] Wolfgang Menesklou, Hans-Jürgen Schreiner, Karl Heinz Härdtl, and Ellen Ivers-Tiffée. "High temperature oxygen sensors based on doped $SrTiO_3$". In: *Sensors and Actuators B: Chemical* 59.2-3 (1999), pp. 184–189. DOI: 10.1016/s0925-4005(99)00218-x.

[5] Jeffrey W. Fergus. "Perovskite oxides for semiconductor-based gas sensors". In: *Sensors and Actuators B: Chemical* 123.2 (2007), pp. 1169–1179. DOI: 10.1016/j.snb.2006.10.051.

[6] Andreas Egger, Edith Bucher, Min Yang, and Werner Sitte. "Comparison of oxygen exchange kinetics of the IT-SOFC cathode materials $La_{0.5}Sr_{0.5}CoO_{3-\delta}$ and $La_{0.6}Sr_{0.4}CoO_{3-\delta}$". In: *Solid State Ionics* 225 (2012), pp. 55–60. DOI: 10.1016/j.ssi.2012.02.050.

[7] L. M. van der Haar, M. W. den Otter, M. Morskate, H. J. M. Bouwmeester, and H. Verweij. "Chemical Diffusion and Oxygen Surface Transfer of $La_{1-x}Sr_xCoO_{3-\delta}$ Studied with Electrical Conductivity Relaxation". In: *Journal of The Electrochemical Society* 149.3 (2002), J41–J46. DOI: 10.1149/1.1446874.

[8] J. E. ten Elshof, M. H. R. Lankhorst, and H. J. M. Bouwmeester. "Oxygen Exchange and Diffusion Coefficients of Strontium-Doped Lanthanum Ferrites by Electrical Conductivity Relaxation". In: *Journal of The Electrochemical Society* 144.3 (1997), p. 1060. DOI: 10.1149/1.1837531.

[9] Edith Bucher, Andreas Egger, Peter Ried, Werner Sitte, and Peter Holtappels. "Oxygen nonstoichiometry and exchange kinetics of $Ba_{0.5}Sr_{0.5}Co_{0.8}Fe_{0.2}O_{3-\delta}$". In: *Solid State Ionics* 179.21-26 (2008), pp. 1032–1035. DOI: 10.1016/j.ssi.2008.01.089.

[10] Mónica Burriel, Christian Niedrig, Wolfgang Menesklou, Stefan F. Wagner, José Santiso, and Ellen Ivers-Tiffée. "BSCF epitaxial thin films: Electrical transport and oxygen surface exchange". In: *Solid State Ionics* 181.13-14 (2010), pp. 602–608. DOI: 10.1016/j.ssi.2010.03.005.

[11] H. J. M. Bouwmeester, M. W. Den Otter, and B. A. Boukamp. "Oxygen transport in $La_{0.6}Sr_{0.4}Co_{1-y}Fe_yO_{3-\delta}$". In: *Journal of Solid State Electrochemistry* 8.9 (2004), pp. 599–605. DOI: 10.1007/s10008-003-0488-3.

[12] M. Leonhardt, R. A. De Souza, J. Claus, and J. Maier. "Surface Kinetics of Oxygen Incorporation into $SrTiO_3$". In: *Journal of The Electrochemical Society* 149.2 (2002), J19–J26. DOI: 10.1149/1.1430723.

[13] J. Claus, M. Leonhardt, and J. Maier. "Tracer diffusion and chemical diffusion of oxygen in acceptor doped $SrTiO_3$". In: *Journal of Physics and Chemistry of Solids* 61.8 (2000), pp. 1199–1207. DOI: 10.1016/s0022-3697(99)00421-7.

[14] Markus Kubicek, Andreas Limbeck, Till Frömling, Herbert Hutter, and Jürgen Fleig. "Relationship between Cation Segregation and the Electrochemical Oxygen Reduction Kinetics of $La_{0.6}Sr_{0.4}CoO_{3-\delta}$ Thin Film Electrodes". In: *Journal of The Electrochemical Society* 158.6 (2011), B727. DOI: 10.1149/1.3581114.

[15] Zhuhua Cai, Yener Kuru, Jeong Woo Han, Yan Chen, and Bilge Yildiz. "Surface Electronic Structure Transitions at High Temperature on Perovskite Oxides: The Case of Strained $La_{0.8}Sr_{0.2}CoO_3$ Thin Films". In: *Journal of the American Chemical Society* 133.44 (2011), pp. 17696–17704. DOI: 10.1021/ja2059445.

[16] Edith Bucher, Werner Sitte, Frederik Klauser, and Erminald Bertel. "Impact of humid atmospheres on oxygen exchange properties, surface-near elemental composition, and surface morphology of $La_{0.6}Sr_{0.4}CoO_{3-\delta}$". In: *Solid State Ionics* 208 (2012), pp. 43–51. DOI: 10.1016/j.ssi.2011.12.005.

[17] Ghislain M. Rupp, Helena Téllez, John Druce, Andreas Limbeck, Tatsumi Ishihara, John Kilner, and Jürgen Fleig. "Surface chemistry of $La_{0.6}Sr_{0.4}CoO_{3-\delta}$ thin films and its impact on the oxygen surface exchange resistance". In: *Journal of Materials Chemistry A* 3.45 (2015), pp. 22759–22769. DOI: 10.1039/c5ta05279c.

[18] Edith Bucher, Christian Gspan, Ferdinand Hofer, and Werner Sitte. "Sulphur poisoning of the SOFC cathode material $La_{0.6}Sr_{0.4}CoO_{3-\delta}$". In: *Solid State Ionics* 238 (2013), pp. 15–23. DOI: 10.1016/j.ssi.2013.03.007.

[19] Edith Bucher, Christian Gspan, and Werner Sitte. "Degradation and regeneration of the SOFC cathode material $La_{0.6}Sr_{0.4}CoO_{3-\delta}$ in SO_2-containing atmospheres". In: *Solid State Ionics* 272 (2015), pp. 112–120. DOI: 10.1016/j.ssi.2015.01.009.

[20] E. Bucher, C. Gspan, T. Höschen, F. Hofer, and W. Sitte. "Oxygen exchange kinetics of $La_{0.6}Sr_{0.4}CoO_{3-\delta}$ affected by changes of the surface composition due to chromium and silicon poisoning". In: *Solid State Ionics* 299 (2017), pp. 26–31. DOI: 10.1016/j.ssi.2016.09.024.

[21] Lei Wang, Rotraut Merkle, Yuri A. Mastrikov, Eugene A. Kotomin, and Joachim Maier. "Oxygen exchange kinetics on solid oxide fuel cell cathode materials—general trends and their mechanistic interpretation". In: *Journal of Materials Research* 27.15 (2012), pp. 2000–2008. DOI: 10.1557/jmr.2012.186.

[22] Rotraut Merkle and Joachim Maier. "How Is Oxygen Incorporated into Oxides? A Comprehensive Kinetic Study of a Simple Solid-State Reaction with $SrTiO_3$ as a Model Material". In: *Angewandte Chemie International Edition* 47.21 (2008), pp. 3874–3894. DOI: 10.1002/anie.200700987.

[23] Bilge Yildiz. ""Stretching" the energy landscape of oxides—Effects on electrocatalysis and diffusion". In: *MRS Bulletin* 39.2 (2014), pp. 147–156. DOI: 10.1557/mrs.2014.8.

[24] Markus Kubicek, Zhuhua Cai, Wen Ma, Bilge Yildiz, Herbert Hutter, and Jürgen Fleig. "Tensile Lattice Strain Accelerates Oxygen Surface Exchange and Diffusion in $La_{1-x}Sr_xCoO_{3-\delta}$ Thin Films". In: *ACS Nano* 7.4 (2013), pp. 3276–3286. DOI: 10.1021/nn305987x.

[25] Christoph Riedl. "Modification of mixed conducting oxide surfaces with platinum nanoparticles and its effect on electrochemical properties". MA thesis. TU Wien, 2019.

[26] Christoph Riedl, Alexander Schmid, Andreas Nenning, Harald Summerer, Stefan Smetaczek, Sabine Schwarz, Johannes Bernardi, Alexander Optiz, Andreas Limbeck, and Juergen Fleig. "Outstanding Oxygen Reduction Kinetics of $La_{0.6}Sr_{0.4}FeO_{3-\delta}$ Surfaces Decorated with Platinum Nanoparticles". In: *Journal of The Electrochemical Society* 167.10 (2020), p. 104514. DOI: 10.1149/1945-7111/ab9c7f.

[27] Kian Kerman, Changhyun Ko, and Shriram Ramanathan. "Orientation dependent oxygen exchange kinetics on single crystal $SrTiO_3$ surfaces". In: *Physical Chemistry Chemical Physics* 14.34 (2012), p. 11953. DOI: 10.1039/c2cp41918a.

[28] Rotraut Merkle and Joachim Maier. "Oxygen incorporation into Fe-doped $SrTiO_3$: Mechanistic interpretation of the surface reaction". In: *Physical Chemistry Chemical Physics* 4.17 (2002), pp. 4140–4148. DOI: 10.1039/b204032h.

[29] Judith Januschewsky, Martin Ahrens, Alexander Opitz, Frank Kubel, and Jürgen Fleig. "Optimized $La_{0.6}Sr_{0.4}CoO_{3-\delta}$ Thin-Film Electrodes with Extremely Fast Oxygen-Reduction Kinetics". In: *Advanced Functional Materials* 19.19 (2009), pp. 3151–3156. DOI: 10.1002/adfm.200900362.

[30] Joachim Maier. "On the correlation of macroscopic and microscopic rate constants in solid state chemistry". In: *Solid State Ionics* 112.3-4 (1998), pp. 197–228. DOI: 10.1016/s0167-2738(98)00152-0.

[31] R. H. E. van Doorn, I. C. Fullarton, R. A. de Souza, J. A. Kilner, H. J. M. Bouwmeester, and A. J. Burggraaf. "Surface oxygen exchange of $La_{0.3}Sr_{0.7}CoO_{3-\delta}$". In: *Solid State Ionics* 96.1-2 (1997), pp. 1–7. DOI: 10.1016/s0167-2738(97)00011-8.

[32] Markus Kubicek, Tobias M. Huber, Andreas Welzl, Alexander Penn, Ghislain M. Rupp, Johannes Bernardi, Michael Stöger-Pollach, Herbert Hutter, and Jürgen Fleig. "Electrochemical properties of $La_{0.6}Sr_{0.4}CoO_{3-\delta}$ thin films investigated by complementary impedance spectroscopy and isotope exchange depth profiling". In: *Solid State Ionics* 256 (2014), pp. 38–44. DOI: 10.1016/j.ssi.2013.12.016.

[33] B. Ma, J. H. Park, and U. Balachandran. "Analysis of Oxygen Transport and Stoichiometry in Mixed-Conducting $SrFeCo_{0.5}O_x$ by Conductivity and Thermogravimetric Analysis". In: *Journal of The Electrochemical Society* 144.8 (1997), p. 2816. DOI: 10.1149/1.1837900.

[34] Chirranjeevi Balaji Gopal and Sossina M. Haile. "An electrical conductivity relaxation study of oxygen transport in samarium doped ceria". In: *J. Mater. Chem. A* 2.7 (2014), pp. 2405–2417. DOI: 10.1039/c3ta13404k.

[35] Isamu Yasuda and Tomij Hikita. "Precise Determination of the Chemical Diffusion Coefficient of Calcium-Doped Lanthanum Chromites by Means of Electrical Conductivity Relaxation". In: *Journal of The Electrochemical Society* 141.5 (1994), p. 1268. DOI: 10.1149/1.2054908.

[36] J. A. Lane and J. A. Kilner. "Measuring oxygen diffusion and oxygen surface exchange by conductivity relaxation". In: *Solid State Ionics* 136-137.1-2 (2000), pp. 997–1001. DOI: 10.1016/s0167-2738(00)00554-3.

[37] Stuart B. Adler. "Factors Governing Oxygen Reduction in Solid Oxide Fuel Cell Cathodes†". In: *Chemical Reviews* 104.10 (2004), pp. 4791–4844. DOI: 10.1021/cr020724o.

[38] Richard J. D. Tilley Tilley. *Defects in Solids*. John Wiley & Sons, Oct. 3, 2008. 548 pp. ISBN: 0470077948.

[39] Roger A. De Souza, Jürgen Fleig, Rotraut Merkle, and Joachim Maier. "$SrTiO_3$: A Model Electroceramic". In: *Zeitschrift für Metallkunde* 94.3 (2003), pp. 218–225. DOI: 10.3139/146.030218.

[40] Avner Rothschild, Wolfgang Menesklou, Harry L. Tuller, and Ellen Ivers-Tiffée. "Electronic Structure, Defect Chemistry, and Transport Properties of $SrTi_{1-x}Fe_xO_{3-y}$ Solid Solutions". In: *Chemistry of Materials* 18.16 (2006), pp. 3651–3659. DOI: 10.1021/cm052803x.

[41] Veronika Metlenko, WooChul Jung, Sean R. Bishop, Harry L. Tuller, and Roger A. De Souza. "Oxygen diffusion and surface exchange in the mixed conducting oxides $SrTi_{1-y}Fe_yO_{3-\delta}$". In: *Physical Chemistry Chemical Physics* 18.42 (2016), pp. 29495–29505. DOI: 10.1039/c6cp05756j.

[42] Ingrid Denk, Wolfram Münch, and Joachim Maier. "Partial Conductivities in $SrTiO_3$: Bulk Polarization Experiments, Oxygen Concentration Cell Measurements, and Defect-Chemical Modeling". In: *Journal of the American Ceramic Society* 78.12 (1995), pp. 3265–3272. DOI: 10.1111/j.1151-2916.1995.tb07963.x.

[43] N.-H. Chan, R. K. Sharma, and D. M. Smyth. "Nonstoichiometry in $SrTiO_3$". In: *Journal of The Electrochemical Society* 128.8 (1981), p. 1762. DOI: 10.1149/1.2127727.

[44] U. Balachandran and N. G. Eror. "Electrical conductivity in strontium titanate". In: *Journal of Solid State Chemistry* 39.3 (1981), pp. 351–359. DOI: 10.1016/0022-4596(81)90270-x.

[45] N. G. Eror and U. Balachandran. "High-Temperature Defect Structure of Acceptor-Doped Strontium Titanate". In: *Journal of the American Ceramic Society* 65.9 (1982), pp. 426–431. DOI: 10.1111/j.1151-2916.1982.tb10508.x.

[46] Ralf Moos and Karl Heinz Hardtl. "Defect Chemistry of Donor-Doped and Undoped Strontium Titanate Ceramics between 1000° and 1400°C". In: *Journal of the American Ceramic Society* 80.10 (2005), pp. 2549–2562. DOI: 10.1111/j.1151-2916.1997.tb03157.x.

[47] Rainer Waser. "Bulk Conductivity and Defect Chemistry of Acceptor-Doped Strontium Titanate in the Quenched State". In: *Journal of the American Ceramic Society* 74.8 (1991), pp. 1934–1940. DOI: 10.1111/j.1151-2916.1991.tb07812.x.

[48] R. A. De Souza. "Oxygen Diffusion in $SrTiO_3$ and Related Perovskite Oxides". In: *Advanced Functional Materials* 25.40 (2015), pp. 6326–6342. DOI: 10.1002/adfm.201500827.

[49] A. N. Petrov, O. F. Kononchuk, A. V. Andreev, V. A. Cherepanov, and P. Kofstad. "Crystal structure, electrical and magnetic properties of $La_{1-x}Sr_xCoO_{3-y}$". In: *Solid State Ionics* 80.3-4 (1995), pp. 189–199. DOI: 10.1016/0167-2738(95)00114-l.

[50] Atsushi Mineshige, Minoru Inaba, Takeshi Yao, Zempachi Ogumi, Kenji Kikuchi, and Masaya Kawase. "Crystal Structure and Metal–Insulator Transition of $La_{1-x}Sr_xCoO_3$". In: *Journal of Solid State Chemistry* 121.2 (1996), pp. 423–429. DOI: 10.1006/jssc.1996.0058.

[51] Junichiro Mizusaki, Junji Tabuchi, Takashi Matsuura, Shigeru Yamauchi, and Kazuo Fueki. "Electrical Conductivity and Seebeck Coefficient of Nonstoichiometric $La_{1-x}Sr_xCoO_{3-\delta}$". In: *Journal of The Electrochemical Society* 136 (7 1989), pp. 2082–2088. DOI: 10.1149/1.2097187.

[52] Martin Søgaard, Peter Vang Hendriksen, Mogens Mogensen, Finn Willy Poulsen, and Eivind Skou. "Oxygen nonstoichiometry and transport properties of strontium substituted lanthanum cobaltite". In: *Solid State Ionics* 177.37-38 (2006), pp. 3285–3296. DOI: 10.1016/j.ssi.2006.09.005.

[53] Junichiro Mizusaki, Yasuo Mima, Shigeru Yamauchi, Kazuo Fueki, and Hiroaki Tagawa. "Nonstoichiometry of the perovskite-type oxides $La_{1-x}Sr_xCoO_{3-\delta}$". In: *Journal of Solid State Chemistry* 80 (1 1989), pp. 102–111. DOI: 10.1016/0022-4596(89)90036-4.

[54] A. N. Petrov, V. A. Cherepanov, and A. Yu. Zuev. "Thermodynamics, defect structure, and charge transfer in doped lanthanum cobaltites: an overview". In: *Journal of Solid State Electrochemistry* 10.8 (2006), pp. 517–537. DOI: 10.1007/s10008-006-0124-0.

[55] Martijn H. R. Lankhorst, H. J. M. Bouwmeester, and H. Verweij. "High-Temperature Coulometric Titration of $La_{1-x}Sr_xCoO_{3-\delta}$: Evidence for the Effect of Electronic Band Structure on Nonstoichiometry Behavior". In: *Journal of Solid State Chemistry* 133.2 (1997), pp. 555–567. DOI: 10.1006/jssc.1997.7531.

[56] Martijn H. R. Lankhorst, H. J. M. Bouwmeester, and H. Verweij. "Use of the Rigid Band Formalism to Interpret the Relationship between O Chemical Potential and Electron Concentration in $La_{1-x}Sr_xCoO_{3-\delta}$". In: *Physical Review Letters* 77.14 (1996), pp. 2989–2992. DOI: 10.1103/physrevlett.77.2989.

[57] Martijn H. R. Lankhorst, H. J. M. Bouwmeester, and H. Verweij. "Importance of electronic band structure to nonstoichiometric behaviour of $La_{0.8}Sr_{0.2}CoO_{3-\delta}$". In: *Solid State Ionics* 96.1-2 (1997), pp. 21–27. DOI: 10.1016/s0167-2738(96)00620-0.

[58] M. H. R. Lankhorst and H. J. M. Bouwmeester. "Determination of Oxygen Nonstoichiometry and Diffusivity in Mixed Conducting Oxides by Oxygen Coulometric Titration". In: *Journal of The Electrochemical Society* 144.4 (1997), p. 1268. DOI: 10.1149/1.1837581.

[59] Wolfgang Preis, Michael Holzinger, and Werner Sitte. "Application of the van der Pauw Method to Conductivity Relaxation Experiments on $YBa_2Cu_3O_{6+\delta}$". In: *Monatshefte fuer Chemie/Chemical Monthly* 132.4 (2001), pp. 499–508. DOI: 10.1007/s007060170112.

[60] Chang-Rock Song and Han-Ill Yoo. "Chemical diffusivity of $BaTiO_{3-\delta}$ III. Conductivity–nonstoichiometry (δ) correlation in a mixed n/p regime". In: *Solid State Ionics* 124.3-4 (1999), pp. 289–299. DOI: 10.1016/s0167-2738(99)00226-x.

[61] Andreas Egger. "Rare earth nickelates as cathodes for solid oxide fuel cells". PhD thesis. Montanuniversität Leoben, 2013.

[62] S. Wang, A. Verma, Y. L. Yang, A. J. Jacobson, and B. Abeles. "The effect of the magnitude of the oxygen partial pressure change in electrical conductivity relaxation measurements: oxygen transport kinetics in $La_{0.5}Sr_{0.5}CoO_{3-\delta}$". In: *Solid State Ionics* 140.1-2 (2001), pp. 125–133. DOI: 10.1016/s0167-2738(01)00709-3.

[63] M. W. den Otter, H. J. M. Bouwmeester, B. A. Boukamp, and H. Verweij. "Reactor Flush Time Correction in Relaxation Experiments". In: *Journal of The Electrochemical Society* 148.2 (2001), J1–J6. DOI: 10.1149/1.1337604.

[64] Wolfgang Preis. "Modelling of surface exchange reaction, oxygen diffusion, and conductivity relaxation of solid oxides: Application to the van der Pauw method on disk-shaped samples". In: *Computational Materials Science* 103 (2015), pp. 237–243. DOI: 10.1016/j.commatsci.2014.11.017.

[65] John Crank. *The Mathematics of Diffusion*. Oxford University Press, Mar. 6, 1979. 424 pp. ISBN: 0198534116.

[66] M. W. den Otter, L. M. van der Haar, and H. J. M. Bouwmeester. "Numerical evaluation of eigenvalues of the sheet diffusion problem in the surface/diffusion mixed regime". In: *Solid State Ionics* 134.3-4 (2000), pp. 259–264. DOI: 10.1016/s0167-2738(00)00684-6.

[67] D. Poetzsch, R. Merkle, and J. Maier. "Stoichiometry Variation in Materials with Three Mobile Carriers-Thermodynamics and Transport Kinetics Exemplified for Protons, Oxygen Vacancies, and Holes". In: *Advanced Functional Materials* 25.10 (2015), pp. 1542–1557. DOI: 10.1002/adfm.201402212.

[68] Joachim Maier. "Mass Transport in the Presence of Internal Defect Reactions-Concept of Conservative Ensembles: I, Chemical Diffusion in Pure Compounds". In: *Journal of the American Ceramic Society* 76.5 (1993), pp. 1212–1217. DOI: 10.1111/j.1151-2916.1993.tb03743.x.

[69] Joachim Maier. "Mass Transport in the Presence of Internal Defect Reactions-Concept of Conservative Ensembles: III, Trapping Effect of Dopants on Chemical Diffusion". In: *Journal of the American Ceramic Society* 76.5 (1993), pp. 1223–1227. DOI: 10.1111/j.1151-2916.1993.tb03745.x.

[70] Joachim Maier. *Physical Chemistry of Ionic Materials*. John Wiley & Sons, Ltd, 2004. DOI: 10.1002/0470020229.

[71] Joachim Maier. "Interaction of oxygen with oxides: How to interpret measured effective rate constants?" In: *Solid State Ionics* 135.1-4 (2000), pp. 575–588. DOI: 10.1016/s0167-2738(00)00438-0.

[72] L. J. van der Pauw. "A method of measuring specific resistivity and Hall effect of discs of arbitrary shape". In: *Philips Research Reports* 13.1 (1958), p. 1.

[73] L. J. van der Pauw. "A method of measuring specific resistivity and Hall coefficient on lamellae of arbitrary shape". In: *Philips Technical Review* 20 (1958), pp. 220–224.

[74] Maggio P. Pechini. "Method of preparing lead and alkaline earth titanates and niobates and coating method using the same to form a capacitator". US 3330697 A. July 11, 1967.

[75] Andreas Falkenstein, David N. Mueller, Roger A. De Souza, and Manfred Martin. "Chemical relaxation experiments on mixed conducting oxides with large stoichiometry deviations". In: *Solid State Ionics* 280 (2015), pp. 66–73. DOI: 10.1016/j.ssi.2015.07.023.

[76] Geir Watterud. "Determination of oxygen transport coefficients in perovskites and perovskite related materials with mixed conductivity". PhD thesis. Norwegian University of Science and Technology, 2005.

[77] Bernard A. Boukamp, Matthijs W. den Otter, and Henny J. M. Bouwmeester. "Transport processes in mixed conducting oxides: combining time domain experiments and frequency domain analysis". In: *Journal of Solid State Electrochemistry* 8.9 (2004), pp. 592–598. DOI: 10.1007/s10008-003-0493-6.

[78] Yihong Li, Kirk Gerdes, Harvey Diamond, and Xingbo Liu. "An improved method to increase the predictive accuracy of the ECR technique". In: *Solid State Ionics* 204-205 (2011), pp. 104–110. DOI: 10.1016/j.ssi.2011.09.017.

[79] Alineason Materials Technology GmbH. URL: https://www.alineason.com/en/produkt/strontium-titanate/ (visited on 03/14/2020).

[80] X. Chen, S. Wang, Y. L. Yang, L. Smith, N. J. Wu, B. I. Kim, S. S. Perry, A. J. Jacobson, and A. Ignatiev. "Electrical conductivity relaxation studies of an epitaxial $La_{0.5}Sr_{0.5}CoO_{3-\delta}$ thin film". In: *Solid State Ionics* 146.3-4 (2002), pp. 405–413. DOI: 10.1016/s0167-2738(01)01031-1.

[81] Wolfgang Preis. "Modeling of conductivity relaxation in oxide ceramics taking account of concentration dependent chemical diffusivities and surface exchange coefficients". In: *Solid State Ionics* 316 (2018), pp. 118–124. DOI: 10.1016/j.ssi.2017.12.032.

[82] Ørjan Fossmark Lohne, Martin Søgaard, and Kjell Wiik. "The Significance of Gas-Phase Mass Transport in Assessment of k_{chem} and D_{chem}". In: *Journal of The Electrochemical Society* 160.11 (2013), F1282–F1292. DOI: 10.1149/2.077311jes.

[83] Gerardo Jose la O', Sung-Jin Ahn, Ethan Crumlin, Yuki Orikasa, Michael D. Biegalski, Hans M. Christen, and Yang Shao-Horn. "Catalytic Activity Enhancement for Oxygen Reduction on Epitaxial Perovskite Thin Films for Solid-Oxide Fuel Cells". In: *Angewandte Chemie International Edition* 49.31 (2010), pp. 5344–5347. DOI: 10.1002/anie.201001922.

[84] Ethan J. Crumlin, Sung-Jin Ahn, Dongkyu Lee, Eva Mutoro, Michael D. Biegalski, Hans M. Christen, and Yang Shao-Horn. "Oxygen Electrocatalysis on Epitaxial $La_{0.6}Sr_{0.4}CoO_{3-\delta}$ Perovskite Thin Films for Solid Oxide Fuel Cells". In: *Journal of The Electrochemical Society* 159.7 (2012), F219–F225. DOI: 10.1149/2.018207jes.

[85] E. Bucher, W. Jantscher, A. Benisek, W. Sitte, W. Preis, I. Rom, and F. Hofer. "Transport properties of $La_{0.4}Sr_{0.6}CoO_{3-\delta}$". In: *Solid State Ionics* 141-142 (2001), pp. 375–380. DOI: 10.1016/s0167-2738(01)00809-8.

[86] Noriko Sata, Kazuya Ikeda, Fumitada Iguchi, and Hiroo Yugami. "Synthesis of $La_{0.6}Sr_{0.4}FeO_3/La_{0.6}Sr_{0.4}CoO_3$ mixed ion conducting superlattices by PLD". In: *Solid State Ionics* 178.29-30 (2007), pp. 1563–1567. DOI: 10.1016/j.ssi.2007.10.005.

[87] Jong Hoon Joo, Rotraut Merkle, Jung-Hwa Kim, and Joachim Maier. "Measuring Electrical Properties of Thin Film Fuel Cell Electrodes by In Situ Infrared Spectroscopy". In: *Advanced Materials* 24.48 (2012), pp. 6507–6512. DOI: 10.1002/adma.201202934.

Acknowledgments

Abschließend möchte ich mich bei all jenen bedanken, die mich während der Erstellung dieser Arbeit begleitet und unterstützt haben.

Mein größter Dank gilt hierbei meinem Betreuer Markus Kubicek - danke für deine Zeit, deine endlose Geduld, deinen Enthusiasmus und danke, dass du dein Wissen mit mir geteilt hast! Eine bessere Betreuung hätte ich mir nicht vorstellen können.

An dieser Stelle möchte ich mich außerdem herzlich bei Jürgen Fleig für die Möglichkeit, meine Masterarbeit in seiner Arbeitsgruppe anfertigen zu dürfen, bedanken.

Vielen Dank auch an die gesamte Arbeitsgruppe für die tolle und hilfsbereite (Arbeits-)Atmosphäre. Es hat mir viel Freude bereitet, jeden Tag auf die Uni zu kommen. Besonderer Dank gilt dabei Harald Summerer, der mir nicht nur diverse LaTeX-Vorlagen zur Verfügung gestellt hat, sondern auch immer ein offenes Ohr hatte. Vielen Dank auch an Matthäus Siebenhofer für die Herstellung der Targets, sowie für die XRD-Messungen. Großer Dank gilt zudem Alexander Schmid, der mir geholfen hat, reciprocal space maps für diese Arbeit zu plotten. Danke auch an Eva Pycha, Max Morgenbesser und Stefan Smetaczek für die gemeinsame lustige Zeit im Büro. Hier sei auch unser Zimmernachbar Alexander Viernstein erwähnt - danke für deine Hilfsbereitschaft!

Ein riesiges Dankeschön möchte ich zudem meinen Freunden aussprechen - danke für eure großartige Unterstützung in den letzten Wochen und Monaten, für den Austausch, für's Zuhören und Aufmuntern in schwierigen Phasen. Ohne euch hätte ich es wohl nicht geschafft. Zu guter Letzt möchte ich mich noch ganz herzlich bei meinen Eltern bedanken, die mich über die Jahre finanziell unterstützt haben und die mir mein Studium damit erst ermöglicht haben. Danke!